FLOW AND FRACTURE OF TYPE 304 AUSTENITIC STAINLESS STEEL BAR AND WELDMENTS

Dissertation

Presented in Partial Fulfillment of the Requirements
for the Degree Doctor of Philosophy in the Graduate School
of The Ohio State University

By

Edward N. C. Dalder, B.Met.E., M.S. (Met. E.)

The Ohio State University
1973

Approved by:

J. W. Spretnak
Adviser
Department of Metallurgical Engineering

Reading Committee:

Prof. G. W. Powell
Prof. F. H. Beck
Prof. J. W. Spretnak

ACKNOWLEDGEMENTS

The author wishes to express his appreciation to Dr. J. W. Spretnak for his interest and guidance during the course of this investigation, and to the United States Atomic Energy Commission and to E. I. du Pont de Nemours, Inc. for financial support. The assistance of R. Justus, D. Hauser, and R. V. Farrar with various portions of the experimental work is gratefully acknowledged.

DEDICATION

To Jeanne

VITA

May 24, 1935	Born, Brooklyn, New York.
1956	B. Met. E., Polytechnic Institute of Brooklyn, Brooklyn, New York.
1956-1959	Metallurgical Engineer, Grumman Aerospace Corporation, Bethpage, New York.
1959-1962	Metallurgical Engineer, Republic Aviation Corporation, Farmingdale, New York.
1962-1964	Metallurgical Engineer, Pratt and Whitney Aircraft, East Hartford, Connecticut.
1964	M. S. (Met. E.), Polytechnic Institute of Brooklyn, Brooklyn, New York.
1964-1967	Senior Engineer, United States Steel Corporation, Monroeville, Pennsylvania.
1967-1973	Research Associate, Department of Metallurgical Engineering, The Ohio State University, Columbus, Ohio.

TABLE OF CONTENTS

LIST OF TABLES

LIST OF FIGURES

LIST OF FIGURES (Cont.)

LIST OF FIGURES (Cont.)

LIST OF FIGURES (Cont.)

LIST OF FIGURES (Cont.)

LIST OF FIGURES (Cont.)

LIST OF FIGURES (Cont.)

LIST OF FIGURES (Cont.)

INTRODUCTION

The load-bearing capacity of a component in a structure is determined by the material's ability to accomodate flaws or stress-concentrators, which may be present intentionally as a result of design-necessity or unintentionally as a result of a particular fabrication technique, such as welding. In turn, the material's ability to accomodate flaws is determined by the ability of the material to tolerate the accumulation of plastic-strain at a flaw, sometimes referred as the notch-ductility. Such flaws or discontinuities must be anticipated in real engineering structures.

For fracture in metallic materials to happen, uniform plastic flow must first take place, and then become confined or localized to one or more regions of the component. Fracture eventually occurs at or within one of these regions of localization of plastic flow. Several researchers (1-3) have stated that there are two means by which fracture may be initiated in metallic materials. The first method, termed "ductile fracture", involves the creation of discontinuities at interfaces between dispersed second-phase particles and the matrix, and the growth of these discontinuities to form the fracture. The second method, termed "brittle fracture" by some (4,5) and "instability-controlled fracture" by others (1-3), involves the localization of plastic flow on planes of maximum shear strain as predicted by the theory of plasticity (6), and the eventual separation of the material along these planes.

Previous research (7) has demonstrated that the critical shear strain at the onset of instability development (γ_i) is governed by prior strain (γ), strain rate ($\dot{\gamma}$), temperature (T), stress-gradient ($\frac{d\sigma}{dx}$), and a general factor encompassing microstructural effects (α) which includes strength-level. Values of γ_i are a measure of the material's ability to accomodate plastic strain in the presence of a notch, often referred to as the notch-ductility. These values do not usually correlate with values of ductility-parameters measured in the smooth-bar tensile test. For any material, a functional relationship summarizing the previous statement may be written in the form:

$$\gamma_i = f(\gamma, \dot{\gamma}, T, \frac{d\sigma}{dx}, \alpha) \qquad (1)$$

The object of these efforts is the determination of the effects of environmental (γ, $\dot{\gamma}$, T), metallurgical (α), and mechanical ($\frac{d\sigma}{dx}$) factors on the strain at which the structural member ceases to be a reliable load-bearing component, and instead teeters on the brink of mechanical failure.

To make such research truly meaningful, it should be carried out on real engineering materials of current and future interest to a wide segment of industry. A relevant application of engineering materials is the Liquid Metal Fast Breeder Reactor (LMFBR), said to be a solution to our country's developing energy crisis. Within this reactor, which has stated design requirements of 30 years life at temperatures to 1200°F in the presence of liquid sodium as a heat-transfer fluid, many metal components are being fabricated from Type 304 austenitic stainless steel (8,9). Typical components, their product forms, and specific design

requirements are summarized in Table 1. Bauer and Connor (8), in their extensive study of materials requirements for the LMFBR, have pointed out that data to be used in the development of analytical method for elevated-temperature long-time structural design in the elastic-plastic region may be obtained from tests run in air or a suitable inert environment to retard contamination of the specimen, rather than in liquid sodium: Two areas of critical importance to LMFBR designers were identified: (1) Data involving the determination of the values of strain-parameters at the onset of critical events are needed for elevated-temperature design-analyses based on strain, rather than stress limitations; and (2) data on the relative values of strain to the onset of critical events for unwelded material and weldments made by processes that will be employed in the fabrication of LMFBR components. Need for the latter information lies in the fact that, even if the weldments are as strong or stronger than the unwelded base-metal, creep of the latter may place additional loads on the weldment. If the weldment has lower values of strain to the onset of some critical event (such as initiation of tertiary creep or a fast running crack) as existing data suggests, failure may well be initiated in the "stronger" component of the structure.

It was decided to evaluate one-inch diameter bar as being typical of a readily available wrought product form, and a two-inch thick weldment fabricated from rolled plate and Type 308 stainless steel filler metal by the manual shielded metal arc process as being typical of a welding process used in the fabrication of LMFBR components (9). The former material was evaluated in both the solution-annealed and sensitized conditions, while the latter material was evaluated as welded, i.e.;

with a sensitized heat-affected zone, which reflects the condition of large welded LMFBR components after field-erection welding. The temperature: strain-rate envelope was selected to include typical LMFBR operating requirements: room-temperature to 1200°F (649°C) and strain-rates of 0.06 to 5 per minute (10,11).

REVIEW OF PREVIOUS WORK

1. The Two Modes of Fracture

The two basic modes of fracture, as described in the introduction, are by pore formation and coalescence and by instability formation and growth in directions of pure shear. While cavitation, or pore formation and coalesence, has been accepted as one of the two basic modes of fracture for quite some time, several researchers (12-14) have stated that it is one of the least understood failure-modes. The difficulty with the concept of cavitation lies in the difficulties in formulating mathematical criteria of the strain to fracture that yield predictions which fall at all close to experimentally-observed values (15). Conceptually, cavitation is often envisioned as a nucleation and growth process. After considerable plastic flow, pores nucleate at some matrix discontinuity, such as inclusions, precipitates, dispersions, and grain or subgrain boundaries. The pores then grow with continuing plastic deformation and expand under triaxial stresses until they are completely joined on the fracture surface. Thus, the material between the pores fails by 100% reduction of area in pure ductile fracture. Some complications occur with different states of stress, for instance in a round tensile specimen in which a stress state favoring a shear coalescence of the pores is generated in the necked section. Also, loads requiring pulling apart from one edge create a "tearing" fracture. These different

states of stress only slightly affect the coalescence stage of cavitation; the basic mode of fracture, pore formation at discontinuities and coalescence by rupture between pores, is consistent.

A second mode of fracture, as described in the introduction, is fracture by instability in directions of pure shear. The original suggestion of this type of fracture appears to have been made by a Dutch plastician, F. K. Th. Van Iterson (16). After observations of flow in many metallic and non-metallic materials, Van Iterson postulated that material achieves a new state of matter, somewhere between solid and liquid, which he called the "plasticized state." The plasticized state will occur in directions of zero extensional strain. Instability fracture is a fracture resulting from localized plastic flow, the plastic flow being shear deformation in directions of pure shear. Instability deformation is not a geometric instability as necking in the round tensile specimen, nor is it crystallographic slip. Spretnak (17), in a recent summary paper, stated the three requirements for the formation of such localized plastic flow: (a) a stress gradient, (b) a free surface, and (c) the material must simulate the ideally plastic state.

Even though the type of deformation and direction of that deformation for instability fractures has been defined, there are three distinct types of fracture that can occur through instability flow. Suppose the plane of deformation has a finite width. Then the first type of instability fracture occurs in the case of highly localized plastic flow on a plane of pure shear, with the thickness of the instability plane being smaller than the second phase particles distributed throughout the matrix. As a result of the intense localization of flow, the

material behaves homogeneously with respect to the fracture process, with little evidence of the second phase particles on the fracture surface. This results in the topography of the fracture surface failing to show large dimples which would otherwise be formed in a material with second phase particles which underwent uniform deformation.

A second type of instability-fracture may occur when the plane on which instabilities lie is thicker than the size of the dispersed second phase particles. The diffuse instability flow would lead to pore formation and coalescence within the instability, as suggested by Spretnak (18). The differences between the two types of instability fractures lie in the widths of the plane of localized flow relative to the size of the dispersed second phase particles and the effect of the width on the process of final fracture.

The third type of fracture which may involve instability flow is not instability controlled, and is called a mixed mode fracture. In the case in which uniform deformation has led to pore formation, the coalescence could occur if the formation of pores fulfilled the requirements for instability-controlled flow (free surface, stress gradient, ideal plastic material). In this type of fracture the instability fracture causes coalescence, limiting the ductility normally found in cavitation by limiting the amount of plastic flow required to join the pores.

2. Cavitation

The first observation of the formation of a large internal cavity in a cylindrical tensile specimen has been attributed to Ludwik (19). Many recent workers have reported the results of observations made on

cylindrical tensile specimens, and presented convincing arguments for the occurrence of ductile fracture by cavitation, for example Broek (15) Puttick (20), and Rogers (21). Beachem (22) has given an analysis and proof of the cavitation process being the controlling feature in ductile fracture. By observing actual fracture-surfaces by electron-microscopy, Beachem was able to correlate the effects of stress-state on the various modes of cavity-coalescence. Figure 1 presents the types of surface topography and the mode of void coalescence that caused the topography.

A. Void formation at spherical particles

1. Theories--A spherically-shaped second-phase particle whose elastic and plastic constants differ from those of the matrix will act as a stress-concentrator. When the stiffness of the particle is more than that of the matrix, stress-concentrations will occur at its poles. When the stiffness of the particle is less than that of the matrix, concentrations of stress will occur at the particle's equator. Goodier (23) has presented calculations of the stresses developed around spherical particles.

Gurland and Plateau (24) have proposed a simple model for cavity-formation in conjunction with spherical particles. They considered the case where the particle stiffness is greater than the matrix stiffness, which would result, if the sample were loaded in tension, in the stress-concentrations at the poles of the particles creating tensile stresses over the matrix: particle interface. Their basic assumptions were that (a) stresses in the matrix are affected by the particle over a volume whose dimensions are of the order of those of the particle, (b) the size of the initial void equals that of the inclusion, and (c) the criterion

for cavity formation is that the surface-energy required to create the new free-surfaces is supplied by the relief of strain-energy by void-formation. Their results are summarized in equation (2)

$$\sigma_{void} = \left(\frac{E\gamma}{a}\right)^{1/2} \frac{1}{\alpha} \qquad (2)$$

where σ is the nominal stress in the matrix, γ is the surface-energy, and α is a factor representing the concentration of stress around the particle. It has been indicated by Rosenfield (14) that the magnitude of γ in equation (2) depends on the interface-energy, γ_{mp}, the particle's surface-energy, γ_p, and the matrix surface-energy, γ_M, such that

$$\begin{aligned} \gamma &= 2\gamma_p \text{ for fracture of the particle} \\ \gamma &= \gamma_M + \gamma_p - \gamma_{Mp} \text{ for decohesion at the interface.} \end{aligned} \qquad (3)$$

Brook (15) has shown that the relationship between α and the elastic-constants of the matrix and particle are very complex.

A mechanism and criterion developed specifically for formation of cavities at the interface between a spherical inclusion in a shear-band and the matrix has been proposed by Ashby (25). In this model, which was developed to rationalize the work-hardening behavior of dispersion-strengthened materials, the particle is considered to be infinitely stiff, while the matrix is permitted to undergo plastic deformation. Because of its presence in a shear-band, the particle stresses the surrounding matrix, since the particle will provide a constraint to free deformation of the hole, as is shown in Figure 2. Under load, the stresses produced by the particle become large enough to exceed the yield stress, producing plastic flow. Ashby considers this plastic flow to be secondary slip, with

the role of relieving the stresses caused by the particles. This relief can be produced by forming interstitial loops in areas of the matrix under compression, and by forming vacancy loops in areas of the matrix under tension, as shown in Figure 2b. Finally, coalescence of vacancy-loops at the particle: matrix interface creates a cavity or void (Figure 2c). Assuming a linear variation of strain in the shear-band, and that void-formation occurred when the interfacial stress exceeded a critical value, σ_v, Ashby obtained

$$\sigma_v = \alpha\beta \frac{a\varepsilon}{bL} \qquad (4)$$

where ε is the strain in the matrix, a is the size of the particle, b is the Burgers vector, α and β are two constants, and L is the length of the dislocation-pileup. The matrix-strain, ε_v, of a void is

$$\varepsilon_v = \frac{1}{\alpha\beta} \frac{bL}{a} \sigma_v \qquad (5)$$

Equation (5) predicted that the strain for void-formation would vary inversly with the particle-size, a, while equation (2) of Gurland and Plateau predicted a variation with the inverse square-root of a. This difference could, however, be caused by a dependence of L on particle-size.

An objection to Ashby's model is that it requires slip occur by motion of prismatic loops. Prismatic loops are difficult to move, as high stresses are required to move them in their glide-path. Hence, the first vacancy loop formed should adhere to the interface and form the required cavity. While prismatic loops are occasionally seen in as-

quenched material, probably as a result of vacancy condensation, they are usually not observed in plastically-strained materials.

2. Experimental observations--of void-formation at spherical inclusions are numerous (26-29). Tipnis and Cook (26), in a study of flow and fracture in resulfurized free-machining steels, found evidence of void-formation at the inclusion: matrix interface of spherical MnS inclusions under a variety of loading conditions ranging from torsion to torsion plus superposed tension or compression. Brower and Flemings (27) on their study of chill-cast iron plus spherical FeO or SiO_2 inclusions deformed in tension, made direct observations of inclusion: matrix decohesion using the scanning electron microscope. Broek (28), who investigated the mechanisms of void-initiation and growth in six precipitation-strengthened aluminum-base alloys, found evidence of void-initiation at interfaces between spherical particles and the matrix after straining both 2024 and 7075 alloys in the fully-aged condition. Baker and Charles (29), who investigated the deformation behavior of MnS inclusions in resulfurized steels during hot-rolling, found direct metallographic evidence of voids at the poles of spherical inclusions. They postulated that the void-formation by decohesion at the inclusion: matrix interface at the locations of maximum stress as predicted by Goodier (23) was due to the inability of the austenitic matrix to flow around the non-deforming inclusion while simultaneously maintaining contact with it. Similar void-formation by inclusion: matrix decohesions in steels containing non-deforming oxide and/or silicate inclusions have also been reported by Pickering (30), and Rudnik (31), as well as Charles and Uchiyama (31).

B. Void-formation at elongated particles

1. Theories--Gurland and Plateau's (24) condition for void-formation has also been applied to elongated particles. For this case, equation (2) is modified to

$$\sigma_v = \frac{1}{q}\left(\frac{E\gamma}{\lambda}\right)^{1/2} \qquad (6)$$

where a is the diameter of the particle, λ is length, and q is now a new factor representing the concentration of stress around the particle. Hence, the stress for cavity-formation depends on the length of the particle, rather than on its aspect-ratio (ratio of length to width).

It is often assumed that particles fracture by cleavage due to stresses created by dislocations piling-up against the particles. Two variations of an analysis of particle-fracture by the shear-stress from a piled-up group of dislocations have been reported by Gurland (33) and Barnby (34). In its glide-plane near the head of the piled-up group of n dislocations, the shear stress exerted by the group is

$$\tau = n\,\tau_a$$

where τ_a is the applied shear stress. The approximate number of dislocations in the pile-up is given by

$$n = \frac{2L}{Gb}\,\tau_a$$

where L is the length of the pile-up, G is the shear modulus of the material, and b is the Burgers vector. Solving for the shear-stress on the particle, one obtains

$$\tau = \frac{2L}{Gb}(\tau_a)^2$$

Assuming that fracture of the inclusion takes place when this stress exceeds a critical value τ_{cr} the condition for cavity-formation becomes

$$\tau_a = \left(\frac{Gb \cdot \tau_{cr}}{2L}\right)^{1/2} \qquad (7)$$

Equation (7) indicates that the stress τ_a is not a function of particle-size. Barnby (31) claimed that τ_{cr} the particle's fracture-stress, must vary as the square root of the diameter of the particle; requiring that large particles would fail at higher stresses than small particles, which is not realistic. Gurland (33) incorporates the effect of particle-size in equation (7) by assuming the existence of a relationship between the size of the pile-up and the spacing and size of the particles.

Broek (15) in his study of ductile fracture in precipitation-strengthened aluminum alloys, raised the point that second-phases formed by solid-state precipitation-reactions are metallic in nature and should be capable of some plastic-deformation before fracture. He then proposed a criterion for fracture of limited-ductility metallic particles involving their undergoing plastic deformation in tension during straining of the matrix until the ductility of the metallic particle is exhausted and fracture results. Since these particles are almost always stiffer than the matrix, compatibility of deformation between the particle and matrix will develop higher stresses in the particle than in the matrix. This stress-concentrating effect results in the particles failing at relatively low overall strains. Broek assumed that the metallic particles would fracture when the maximum strain in the inclusion,

which would be developed at its mid-length according to his elastic-analysis, exceeds a critical value. Limited agreement with experiment was obtained.

2. Experimental observations--of void-formation at elongated particles are numerous (26, 29, 35, 36). Tipnis and Cook (26) found extensive evidence of void formation associated with both inclusion: matrix decohesions at the duplex-phase tails of ductile (Fe, Mn) S inclusions and by fracturing of non-deforming MnS inclusions in resulfurized free-machining steels deformed in torsion both without or with superposed axial tension or compression. Similar results were seen by Baker and Charles (29) in their studies of deformation of MnS inclusions in resulfurized steels by hot rolling.

Shapiro and Dieter (35) found evidence of void-initiation by both inclusion: matrix decohesions and by fracturing of inclusions, probably oxides and carbonitrides, during torsion-testing of a Fe-Cr-Ni alloy (Inconel 600) at 800°F to 1200°F. No attempt was made to correlate macroscopic loading-conditions (torsion versus torsion plus superposed tension or compression) with the two modes of void-formation.

Driver (36) in his study of elevated-temperature fatigue-failure in types 304L, 304H, and 321 austenitic stainless steels, found metallographic evidence of void-initiation by decohesions at the interface between elongated $M_{23}C_6$ grain-boundary carbides and the austenitic matrix.

In the case of dispersion-hardened materials, which are usually strengthened with oxide particles, one would think that the cohesive strength between the matrix and the oxide particles is low. As a consequence of the concentration of stresses at the particle-poles, relatively

low stresses are needed to exceed the matrix: oxide interfacial strength, resulting in cavities being found at the poles (37-39).

On the other hand, evidence for void-initiation by particle-fracture alone has been seen (28, 34, 40). Broek (28) in his investigation of void-initiation and growth in precipitation-strengthened aluminum alloy, found extensive evidence of void-initiation due to fracture of elongated inclusions of sub-microscopic (1000Å-3000Å) size. No evidence of fracture of θ' particles, also present in one of the alloys containing these inclusions, was seen. Barnby (34) and Barnby and Peace (40) in their studies of tensile and fatigue deformation of austenitic stainless steel sensitized to produce extensive precipitates of rod-like $M_{23}C_6$ carbides, found that void-initiation in the matrix occurred only at the extensions of transverse cracks originating within the elongated carbides. No evidence of void-initiation by decohesion at the carbide: matrix interfaces was seen.

C. Void-coalescence

Gurland and Plateau (24) have proposed a model for coalescence of voids. Their assumptions include considering the void as an idealized ellipsoid, considering the inclusion to be non-deformable relative to the matrix, considering that growth of the void is due to tensile rather than shear strains, and assuming the the effect of strain-concentration at the equator of the ellipsoidal inclusion can be incorporated in a strain-concentration factor k_c, where

$$k_c = \frac{d\varepsilon_m}{d\varepsilon} = 1 + C\,\frac{a^2}{p^2}\,. \qquad (8)$$

In equation (8), a and p are major and minor axis of the void, ε_m is the strain at the equator, ε is the nominal strain in the matrix, and C is a constant. Their final result for the strain in the matrix at failure, ε_f, is given by

$$\varepsilon_f = \varepsilon_v + \frac{1}{2} \ln \left(\frac{D}{C} f^{-1/3} + 1\right) \qquad (9)$$

where ε_v is the strain to create a void, and D is the mean distance between centers of the particles at the instant of fracture, and is related to the mean distance between particles in the undeformed alloy, D_o, by

$$D = D_o \exp\left[-(\varepsilon - \varepsilon_v)\right].$$

However, Gurland and Plateau's assumption for their strain-concentration factor, k_c, is open to question, casting a suspicion as the basic validity of their analysis.

Thomason (41) has proposed a different criterion for void-coalescence. For the two-dimensional case, he examines the conditions for necking of the matrix between regualrly-distributed voids of square cross section in an element of unit thickness (Figure 3). He assumed that necking occurs if a critical value is exceeded by σ_n, the net section stress. The nominal stress, σ, is related to the net-section stress by

$$\sigma_{dx} = \sigma_n \, (dx - nw)$$

or

$$\sigma = \sigma_n \left(1 - \frac{nw}{dx}\right). \qquad (10)$$

The volume-fraction of cavities may be calculated from Figure 3 as

$$f = nw \cdot \frac{nw}{dx} \cdot dy = \left(\frac{nw}{dx}\right)^2 .$$

Therefore, the condition for necking (coalescence) becomes

$$\sigma_f = C(1-f^{1/2})$$

where C is a constant, and σ_f is the fracture-stress. This equation is Thomason's basic result.

Recently, Thomason (42) extended the above analysis to the case where the model depicted in Figure 3 has the cavities filled with hard prismatic particles that are firmly bonded to the matrix. Thomason assumed that matrix: particle decohesion occurs when the interfacial tensile stress reaches a critical level, σ_o, which is independent of any shear stress acting along the interface. Thomason also assumed that at the onset of internal necking no change in stress occurs at the top and bottom surfaces of the particles, and that the matrix obeyed the Levy-Von Mises flow-rule and the Von Mises yield criterion. He stated that two possible situations existed at the moment of macroscopic tensile instability; (a) flow without decohesion at the inclusion: matrix interface, and (b) flow with decohesion along the upper and lower faces of the particles but not along the sides (Figure 4). The general condition for incipient internal necking between particles is that the load to cause internal necking, L_N, becomes just equal to, or less than, that required for uniform flow, L_u, i.e.

$$L_N \leq L_u \qquad (11)$$

After considerable mathematics, Thomason concluded that when decohesion

failed to occur at the particle: matrix interface, internal necking could also not occur and, if internal cavities are not created by other mechanisms, such as fracture of the particle, this idealized material can "fail" only by 100 percent reduction in area at an external neck. For the case of particle: matrix decohesion, Thomason concluded that the ductile matrix-material could be strained in the z direction until the cavities at the ends of the particles have been elongated enough to enable internal necking to take place. Then, ductile fracture will occur. He also concluded that prevention of complete particle: matrix decohesion, i.e., maintainence of particle: matrix contact along the sides (Figure 5) will delay the onset of ductile failure by internal necking between particles and so increase the macroscopic ductility of the material.

McClintock, Kaplan, and Berg (43) presented a detailed treatment of void-formation and coalescence. Considering a two-dimensional section through a linear-hardening material containing uniformly-spaced cylindrical holes that was subjected to a combination of shear and hydrostatic tension, they calculated how the holes would deform under the stated loading-conditions. They found that the holes elongated in the direction of principal stress, but that the deformation of shear bands rotated the holes into the direction of principal stress and tended to close them (Figure 6). Fracture occurred when the boundaries of the deforming elements in which the holes lie make contact with the holes (Figure 6). This implies that the majority of the elements will be so unfavorable located that when boundaries and holes come into contact, they touch and coalesce simultaneously. The main objection to this model is

that it works best for non-rigid inclusions i.e., voids. In the case of a real material in place of the void, say a relatively rigid oxide or carbide, free deformation of the void is seriously retarded. Another objection is that the model is two-dimensional.

Broek (44) has proposed a model for void-coalescence based, in part, on the following experimental observations be made on precipitation-hardened aluminum alloys:

(1) Voids associated with large inclusions, hence large enough to be seen through the optical microscope, are not essential to the fracture process.

(2) Fracture of elongated particles leads to creation of cavities in the matrix long before fracture of the sample occurs.

(3) Cavity initiation before fracture was seen to a very limited extent. Cavity initiation on a large scale probably led to spontaneous growth and coalescence.

(4) Growth of cavities by slip-plane decohesion, under the action of shear stresses, occurred mainly in a direction normal to the applied tensile stress.

Dislocation pile-ups form at particles during plastic-flow, as shown in Figure 7. Primary loops shown in Figure 7a form by a mechanism proposed by Hirsch (45) and Ashby (46). The particle repels the loops through the action of the loop's image forces. Opposing these image forces are stresses generated by the pile-up and the applied stress, whichare acting to push the leading loop towards the particle. When the image forces are less than the back stress on the leading loop, the leading loop will move towards the particle: matrix interface. Where several

loops are pushed into the interface it becomes possible for a decohesion to take place along AB in Figure 8, forming a void. Formation of the embryonic void causes the repulsive force on subsequent loops to be drastically reduced, enabling the majority of the dislocations in the pile-up to empty themselves into the newly-formed void. Dislocation sources behind the loops, which were shut off because of the constraint of the pile ups, can resume action. Hence, the process can, in principle, lead to unstable void growth and coalescence almost immediately upon formation of the voids (Figure 8). Actually, the situation of a single giant pile up probably would not occur. Friedel (47) argued that plastic relaxation of the stresses created by the pile-up began when the stress exerted on secondary sources by the piled-up group exceeded the elastic limit. He showed that pile-ups in face-centered cubic crystals should relax if they contain greater than about five dislocations, which implies that many pile-ups must be formed on different slip planes (Figure 8f). This situation would also lead to decohesion at particle: matrix interfaces when one or more dislocations are pushed into the interface. There, newly-formed voids can grow, due to dislocations on other slip-planes that are attracted to the voids (Figure 8g). This growth is depicted in Figure 9. Broek was unable to evaluate the model because of the complexity of the mathematical methods that are available for three-dimensional problems of this nature.

3. Instability Flow and Fracture

A. Observations of fracture by instabilities

Localized flow has been observed in many non-metallic materials,

such as high polymers (48) and molding sands (49). Little research effort has been aimed at investigating this phenomenon. Rogers has proposed an additional fracture mode, namely void sheets, that is in fact the diffuse-instability-controlled fracture (21). These void sheets are small regions of shear deformation, usually associated with shear lips in a round tensile specimen where voids have formed and coalesced. Several other investigators have reported the appearance of a diffuse localized flow at the shear lip in tensile specimens (50,51). Hayden and Floreen have presented some convincing evidence of diffuse instabilities leading to fracture (52). In their work with notched bars of 26Cr-6Ni stainless steel, evidence of localized flow is clear because of the duplex microstructure of the material. Localized flow followed the predicted path of pure shear. Figure 10 is a reproduction of a photomicrograph made by Hayden and Floreen. That the diffuse flow in Figure 10 is in the direction of pure shear can be made by a comparison with Figure 11 (3).

Several early studies which had as their purpose the investigation of localized flow failed to show any clear-cut relation between the apparent localized flow and the fracture process (53-57). Most of these studies indicated that fracture occurred at interfaces between regions of localized and uniform flow. The width of the regions of localized flow in relation to the microstructure was not determined.

Considerable evidence of coalescence of voids by instability fracture has recently become available in the literature. In studies on hot-working of resulfurized free-machining steels containing (Fe, Mn)S inclusions of various morphologies, Baker and Charles (29) found evidence

of void coalescence by a localized shear mechanism in the matrix directed towards nearby inclusion neighbors. The scale of localization appeared to be on the order of the size of the inclusions to slightly smaller. During room temperature torsional deformation of resulfurized free-machining steels similar to those just described, Tipnis and Cook (26) observed localization of plastic flow leading to cracking in regions of the matrix between elongated ductile tails of duplex-phase inclusions. Brower and Flemings (27), in their study of the ambient temperature tensile properties of chill-cast Fe-FeO and Fe-SiO_2 alloys, found ample evidence of failure by localization of plastic flow between voids formed by inclusion: matrix decohesions. The scale of localization appeared to be on the order of the diameter of the inclusions to slightly larger. In sensitized type 316 austenitic stainless steel, containing about 3 v/o rod-like $M_{23}C_6$ carbide precipitates, deformed in either tension or high-strain fatigue, Barnby (34) and Barnby and Peace (40) found evidence of propagation of voids by localization of plastic flow in the matrix between voids formed by the fracture of carbide rods. The scale of localization appeared to be on the order of the diameter of the rod-like particles, and much less than the length of the particles. Also, some coalescence of large voids, not necessarily formed by plastic flow but probably inherent voids, has been seen and reported. Rogers reported such a concentration of flow in steel (21). Troiano and Kochera found highly concentrated shear flow between large voids in a copper-tin alloy (58), substantiating the concept of a cavity creating the necessary conditions for instability-flow.

Localized plastic flow is very difficult to detect on a fine scale. Little evidence of finding a layer of localized plastic deformation which has a thickness smaller than second phase particles has been reported. Recently, McGarry (59), in a study of the effect of strength level and strain-rate on the mode of fracture-initiation in AISI 4340 steel, found that for higher strength levels the high strain-rates produced instability fractures wherein the localized plastic flow appeared to be on a scale smaller than the temper-carbides. The only other direct evidence of this extreme localization of plastic flow is seen in the work by Barnby (34) and Barnby and Peace (40) on sensitized Type 316 stainless steel referred to earlier, wherein propagation of the fracture was by localized plastic flow, "shear bands" to use the authors' terminology, on a scale of the rod-like carbide's diameter, which was much less than the particles' lengths. However, some indirect evidence of instability fracture in which the layer of localized flow is smaller than second phase particles has been published. Griffis and Spretnak (60) have proposed that the plastic stretch zone associated with pre-fatigued fracture specimens is an instability fracture. The fracture surface of the plastic stretch zone is featurless as expected for an instability fracture in which the width of the regionof localized plastic flow is extremely small. Also, Spretnak has proposed that quasi-cleavage fracture is an instability fracture. Some convincing information that supports this idea was found by Chang (61) who discovered the existence of plastically deformed metal just below the surface of a quasi-cleavage fracture.

This observation showed that the fracture is not a classical cleavage fracture, i.e., a fracture that occurred by the stresses reaching the

cohesive strength of the metallic bonds, but that there is highly localized plastic flow associated with the fracture process. The quasi-cleavage fracture surface has been found to have little or no second phase particles on it, which substantiates the requirement of an instability fracture resulting from highly localized plastic flow.

B. Factors affecting instability behavior

Many investigators have studied the effect of strength level and strain rate on instability formation. Most of these studies were conducted by torsion testing in which instabilities can form and propagate along the surface of a torsion bar. The instabilities are visible with the naked eye which makes studies much easier than those in which metallography is required to detect localized flow.

The earliest studies of instability behavior in torsion were reported by Rybalko (53), who examined the room-temperature torsional-deformation behavior of a quenched and tempered low alloy steel as a function of tempering temperature (strength level). He found that localization of plastic flow occurred long before final fracture and that the strain to the first localization of plastic flow increased with increasing tempering temperature (decreasing strength level). Rybalko suggested that the value of the strain to first localization of plastic flow be considered as a new material parameter characteristic of the incidence of the beginning of the failure process.

Rybalko and Yakutovich (54,55) have reported on the stationary and nonstationary zones of localized strain developed in quenched and tempered steel bars twisted in torsion. The physical cause of nonstationary zones was attributed to the microstructural heterogeneities, and that of

the stationary type to physical weakening or work softening. Localization of torsional strain was suggested as an important step in the torsion test. It was suggested that the steps involved in the process are (a) thermal hardening, (b) physical softening, and (c) thermal softening. They reported that the amount of stable or non-localized strain decreases monotonically with increasing strain rate. The mechanism of fracture in these bands of unstable flow was the coalescence of micro-cracks, 1-2 microns in length. These cracks were found to be oriented at 45° to the axis of the specimen and it was concluded that tensile stresses are responsible for their propagation. It was proposed that the strain rate at the localization of plastic flow may be an important material parameter.

Zelova, Demina, and Fridman (56) applied the knurled grid technique to the surface of cylindrical steel torsion specimens. Analysis of the grid distortion on specimens after twisting showed the gross nature of the localized flow. It was emphasized that meaningful strains must be calculated from the local plastic deformation in the zone of greatest plastic shear. It was also observed that low tempering temperatures promoted heterogeneous flow in steel torsion specimens. It was found that surface-quality of the specimens greatly affected the strain to fracture, in that mechanically-polished specimen showed much higher values of this parameter than did the ground specimens.

Polokowski and Mostovoy were the first in the United States to report on studies of instabilities in torsion (57). Their work with copper and a two-phase copper alloy, as well as cold drawn AISI 1045 and AISI 4340 steels resulted in their concluding that torsional instabilities

formed in single phase metals and alloys which have low strain hardening coefficients, and did not form in two-phase alloys.

Fields and Backofen (62), in their work on 2024 aluminum alloy, observed that a low strain hardening coefficient and low strain rate sensitivity are factors which promote localized deformation. Absence of significant localized flow was observed for the case of low strain hardening coefficient with high strain rate sensitivity.

Spretnak (17) studied the occurrence of localization of plastic flow, both in tension and torsional straining, in six ultra-high strength low-alloy steels. Testing was carried out at room-temperature at a constant crosshead speed (in tension) or speed of rotation (in torsion). He found little or no correlation between the torsional strain at the onset of the first localization of plastic flow and the corresponding tensile strain, obtained from the maximum-load point in tension, converted to the state of strain of torsion, supporting the contention that the two phenomena of localization of plastic flow are fundamentally different. Reducing the strength level of the steels, in general, increased the strain to first instability. The strain to first instability and the total torsional fracture strain varied greatly among the steels, indicating a possible relationship to fine microstructural differences. Higher stress gradients (smaller specimen diameters) favored smaller values of strain to first instability.

The formation of instabilities and the stress gradient effect were alos found in slow bend tests of U-notch and V-notch bars by Griffis and Spretnak (63). In the tests on notched bars of AISI 4340 steel at an ultimate tensile strength of 180 ksi and higher, instability formation as a

cause of fracture was proposed by these researchers because fracture initiation in the notched bars was a displacive fracture which followed the directions of pure shear (characteristic directions). The V-notch bars exhibited smaller strains to crack initiation than did the U-notch bars, due to the higher stress gradient in the V-notch bars causing earlier instability formation, leading to a smaller strain at the notch at the instant of crack-initiation.

Ernst and Spretnak (64) studied the effect of strain rate on instability behavior in torsion on two ultimate tensile strength levels (180 and 220 ksi) of AISI 4340 steel, unalloyed titanium, and alpha-beta titanium alloy (Ti-13V-11Cr-3Al), and a precipitation-hardened aluminum alloy (7075) at room temperature. They found that the steel showed an important strain-rate dependence of the strain to first instability (Figure 12), whereas the strain to first instability in the non-ferrous alloys was relatively insensitive to shear strain-rate. At a tensile strength level of 180 ksi, the 4340 steel exhibited a critical strain rate below which no instability bands formed before failure, which is in agreement with Rybalko's (53) observation that higher strain-rates favored lower strains to first instability. The non-ferrous alloys consistently formed a single strong instability band immediately prior to failure, and showed strain-hardening response up to the onset of the single strong instability. The high strength steel showed more tolerance to instability bands prior to final fracture, as compared to the non-ferrous alloy. Longitudinal sections through failed specimens demonstrated that the shearing instability bands penetrated completely across the specimen cross section.

Chakrabarti (65) studied the flow and fracture behavior of alpha and alpha-beta brasses at room temperature in both tension and torsional loading. Failure occurred after the onset of instabilities, their movement along the gage length, and the development of a final, strong, instability. This is in contradistinction to the behavior seen in unalloyed titanium and various precipitation-strengthened titanium and aluminum alloys, wherein failure occurred immediately after the development of the first instability (64). Failure to maintain strain-hardening ability (attainment of the ideal plastic state) prior to failure in torsion testing was observed. A dependence of the strain to first instability on grain size was seen, in that the coarser the grain size, the lower the strain to first instability. The observance of instability formation in the two-phase alloys is in contradistinction to a claim by Mostovoy and Polakowski (57) that instability-formation occurs only in single-phase alloys.

Vanecko (66) stated that suppression of instability formation in AISI 4340 steel tested in torsion at cryogenic temperatures under conditions of convective cooling implied that the rapid removal of any localization of heat due to localization of plastic flow is important in the suppression of instability formation. Similar results had been seen by Stüwe and Asbeck (67) in torsion tests on a rimmed low-carbon steel. However, no tests were run in a non-convective cooling medium to determine specimen behavior under these conditions. Vanecko also investigated the nature of the ductile-to-brittle transition in a rimmed low-carbon steel and found that instability formation and loss of elongation in the tensile test of this material, and the loss in ability to strain-

harden as reflected by a decrease in strain-hardening coefficient values with decreasing temperature, were definitely related. This material first underwent Lüders deformation, followed by necking, then by instability-formation along trajectories of pure shear in regions that has previously underwent Lüders deformation. Fracture was, in all cases, associated with one or more instability bands.

Meyerer (68), using AISI 4340 low-alloy steel heat-treated to ultimate tensile strength levels of 168 ksi and 210 ksi, studied the effects of strain rates from 0.15 to 2.2 per minute and temperatures from 200°F to 800°F on the localization of plastic flow and fracture. Several distinct modes of localized plastic flow in torsion tests were seen: (a) diffuse flow, defined as a regional shear gradient over a significant portion of the gage-length, without distinct boundaries; (b) instability interfaces, defined as very thin regions of highly concentrated shear-strain on planes normal to the specimen axis; and (c) instability bands, defined as regions of concentrated shear strain between slowly-advancing interfaces on planes of pure shear, whose appearance were much more gradual transitions of localized flow than instability interfaces. The first were seen at low temperatures and strain-rates, the second at all strain rates at temperatures up to 800°F, and the third at the lower temperatures (to 400°F). The effects of increasing temperature on the strain to first instability and strain to fracture were ambiguous. Longitudinal sections through fractured samples confirmed that instabilities extended completely through the cross section of the samples. Increasing the strain-rate decreased the strain to first instability as had been seen by Rybalko (53) and Ernst and

Spretnak (64). The susceptibility to formation of instabilities was found to be higher for the higher-strength low strain-hardening coefficient material.

Recently, Tanaka and Spretnak (69) investigated the formation and propagation of instability bands during torsion testing of AISI 4340 low-alloy steel at room temperature. They concluded that instability bands formed after saturation of strain-hardening by dispersed carbide particles. Beyond this strain, the matrix becomes transparent to the carbide particles. They observed that the instability interfaces advanced spirally in the axial directions of the sample, and when the interface becomes stationary, fracture was nucleated at an axial distortion in the interface. Fracture by the instability did not involve pore formation and coalescence, so is of the "pure instability" mode.

C. Summary of factors that affect instability formation and propagation.

Observation of the conditions under which instabilities form and propagate lead to several conclusions; (a) instability formation is favored at higher strain rates, (b) instability formation also is favored at higher stress gradients, and (c) instabilities form more easily in materials with a low strain-hardening coefficient and with a low strain rate dependence of flow stress.

MATERIALS AND SPECIMEN PREPARATION

The compositions of the type 304 bar and plate used in the fabrication of specimens is shown in Table 2. Conformance to compositional requirements of ASTM Specification A296-67 was maintained. Also shown is the composition of the weld-metal deposited by the manual metal arc process during the fabrication of a 2 inch thick plate weldment using 1/4" diameter E308-15 electrodes, which was done by the Combustion Division of Combustion Engineering, Inc. according to the conditions summarized in Figure 13. Before machining into test specimens, bar stock was solution annealed for 10 minutes at 2000°F and water quenched. A sensitized microstructure was produced in half of the solution-annealed sample-blanks by heating for 24 hours at 1200°F and water-quenching, and sensitization was confirmed by optical microscopic examination. Specimen configurations for base metal tests are shown in Figure 14, while specimen configurations for weld-metal and weld-joint tests are shown in Figure 15. After heat-treating or welding, specimens were machined to the configurations shown in Figures 14 and 15. After machining, the gage sections were ground to reduce out-of-roundness and taper to 0.0005 inch or less. The gage sections then were polished on a lathe through 4/0 grade metallographic paper and with 5 μm alumina to eliminate surface scratches that would act as stress raisers. Immediately before testing, the diameters of the gage sections of the torsion specimens were measured

with a micrometer at three positions along the gage section and at 120° circumferential intervals at each position. Also, each gage section is marked with three ink lines. These ink lines are equally spaced around the circumference of the bar and are parallel to the specimen axis. They aid in the identification of localized plastic flow during subsequent testing.

EQUIPMENT DEVELOPMENT

A schematic diagram of the elevated-temperature torsion-testing apparatus is shown in Figure 16. The same torsion apparatus was used for room-temperature tests, with the gas-drying train disconnected and the specimen furnaces removed.

The main specimen furnace is a three-zone, 2-1/2 inch wide, water-cooled, radiant heater (Research Inc., Model ZH3A), which was modified to permit viewing of the torsion specimens during testing. Power to the center zone was manually controlled by a variable autotransformer (Variac, Type 126) and the end zones were controlled by temperature controllers (Research Inc., Model 624A) and power controllers (Model 632 Phasers).

The specimen was centered in a 3-1/8 inch-long by 1 inch diameter Vycor tube that had end seals to permit an argon flow of about 4 cc/s at a small positive pressure, and specimen rotation during testing. The tank argon was purified in a drying train consisting of separate bottles containing Drierite (to remove moisture), Ascarite (to remove CO_2) and anhydrous magnesium perchlorate (to remove moisture). The argon then flowed through a U-tube immersed in a dry-ice/methanol mixture that cooled the gas to -108°F (-78°C) to remove moisture. The argon was finally passed through light copper trimmings that were maintained at 275°C (527°F) to remove oxygen.

The specimen temperature was monitored by two 0.020-inch diameter stainless-steel sheathed and grounded chromel-alumel thermocouples (Omega

Engineering, Inc., SCA55-020G-6). They were fed through glass capillary tubing to maintain alignment and lightly held against the specimen gage section at the positions of the furnace end zones with rubber bands, shown in Figure 17. The thermocouple leads were connected to the end-zone temperature controllers.

To produce a uniform temperature (± 5°F) (± 3°C) along the test specimen gage length, auxilliary resistance heaters were constructed and installed between the radiant furnace and the ends of the specimens. The heaters were required to reduce the flow of heat of the ends of the gage section, which had previously resulted in a higher temperature at the center of the gage section than at the ends. These heaters were constructed by winding 0.036 inch diameter Kanthal 1A wire on a 1-5/16 inch long by 1-1/8 inch I.D. threaded ceramic spool. The heater core was positioned concentrically in a 1-5/16 inch long by 6 inch diameter, Schedule 40, aluminum pipe and the empty volume was filled with Fibrefrax insulation. Heater end-plates with a 3/4 inch diameter opening, and sliding doors with a 1/2 inch diameter opening, were constructed from 1/8 inch thick Transite asbestos board. These heaters were positioned on each side of the radiant heating furnace, as shown diagramatically in Figure 16 and pictorially in Figure 18. Power to each heater was controlled by a variable autotransformer (Variac Powostats Types 116B and 126).

The temperature-controller and auxilliary-heater settings required for each test temperature were established using a test specimen having a 1/8 inch diameter hole along its axis. A chromel-alumel thermocouple, with the lead wires fed through a 17 inch long by 3/32 inch diameter 2 hole alumina protection tube, was inserted in the axial hole with the

welded bead in contact with the hole surface. Temperatures were measured at three positions along the reduced gage section of the calibration bar, using a millivolt potentiometer (Leeds and Northrup Catalogue Number 8686) and the settings were adjusted to achieve a temperature within 5°F (3°C) of the desired test temperature along the reduced gage section. The controller and heater settings were recalibrated after about each 6 torsion tests at a given test temperature and before beginning tests at a different temperature. Using this procedure, the specimen temperatures were maintained within ± 10°F (± 6°C) of the desired test temperatures.

Twist was applied by a 3/4 hp. precision variable-speed d.c. motor that was adjustable from about 500 to 2070 rpm. Various combinations of spur gears and worm gear reducers allowed shear-strain rates in the range of 0.004 to 8.7 min^{-1} to be achieved.

The torque was measured by the voltage output of four resistance strain gages bonded to the surface of a tubular load cell and connected to a bridge amplifier (Honeywell Accudata, Model 113). The calibration factor for this load cell was determined by application of static moments from 8.8 to 970 in-lb and found to be 1.45 μV/in-lb/V excitation. The torque transducer was attached to the non-rotating grip of the apparatus. This grip was mounted in ball-bearing bushings and was free to move axially so that axial loads were not imposed during torsion tests. Torque was continuously recorded during each test on a multi-channel oscillographic recorder (Honeywell, Model 906C).

EXPERIMENTAL PROCEDURE

During each torsion test, the following basic data were obtained:

(1) Specimen gage-section temperature at the start of each test,

(2) Shear strain rate at the specimen surface, $\dot{\gamma}$,

(3) Shear strain at the onset of localized flow, γ_i,

(4) Torque versus time throughout each test,

(5) Shear strain at fracture, γ_f.

The shear strain rates, $\dot{\gamma}$, were computed from the measured twist rates using the following equation:

$$\dot{\gamma} = \frac{r}{\ell} \dot{\theta}$$

where r is the radius of the gage section in inches, ℓ is the gage length in inches, and $\dot{\theta}$ is the twist rate in radians per minute. Twist rates were determined from timed rotation of the rotating head.

The shear strain at the onset of localized flow was calculated as the product of the strain rate, which was constant, and the time from the beginning of the test to the occurrence of the instability. The point of instability was indicated by an event marker connected to a different channel of the recorder than that used to record torque. Timing lines recorded by the oscillograph (100, 10, or 1 line(s) per minute) aided in accurate measurement of time during each test. The oscillograph chart speed (0.2, 1, 5, or 25 incheses per minute) was selected to provide a

record at least 12 inches long, and usually about 36 inches long, so that torque and strain values could be accurately measured.

After each elevated-temperature test specimen was installed in the apparatus, the following steps comprised the testing sequence:

(1) The glass cell was purged with high-purity argon for at least 30 minutes before heating was begun;

(2) The radiant-heating furnace and auxilliary resistance heaters were turned on and the specimen was brought to the test temperature in 1 to 1 1/2 hours, in accordance with the results of the calibration experiments;

(3) The motor-speed setting was adjusted to the desired value and the proper gears were installed for speed reduction;

(4) The strain-gage bridge amplifier was zeroed and set for the appropriate full-scale torque value;

(5) The oscillograph was set at the desired chart speed and timing-line spacing;

(6) The motor was started and the specimen surface was observed throughout the test in order to indicate the onset of localized flow on the recorder and also to permit description of instability behavior. The rotating head was timed.

(7) After the specimen fractured, the testing-equipment components were turned off, the recording chart was marked for identification, and the specimen was removed for diameter measurement and subsequent examination;

(8) The torque-time recording was analysed to determine the shear stress-shear strain curve.

RESULTS

1. Base Metal

Single torsion tests were conducted on specimens in the solution-annealed and solution-annealed plus sensitized conditions at 75°F (24°C), 500°F (260°C), 1000°F (538°C), and 1200°F (649°C) at nominal shear strain-rates of 0.07, 0.6, 2.5, and 4.8 per minute. Single tests were also conducted on solution-annealed specimens at a strain-rate of 2.5 per minute at temperatures of 400°F (204°C) and 600°F (316°C). These specimens had gage-sections that were 0.300 inches in diameter, which had previously been adopted as the "standard" gage diameter. Results of these tests are summarized in Table 3. To assess the effects of varying the stress-gradient on the strain to fracture and strain to first instability, additional tests were conducted at 500°F (260°C) and over the entire strain-rate envelope on solution-annealed bars with gage-diameters of 0.250 inches and 0.200 inches, respectively. Results of these tests are summarized in Table 4.

Strain to fracture is presented as a function of temperature in Figures 19 and 20 and strain rate in Figure 21. For all four strain-rates for the solution-annealed material, and for the fastest three strain-rates for the sensitized material, the strain to fracture went through a maximum at 500°F (260°C) and decreased monotonically with temperature to 1200°F (649°C). Sensitized material tested at the slowest strain-rate (0.07 per minute) showed approximately equal strain-to-

fracture values at 75°F (24°C) and 500°F (260°C, with a monotonic decrease of strain to fracture with increasing temperature to 1200°F (649°C).

As a function of strain-rate, the strain to fracture values follow no clear-cut pattern at 75°F (24°C) and 500°F (260°C); being alternately lower for solution-annealed material than for sensitized material at low strain-rates at 75°F (24°C) and high strain rates at 500°F (260°C). Conversely, the strain to fracture for solution-annealed material was higher than that shown by sensitized material at high strain-rates at 75°F (24°C) and low strain-rates at 500°F (260°C). However, for all strain-rates at 1000°F (538°C) and 1200°F (649°C), the strain to fracture values were higher for sensitized material than for solution-annealed material.

Strain to first instability is presented as a function of temperature in Figures 19 and 20 and of strain rate in Figure 22. For the fastest two strain-rates (4.8 and 2.5 per minute), the strain to first instability for both material-conditions went through a maximum at 500°F (260°C) and then decreased monotonically with increasing temperature. For the next slowest strain-rate (0.60 per minute), the solution-annealed material showed a general trend to decreasing values of strain to first instability with increasing temperature. As the same strain-rate (0.60 per minute), the sensitized material showed a maximum in the strain to first instability at 1000°F (538°C). At the slowest strain-rate employed (0.07 per minute), instabilities were seen in the solution-annealed material only at 1200°F (649°C), and in the sensitized material at both 1000°F (538°C) and 1200°F (649°C). For both material-conditions, the strains to first instability at 1200°F (649°C), the value of strain to

first instability was the highest recorded for the sensitized material at that temperature.

The values of strain to first instability as a function of strain-rate follow no clear-cut pattern (Figure 22). At 1000°F (538°C), the strain to first instability decreased with increasing strain-rates for both material-conditions. At 1200°F (649°C), the strain to first instability increased slightly with increasing strain-rates for both material conditions. At 75°F (24°C) and 500°F (260°C), the strain to first instability for sensitized material went through a maximum at a strain-rate of about 2.5 per minute, then decreased with a further increase in strain-rate. For solution-annealed material, the strain to first instability decreased with increasing strain-rate at 75°F (24°C) and increased with increasing strain-rate at 500°F (260°C).

Strain after onset of instability, defined as the difference between the strain to fracture and the strain to first instability, is presented as a function of temperature in Figure 23 and of strain rate in Figure 24. Consideration of this parameter was undertaken in an attempt to assess the ability of the steel to resist failure once an instability has formed. As a function of temperature, and for the fastest three strain-rates, the sensitized material showed a maximum in this parameter at 500°F (260°C) with a monotonic decrease with temperatures to 1200°F (649°C). The solution-annealed material showed similar behavior for strain-rates of 2.5 and 0.6 per minute. For a strain-rate of 4.8 per minute, the solution-annealed material showed a slightly higher value of this parameter at 75°F (24°C) than at 500°F (260°C), with the usual monotonic decrease with temperatures above 500°F (260°C).

The strain-rate dependence of this parameter is complex. Sensitized material tested at 75°F (24°C) and 500°F (260°C) and solution-annealed material tested at 500°F (260°C) show a minimum in this parameter at a strain-rate of about 2.5 per minute. Solution-annealed material tested at 75°F (24°C) shows a monotonic increase in this parameter with increasing strain-rate. For both material-conditions tested at 1000°F (538°C), this parameter appears to go through a maximum at a strain-rate of about 0.6 per minute, with the sensitized material better able to resist the onset of fracture once an instability had formed. For both material-conditions tested at 1200°F (649°C), this parameter went through a slight maximum at a strain-rate of 0.6 per minute. Little difference between the behavior of sensitized and solution-annealed material conditions was seen at 1200°F (649°C).

2. Stress Gradient Effects

Effect of a stress-gradient on the flow and fracture behavior of type 304 stainless steel bar is discussed in terms of the variation of strain to fracture, strain to first instability, and strain after first instability with increasing bar-diameter (decreasing stress gradient).

Strain to fracture as a function of increasing bar diameter (decreasing stress gradient) at 500°F (260°C) is presented in Figure 25. For the fastest strain-rate, 4.8 per minute, the strain to fracture increased with increasing stress-gradient. For the remaining strain rates of 2.5, 0.6, and 0.07 per minute, the strain to fracture decreased with increasing stress gradient. Strain to first instability as a function of increasing bar-diameter (decreasing stress-gradient) at 500°F (260°C) is

presented in Figure 25. For strain-rates of 4.8 and 2.5 per minute, this parameter decreased with increasing stress-gradient. For a strain-rate of 0.6 per minute, no consistent variation of this parameter with increasing stress-gradient was seen. No instabilities were seen at a strain-rate of 0.07 per minute.

Strain after the first instability, defined as the difference between the strain to fracture and the strain to first instability, is presented as a function of increasing bar-diameter (decreasing stress-gradient) in Figure 25. Consideration of this parameter was undertaken in an attempt to assess the ability of the steel to resist failure once an instability has formed. For strain-rates of 4.8 and 2.5 per minute, this parameter increased with increasing stress-gradient. For a strain rate of 0.6 per minute, this parameter decreased, then increased with increasing stress-gradient. Hence, even in the presence of increasing stress-gradients, the material seemed able to resist fracture once localized plastic flow had begun.

3. Welded Plate

Torsion tests were conducted on specimens cut from the 2 inch thick welded plate previously described in the section entitled "Materials and Specimen Preparation." Two types of specimens were used: all weld-metal specimens, where a 1 inch long by 0.300 inch diameter gage-length was located completely in the fusion-zone of the multi-pass weldment (Figure 15a); and weld-joint specimens, where a 2.5 inch long by 0.300 inch diameter gage-length was centered on the fusion-zone, with adjacent regions of heat-affected zone and base-metal contained outboard of the

fusion-zone (Figure 15b). Single tests were conducted on as-welded specimens at 75°F (24°C), 500°F (260°C), 1000°F (538°C), and 1200°F (649°C) at nominal shear strain-rates of 4.8, 0.6, and 0.07 per minute. Results of these tests are summarized in Table 5. Deformation during torsion testing at all temperatures and strain-rates was unique in that the large-grained weld-metal underwent extremely heterogeneous plastic flow with each grain standing out in relief soon after the start of torsion testing. In all cases, failure was either entirely in the fusion-zone; or partially in the fusion-zone, partially in the heat-affected zone.

Strain to fracture as a function of temperature is summarized in Figure 26 for all weld-metal samples and in Figure 27 for weld-joint samples. For all weld-metal samples, minimum values of strain to fracture were seen at 1000°F (538°C) for all strain-rates employed. Maximum values of strain to fracture were seen at 1200°F (649°C) for all strain rates, with the sample tested at a strain rate of 4.8 per minute showing a subsidiary maximum at 500°F (260°C). For weld-joint samples, minimum values of strain to fracture were seen at 1200°F (649°C) for all strain-rates used. For strain-rates of 0.6 and 0.07 per minute, maxima in the strain to fracture: temperature plots of weld-joint samples were seen at 500°F (260°C). Weld-joint samples tested at a strain-rate of 4.8 per minute showed a pronounced maximum at 1000°F (538°C) in the strain to fracture.

The strain-rate dependence of this parameter is summarized in Figure 28 and is complex. For all weld-metal samples, the strain to fracture increased slightly with increasing strain-rate at temperatures of 75°F (24°C) and 500°F (260°C). At 1000°F (538°C), the strain to

fracture of all weld-metal samples is essentially independent of strain rate. At 1200°F (649°C) strain to fracture: strain-rate relationship for all weld-metal samples went through a slight maximum at a strain-rate of 0.6 per minute. For weld-joint samples, the strain to fracture at 75°F (24°C) and 1000°F (538°C) increased with increasing strain rate. At 500°F (260°C), the strain to fracture for weld-joint samples went through a shallow minimum at a strain-rate of 0.6 per minute, while at 1200°F (649°C), the weld-joint sample strain to fracture values went through a shallow maximum at the same strain rate.

Strain to first instability as a function of temperature is summarized in Figure 26 for all weld-metal samples and in Figure 27 for weld-joint samples. For all weld-metal samples, the minimum values of strain to first instability were experienced at 75°F (24°C). For a strain-rate of 4.8 per minute, a maximum value of this parameter for all weld-metal samples, was observed at 1000°F (538°C), while for slower strain rates, maximum value of this parameter was seen at 1200°F (649°C). For weld-joint samples, minimum values of the strain to first instability were seen at 1200°F (649°C) for a strain rate of 4.8 per minute and at 75°F (24°C) for slower strain rates. Maximum values of the strain to first instability for weld-joint samples were seen at 1000°F (538°C) for samples tested at strain-rates of 4.8 and 0.07 per minute, and at 1200°F (649°C) for samples tested at a strain-rate of 0.6 per minute.

The strain-rate dependence of this parameter is summarized in Figure 29 and increased with increasing strain-rate over the entire range of temperatures for all weld-metal samples. For weld-joint samples, the strain to first instability increased with increasing strain-rate at 75°F

(24°C), 500°F (260°C), and 1200°F (649°C). At 1000°F (538°C), the value of this parameter for weld-joint samples went through a shallow minimum at a strain-rate of 0.6 per minute, then increased sharply to a maximum at a strain rate of 4.8 per minute.

Strain after first instability, defined as the difference between the strain to fracture and the strain to first instability, is presented as a function of temperature in Figure 30. Consideration of this parameter was undertaken in an attempt to determine the ability of the weld metal and weld-joint to resist failure once instabilities had formed. As a function of temperature for all weld-metal samples this parameter went through maxima at 1200°F (649°C) and minima at 1000°F (538°C) for all strain rates employed. For weld-joint samples, this parameter went through minima at 1000°F (538°C) and maxima at 500°F (260°C) for samples tested at strain-rates of 0.6 and 0.07 per minute. Weld-joint samples tested at a strain-rate of 4.8 per minute recorded a minimum value of this parameter at 1200°F (649°C) and a maximum value at 1000°F (538°C).

The strain-rate dependence of this parameter is summarized in Figure 31. For all weld-metal samples, the strain after instability was essentially constant at 75°F (24°C), and decreased with increasing strain-rates at 500°F (260°C), 1000°F (538°C), and 1200°F (649°C). For weld-joint samples, this parameter increased with increasing strain-rate for samples tested at 75°F (24°C) and 1000°F (538°C), decreased with increasing strain-rate for samples tested at 1200°F (649°C), and went through a shallow minimum for samples tested at 500°F (260°C).

4. Comparison of Welded and Unwelded Properties

Comparison with unwelded (solution treated) bar stock properties was accomplished by taking the ratio of the particular parameter for a welded sample to that value for solution-annealed bar-stock and analyzing the behavior of the resulting ratios as functions of temperature and shear strain-rate.

The ratio of weld-metal strain to fracture to base metal strain to fracture as a function of temperature is summarized in Figure 32. For all weld-metal samples, the values of this parameter were less than 0.5 for samples tested at all strain rates at temperatures from 75°F (24°C) to 1000°F (538°C). At 1200°F (649°C), the values of this parameter for all weld-metal samples increased to approximately 1.0 for samples tested at strain-rates of 0.07 and 0.6 per minute and to about 1.5 for the samples tested at a strain-rate of 4.8 per minute. Maximum values of this parameter for all weld-metal samples were seen at 1200°F (649°C) and minimum values at 500°F (260°C) for samples tested at all three strain-rates. For weld-joint samples, values of this parameter were less than 0.5 for all strain-rates except the sample tested at 1000°F (538°C) and 4.8 per minute, which exhibited a value of 1.54. At 1200°F (649°C), the values of the parameter for weld-joint samples increased for the samples tested at strain-rates of 0.6 and 0.07 per minute, and decreased for the sample tested at a strain-rate of 4.8 per minute. Maximum values of this parameter for weld-joint samples were seen at 1200°F (649°C) for the samples tested at the slower strain-rates, and at 1000°F (538°C) for the sample tested at a strain-rate of 4.8 per minute. Minimum values of this parameter for weld-joint samples were seen at 75°F (24°C)

for the samples tested at the two slower strain-rates, and at 500°F (260°C) for the samples tested at 4.8 per minute.

The strain-rate dependence of this parameter is summarized in Figure 33. At temperatures of 75°F (24°C) to 1000°F (538°C), the value of this parameter for all weld-metal samples increased with increasing strain-rate and never exceeded 0.50. At a temperature of 1200°F (649°C), the value of this parameter for all weld-metal samples decreased with increasing strain rate, from 1.54 at 0.07 per minute to 1.0 at 4.8 per minute. For weld-joint samples tested at temperatures of 75°F (24°C) to 1000°F (538°C), the value of this parameter increased with increasing strain-rate and never exceeded a value of 0.50 except for the sample tested at a strain-rate of 4.8 per minute and a temperature of 1000°F (538°C) wherein the observed value was 1.54. At a temperature of 1200°F (649°C), values of this parameter for weld-joint samples lay between 0.05 and 0.85, with a minimum at a strain-rate of 0.6 per minute.

The ratio of weld-metal strain to first instability to base-metal strain to first instability as a function of temperature is summarized in Figure 34. For all weld-metal samples, the value of this parameter increased to 1000°F (538°C), then decreased, for samples tested at a strain rate of 4.8 per minute. Values ranged from 0.30 to 0.50. For all weld-metal samples tested at a strain-rate of 0.6 per minute, the value of this aprameter increased from about 0.06 at 75°F (24°C) to 0.60 at 1200°F (649°C). Minimum values of this parameter for all weld-metal samples were attained at 75°F (24°C) while maximum values were attained at 1000°F (538°C) for samples tested at a strain-rate of 4.8 per minute and at 1200°F (649°C) for samples tested at a strain-rate of 0.60 per

minute. For weld-joint samples, the values of this parameter for samples tested at a strain-rate of 4.8 per minute went through a minimum of about 0.30 at 500°F (260°C), then rose to a maximum of about 1.34 at 1000°F (538°C), then decreased with an increase in temperature to 1200°F (649°C). For weld-joint samples tested at a strain-rate of 0.6 per minute, the value of this parameter increased with increasing temperature from a minimum of about 0.04 at 75°F (24°C) to a maximum of 0.30 at 1200°F (649°C).

The strain-rate dependence of this parameter is summarized in Figure 35. For all weld-metal samples this parameter increased with increasing strain-rate at temperatures between 75°F (24°C) and 1000°F (538°C), attaining values less than 0.50, except for the sample tested at 1000°F (538°C) and a strain-rate of 4.8 per minute, which exhibited a value of about 0.85. For all weld-metal samples tested at 1200°F (649°C), this parameter was essentially independent of strain-rate, and was about 0.55. For weld-joint samples, this parameter increased with increasing strain-rate at temperatures between 75°F (24°C) and 1000°F (538°C), with values less than 0.50 except for the sample tested at 1000°F (538°C) and a strain-rate of 4.8 per minute, which exhibited a value of about 1.44. For weld-joint samples tested at 1200°F (649°C), this parameter was essentially independent of strain-rate, and was about 0.35.

The ratio of weld-metal strain after first instability to base-metal strain after first instability as a function of temperature is summarized in Figure 36. For all weld-metal samples tested at a strain-rate of 4.8 per minute, this parameter decreased as the temperature increased from 75°F (24°C) to 1000°F (538°C), then increased as the

temperature increased to 1200°F (649°C). Values ranged from a minimum of 0.15 at 1000°F (538°C) to a maximum of 1.52 at 1200°F (649°C). For all weld-metal samples tested at a strain-rate of 0.6 per minute, the value of this parameter decreased slowly with increasing temperature from a maximum of 3.95 at 75°F (24°C) to a minimum of 0.18 at 500°F (260°C), then increased as the temperature increased to 1200°F (649°C). For weld-joint samples tested at a strain-rate of 4.8 per minute, this parameter increased with increasing temperature from a minimum value of 0.38 at 75°F (24°C) to a maximum value of 1.66 at 1000°F (538°C) then decreased with a further increase in temperature to 1200°F (649°C). For weld-joint samples tested at a strain-rate of 0.6 per minute, this parameter decreased with increasing temperature from a maximum value of 4.3 at 75°F (24°C) to a minimum value of 0.31 at 500°F (260°C) then increased slightly with increasing temperatures to 1200°F (649°C).

The strain-rate dependence of this parameter is summarized in Figure 37. For all weld-metal samples, this parameter decreased with increasing strain-rate at temperatures of 75°F (24°C) and 1000°F (538°C), was essentially independent of strain-rate at 500°F (260°C) with a value of about 0.2, and at 1200°F (649°C) went through a minimum at a strain-rate of 0.6 per minute. For weld-joint samples, this parameter decreases with increasing strain-rate at 75°F (24°C), increased with increasing strain-rate at 500°F (260°C) and 1000°F (538°C), and went through a minimum at a strain-rate of 0.6 per minute at 1200°F (649°C).

METALLOGRAPHY

1. Specimen Preparation

Preparation of samples for metallographic examination consisted of sectioning, mounting, grinding, rough polishing, fine polishing, and etching with suitable reagents. Sectioning was performed using a silicon-carbide cutoff wheel, while flooding the sample with an excess of cold water to prevent over-heating of the sample. Samples were mounted in an epoxy mounting material (Buehler No. 20-8130 AB) with an addition of 15 volume percent 5 micron alumina powder to increase the hardness of the mount and aid in retention of the edges of the sample during subsequent polishing operations. After curing the epoxy, which took 24 hours at room temperature, the samples were surface-ground, removing 0.005 inches per pass so as not to cold-work the stainless-steel, until a sufficiently-wide section of the gage-length was exposed. Rough polishing of samples was accomplished on power-rotated water-cooled wheels, using 240, 320, 400, and 600 grit silicon carbide paper. Fine polishing of samples was accomplished on power-rotated wheels, using Buehler Ltd. Microcloth cloths and polishing with 9 micron, 6 micron, and 3 micron diamond-paste. Between each polishing operation, samples were cleaned in an ultrasonic agitator and rinsed with methanol. Etchants used were glyceregia (2 parts by volume HCl, 2 parts glycerine, 1 part HNO_3) for general microstructural details, and oxalic acid (10 volume percent in

water) for developing the microstructure of sensitized material. Examination was performed on an American Optical Company Model 2400 metallograph.

2. Examination of Incoming Material

The microstructure of solution-annealed bar is shown in Figure 38 and consists of a relatively coarse-grained (ASTM 5) austenitic microstructure with randomly-distributed carbides. The hardness was 280 Vickers. Figures 39 and 40 show the microstructure of solution-annealed and sensitized bar etched with glyceregia and oxalic acid, respectively. The former microstructure is quite similar to that exhibited by the solution-annealed bar (Figure 38), while the latter microstructure clearly shows evidence of extensive sensitization caused by grain boundary precipitation of $M_{23}C_6$ carbides, due to the preferential attack of grain-boundary regions by the oxalic acid. Note also the outlining of some twin-boundaries (Figure 40) by precipitation of $M_{23}C_6$ carbides. Figure 41 is representative of fusion-zone microstructures in the multi-pass manual metal-arc weld supplied by Combustion Engineering, Inc. Note the as-deposited coarse-grained weld-metal adjacent to the fine-grained weld-metal which has been remelted and re-solidified by a subsequent weld-pass. Figure 42 is a typical region of the heat-affected zone in the two-inch thick plate used in fabrication of the welded-joint. Note the presence of a lamination, probably associated with carbonitride inclusions elongated in the rolling direction, which may have been opened by tessellated stresses developed by the multiple thermal-cycles associated with fabrication of the multi-pass weldment. Figure 43 shows a typical section at the fusion-line, and presents evidence of a small fusion-line

hot tear as well as another lamination in the original base-plate which appeared to be associated with a possible heat-affected zone crack.

3. Base Metal Specimens

Microstructures of solution-annealed specimens after torsion-testing at various temperatures and shear strain-rates are presented in Figures 44 through 61. Development of grain-boundary contrast after heavy plastic straining was quite difficult, due to the very rapid general attack by all of the etchants employed. Figures 44 and 45 are representative of the material's appearance after extensive torsional-deformation at room-temperature; rotations of grains and inclusions from the original specimen axis (Figure 44) and formation of many small secondary cracks that are aligned with the fibre-orientation of the specimen (Figure 45). Some of these cracks appear to have originated from inclusions, probably "MC" type carbonitrides, and are propagating in a trans-granular manner along the fibre-axis in the heavily plastically-deformed austenitic matrix (Figure 45) as suggested by Spretnak (18). Figure 46 illustrates the extensive secondary cracking associated samples that exhibited high values of strain to fracture, in this case a fracture strain of 4.00 at room temperature. Figure 47 illustrates the association of a growing crack with inclusions in the austenitic matrix. Extensive cracking parallel to the main crack in Figure 46, in addition to blunting at the growing crack tip, are evidence of the crack's growth being driven by continual plastic straining. Figures 48 and 49 depict a typical room-temperature: high strain-rate fracture. Note the growth of a secondary crack in from the fracture surface by formation of pores at inclusion:

matrix interfaces and the coalescence of these pores ahead of the advancing crack-tip (Figure 49). The inherent good ductility of this material is evidenced by the blunt, rounded, nature of the growing crack-tip.

Details of the fracture-surface (Figure 50) and interior (Figure 51) of the solution-annealed sample that exhibited the highest strain to fracture of all bar samples (6.76 at a temperature: strain-rate combination of 500°F (260°C): 0.62 per minute) show the extensive secondary-cracking associated with a high-ductility fracture (Figure 50). Figure 51 shows that the mode of crack-initiation is by formation of voids at inclusion: matrix interfaces and growth of cracks by localization of plastic-flow along stream-lines in the austenite matrix. Careful examination of Figure 51 failed to reveal any evidence of fracturing of inclusions. Figures 52 and 53 show the microstructural details of a sample tested at 500°F (260°C) and a very slow strain-rate that failed without any visual evidence of instability formation. Note the example of extensive secondary cracking (Figure 53) which was seen all throughout the gage-length. Figure 53 shows that cracks grew from inclusion to inclusion by localization of plastic-flow along stream-lines in the austenitic matrix.

Figures 54 through 58 show microstructural features of a sample tested at a temperature: strain-rate combination of 1000°F (538°C): 4.72 per minute. Note the extreme amount of rotation of the grain-structure and inclusions away from the original bar axis (Figure 54), which was in evidence throughout the entire diameter of the bar. Cracks appeared to nucleate both at inclusion: matrix interfaces within the grains (Figure

56) and at pores formed at carbide-free grain-boundaries (Figure 57) and grow by localization of plastic-flow along stream-lines in the austenitic matrix. No clearcut evidence of inclusion-cracking was seen.

Figures 59 through 61 show microstructural features of a sample tested at a temperature: strain-rate combination of 1200°F (649°C) :: 0.073 per minute. Note the extreme amount or rotation of the grain-structure from the original bar-axis by torsional deformation (Figure 59), as well as the localization of plastic flow between two cracks growing towards each other in a transgranular manner. This photomicrograph, taken just behind the fracture surface on the bar center-line, illustrates the extreme localization of plastic flow that occurred within the strong-instability that led to failure. Contrast the heavily-worked appearance of the microstructure in Figure 59 with that in Figure 60, which was also taken along the bar center-line, but at a location near the specimen shoulder, which having not retained evidence of localized plastic flow, shows only a uniform rotation of grains and inclusions as a result of torsional deformation. Although some rotation of grains away from the original bar-center line is evident in Figure 60, as well as a few small cracks, the relatively undeformed microstructure of Figure 60, compared with that of Figure 59 strikingly illustrates the microstructural effects of localization of plastic-flow prior to failure. Figure 61, an enlargement of the region around the growing tip of one of the cracks shown in Figure 59, clearly illustrates the transgranular nature of the fracture, a common feature in solution-annealed material even in the presence of some intergranular carbides that were found on heating to and testing at 1200°F (649°C): 0.073 per minute.

Microstructures of solution-annealed and sensitized specimens, after torsion-testing at various temperatures and shear strain-rates, are presented in Figures 62 through 76. Microstructural features of a sample tested at a temperature: strain-rate combination of 75°F (24°C): 2.34 per minute are shown in Figures 62 through 65. At the fracture-surface (Figure 62), the grains and inclusions have been rotated almost 90 degrees from the original bar-axis by the extreme localization of plastic-flow within the instability that was associated with the fracture. This extreme rotation of grains and inclusions was evident across the entire diameter of the sample at the fracture-surface, not just near the external surface of the bar where the maximum shear-strain would be expected during uniform deformation of the specimen. Figure 63 illustrates the much less intense deformation that occurred far from the fracture-surface. Formation of microcracks at carbide networks at grain-boundaries and twin-boundaries are shown in Figures 64 and 65, as well as at isolated inclusions within the interior of the grain. Propagation of the cracks seems to take place both along the intergranular carbide networks (Figure 64) and within the interior of the grain (Figures 64 and 65). In the latter case, the cracks appear to grow from inclusion to inclusion within the grain, or from a site within the grain to the near-by grain-boundary carbide network that is favorable oriented with respect to a plane of maximum shear strain. Only a moderate number of secondary cracks were seen in this sample, which failed at a strain to fracture of 2.32, which was low for base-metal specimens tested at room-temperature.

Figures 66 and 69 summarize microstructural features of a sample tested at a temperature: strain-rate combination of 500°F (260°C): 0.065

per minute. This sample, which failed at a relatively high strain to fracture of 4.56, which was a maximum for sensitized bar-stock, showed evidence of extreme rotation of grains and inclusions due to torsional deformation, both at the outermost surface of the bar at the fracture (Figure 66) and near the surface of bar far from the fracture-surface (Figure 67). Near the bar center-line, little evidence of plastic-flow in the form of grain-rotation was seen (Figure 68). The details of the fracture are presented in Figure 69, wherein pores are seen forming at both intergranular carbide networks and at isolated carbides and other inclusions within the grains, by either decohesion at the austenite: carbide interface or possibly cracking of the relatively hard, brittle, carbides as has been reported by Barnby (34) for short-time tensile deformation of sensitized Type 316 stainless steel, and by Barnby and Peace (40) for low cycle fatigue-deformation of the same material. Growth of the cracks is predominantly intergranular, with an occasional transgranular excursion along a region of highly-localized plastic-flow, usually towards another crack or accumulation of pores at a grain-boundary.

Figures 70 and 71 present microstructural features of a sample tested at a temperature: strain-rate combination of 500°F (260°C): 2.64 per minute. This sample, which failed at a relatively high strain to fracture of 5.78 appeared to initiate pores mostly at grain boundary carbide networks and occasionally at isolated inclusions within the grains (Figure 71). Growth of cracks appeared to be mainly intergranular, with occasional transgranular excursions towards an inclusion or an isolated microcrack in a near-by grain-boundary.

The details of a sample tested at 1000°F (538°C): 4.81 per minute are presented in Figures 72 and 73 which depict the propagation of a secondary crack just behind the fracture surface by linking up with a crack emanating from a small inclusion. Other details of the fracture and associated microstructure were quite similar to Figures 70 and 71.

In Figures 74 through 76 are presented the pertinent microstructural features of a sample that was tested at a temperature: strain-rate combination of 1200°F (649°C): 0.0731 per minute. Contrast the extreme rotation of grains and inclusions within the instability that was associated with the fracture (Figure 74) with the relatively light amount of grain and inclusion re-orientation shown in Figure 76, which was taken near the bar-surface far from the fracture-location. This clearly illustrates the microstructural differences produced by localization of plastic-flow. In Figure 74 is also illustrated how pores form and grow in an intergranular manner along grain-boundary carbide networks. Note also the extreme localization of plastic flow on the micro-level as two cracks grow towards each other (Figure 75).

4. Welded Specimens

Microstructures of all weld-metal specimens after torsion-testing at various temperatures and strain-rates are presented in Figures 77 through 87. In Figures 77 and 78 are shown microstructural features of a weld-metal sample that was tested at a temperature: strain-rate combination of 75°F (24°C): 0.0688 per minute, and recorded a strain to first instability value of 0.0624, the lowest of any weld-metal sample. Note the intense localization of plastic flow within the instability associated with failure

failure (Figure 77). Examination of Figure 78 reveals the formation of voids within interdendritic ferrite pools, and the growth of these voids into cracks, first within the ferrite, then by intense localization of plastic-flow in the austenitic matrix between microcracks within near-by ferrite-pools. Similar types of fracture of duplex austenitic-ferrite weld-metals on types 304 and 316 base metals have been reported for isothermal fatigue-loading in the range of room temperature to 1100°F (593°C) by Shahinian, Smith, and Hawthorne (70) and James (71) and for stress-rupture loading at 1200°F (649°C) by Goodwin, Cole, and Slaughter (72).

Figures 79 through 81 present pertinent microstructural features of two weld-metal samples tested at 500°F (260°C) and strain-rates of 4.85 per minute (Figures 79 and 80) and 0.0651 per minute (Figure 81), respectively. The former sample exhibited the highest values of strain to first instability and strain to fracture recorded at 500°F (260°C) while the second sample exhibited the lowest values of these parameters at 500°F (260°C). In the former case, extensive secondary cracking, both at the fracture surface (Figure 79) and far away from it, was seen. Note the extensive cracking parallelling both sides of the secondary crack. Cracks initiated by void-formation in ferrite pools and grew by propagation of voids, first within the ferrite pools, then by localization of plastic flow in the austenitic matrix between void-filled ferrite pools. In the latter case, only a few secondary cracks were seen on the fracture surface (Figure 81) and none in the interior of the bar.

Microstructural features developed in weld-metal samples tested at 1000°F (538°C) and 1200°F (649°C) were quite similar. In Figures 82 through 87 are presented pertinent microstructural features for two weld-

metal samples tested at 1200°F (649°C). The former sample was tested at a strain rate of 4.80 per minute and exhibited the highest strain to first instability and lowest strain to fracture of weld-metal samples tested at 1200°F (649°C), while the latter was tested at a strain-rate of 0.580 per minute and exhibited the lowest strain to first instability and highest strain to fracture of weld-metal samples tested at 1200°F (649°C). Figures 82 and 83 illustrate the paucity of secondary crack-formation along the fracture-surface of the low strain to fracture sample. Note the propagation of one of these cracks along interdendritic ferrite pools (Figure 83). Little secondary crack-development was seen away from the fracture-surface in this sample. Figure 84 illustrates the appearance of the fracture surface in the high strain to fracture sample. Note the distortion and bending of the ferrite pools in the weld-metal at and just behind the fracture surface, which is evidence of an strong instability having caused localization of plastic flow prior to fracture. Extensive secondary cracking was seen throughout the interior of the specimen and all along the exterior surface of the gage-length (Figure 85). In Figure 86 and 87 are shown the details of the secondary crack depicted in Figure 85. Note the propagation of the crack along pools of interdendritic ferrite and the formation of pores within the ferrite ahead of and alongside the growing crack. Figure 87 shows clearly the extensive localization of plastic-flow in the adjacent austenite associated with propagation of the crack.

Microstructures of typical weld-joint samples after torsion-testing at various temperatures and strain-rates are presented in Figures 88 through 98. In Figures 88 through 90 are presented microstructural

features of a sample, which when tested at a temperature: strain-rate combination of 75°F (24°C): 4.80 per minute, showed the only clear evidence of all weld-joint samples of instability formation in the heat-affected zone. Note that the fracture-path is partially through the sensitized heat-affected zone (Figure 88) and partially through the fusion-zone (Figure 89), and does not show much secondary cracking. In Figure 90 is presented the details of a crack emanating from a microshrinkage cavity in the fusion-zone. Note the pore-formation in ferrite pools throughout the region of the fusion-zone near the microshrinkage cavity and associated crack.

In Figures 91 and 92 are presented microstructural details of a weld-joint sample that was tested at a temperature: strain-rate combination of 500°F (250°C): 0.0690 per minute. This sample exhibited moderate secondary cracking throughout the heat-affected zone and fusion zone, with failure occurring entirely within the fusion-zone. Note the formation of pores within the ferrite pools and the growth of these pores into small cracks entirely within the ferrite (Figure 92), as well as the formation of inclusion: matrix decohesions within the austenite. Figure 91 shows the development of secondary cracks from the fracture surface and the localization of plastic flow around these microcracks.

Figures 93 and 94 summarize the pertinent microstructural features of a weld-joint sample that was tested at a temperature: strain-rate combination of 1000°F (538°C): 4.87 per minute. Note the extensive secondary cracking, both at the fracture surface and behind it (Figure 93). Propagation of a secondary crack just behind the fracture appears to have occurred by localization of plastic flow in the austenitic matrix leading

to tearing between microcracks that developed within ferrite pools (Figure 94). Failure was entirely within the fusion-zone.

Figures 95 through 99 presents microstructural features of a weld-joint sample that was tested at a temperature: strain-rate combination of 1200°F (649°C): 4.86 per minute. Failure occurred entirely within the fusion-zone, which shows evidence of extensive secondary crack-development (Figure 95). Note the branching of one of these secondary cracks (Figure 95). At and near the fracture surface (Figure 95), is evidence of intense localization of plastic flow, in the form of bending of inter-dendritic ferrite pools, that occurred during deformation of the strong instability associated with fracture. Figures 97 and 98 are enlargements of the growing end of the secondary crack shown in Figure 95. Note propagation of the crack through the austenite from one ferrite pool to another, and along an inclusion: austenite interface, as well as evidence of localization of plastic flow on the austenitic matrix ahead of the growing crack-tip (Figure 98).

DISCUSSION

1. Identification of Mode of Fracture

Irrespective of the level of ductility at fracture, as typified by strain to fracture values, the mechanism of fracture-initiation in wrought type 304 austentic stainless steel, either solution-annealed or sensitized, was the ductile fracture mechanism as described in the "Review of Previous Work". Evidence for this statement was gathered by careful optical-microscopic examination of failed samples. Since all fractures were driven by continued plastic straining, they occurred by the stable mode. Values of shear strain reported herein are a measure of the material's ability to accomodate plastic-strain in the presence of a notch, often referred to as the notch-ductility. These values do not usually correlate with values of ductility-parameters measured in the smooth-bar tension test.

Compare the microstructure of two solution-annealed samples; A4 (500°F (260°C): 0.62 per minute) that exhibited the maximum value of strain to fracture of 6.76, and sample A11 (1000°F (538°C): 4.72 per minute) that exhibited a relatively low value of strain to fracture of 2.42, as presented in Figures 50 to 51 and 54 to 58, respectively. Both samples show evidence of initiation of fracture by decohesion at randomly dispersed oxide and carbo-nitride inclusion: matrix interfaces, and propagation of cracks by localization of plastic-flow on a microscopic level.

Similar microstructural effects were seen in the case of sensitized material, as shown by comparing the microstructures of sample AS3 (500°F (260°C): 2.64 per minute) that recorded the maximum value of strain to fracture of 5.78 and sample AS15 (1200°F (649°C): 0.0731 per minute) that had the minimum value of strain to fracture of 1.42 as presented in Figures 70 to 71 and 74 to 76, respectively. In addition to oxide and carbo-nitride inclusion: matrix interfaces serving as sites for crack-initiation as was seen for the solution-annealed material, the interfaces created between the austenitic matrix and the $(Fe, Cr)_{23}C_6$ carbides that precipitated on grain boundaries and twin boundaries (Figures 64 and 65) could be expected to serve as potential sites for second phase: matrix decohesions to form. That these regions did serve as preferred locations for crack-initiation is shown for sensitized samples tested at ambient (AS17, 75°F (24°C): 2.34 per minute) and elevated temperatures (AS11, 500°F (260°C): 0.065 per minute, Figures 64 to 65 and 69). Previous evidence of the role of twin boundaries as crack-initiation sites in type 304 stainless steel deformed at elevated temperatures has been reported by Michel, Nahm, and Moteff (73). Despite the many additional inclusion (or second phase): matrix interfaces in the sensitized material, relative to the solution-annealed material, the range of strain to fracture values for the two material-conditions was from 1.42 to 5.78 for the sensitized material and from 1.23 to 6.76 for the solution-annealed material. Hence, sensitization appears to have only a slight effect on reducing the range of strain to fracture values seen in this investigation.

Similar to the trend set in the wrought material, as typified by strain to fracture values, the mode of fracture-initiation in welded type

304 austenitic stainless steel was by the ductile fracture mechanism. Consider the microstructure of two all weld-metal samples; that of sample W12 (75°F (24°C): 0.0688 per minute) that had a relatively-low strain to fracture value of 1.11 (Figures 77 and 78), and that of sample W9 (1200°F (649°C): 0.0720 per minute) that had a relatively high strain to fracture value of 1.78 (Figures 84-87). Irrespective of the relative strain to fracture values, fracture-initiation involved the formation of decohesions at two different types of sites. The more prevalent site was associated with the pools of delta-ferrite contained in a predominantly austenitic matrix. Pores tended to nucleate at the interfaces between delta-ferrite and the austenitic matrix, and enlarge either within the ferrite or within the austenite. This trend was seen not only in the above-mentioned specimens, but in specimens deformed over the entire range of temperatures and strain-rates employed. Additional examples are shown on Figures 80, 92 and 97. The less prevalent fracture-initiation site was associated with decohesions formed at an occasional non-metallic inclusion-matrix interface (Figures 91 and 92) similar in nature to one of the sources of fracture-initiation seen in wrought material.

Deciding on the mode of fracture propagation requires consideration of not only the metallographic evidence but also the types of instabilities observed during torsion-testing. For the moment; divide the specimens into two classes, using as a basis for the separation the presence or absence of instabilities visible with the naked eye during torsion testing, hereafter referred to as "macroscopic instabilities." Tables 2 through 5, which summarize the details of all torsion-tests performed, indicate that specimens tested under the following temperature:

nominal strain rate conditions failed without the occurrence of macroscopic instabilities being generated during torsion-testing: solution-annealed bar; 75°F (24°C), 500°F (260°C), and 1000°F (538°C) at a nominal strain-rate of 0.07 per minute; and sensitized bar; 75°F (24°C) and 500°F (260°C) at a nominal strain-rate of 0.07 per minute. All welded samples showed evidence of one or more macroscopic instabilities prior to failure. These conditions are summarized in Table 6.

Since a few samples failed without the development of macroscopic instabilities, i.e. underwent uniform deformation up to the instant of failure, let us consider the resulting microstructural changes. The microstructure of sample A4 (500°F (260°C): 0.0634 per minute) was typical of solution-annealed samples which underwent only uniform-deformation prior to failure. Figure 50 shows no evidence of microscopic instability formation on a scale equal to or larger than the dispersed inclusions at or near the fracture surface. Growth of secondary cracks behind the fracture-surface appeared to have occurred by tearing the material between decohesions formed at non-metallic inclusion: matrix interfaces (Figure 51), implying that localization of plastic flow took place on a scale smaller than the non-metallic inclusions. The microstructure of sample AS11 (500°F (260°C): 0.065 per minute) was typical of sensitized samples which underwent only uniform-deformation prior to failure. Figure 66 shows no evidence of instability formation on a scale larger than the particle-size of the grain-boundary carbides, while Figure 67 shows evidence of secondary crack-propagation occurring along grain-boundary carbide networks. An enlargement of the fracture surface and the region immediately behind it, shown in Figure 69, showed evidence of propagation

of cracks along a grain-boundary by localization of plastic flow between carbide particles on a scale equal to or less than the size of the intergranular carbides. Propagation of cracks in sensitized type 316 stainless steel deformed in static tension on a scale smaller than the carbide particles has been reported by Barnby (34). Evidently, specimens which deformed to fracture without the formation of macroscopic instabilities failed by what McGarry (74) described as a "mixed mode" fracture; i.e., one in which uniform deformation led to formation of pores at interfaces between second phase particles and the austenitic matrix, but where coalescence of pores occurred by means of microscopic instability-formation.

Most of the samples developed one or more instability-bands which are, to use the terminology of Ernst and Spretnak (64), "regions of concentrated shear-strain between slowly advancing interfaces on planes of pure shear". These bands appeared to be about 1/4 inch wide, formed at the moving end of the sample, and traversed the gage-length towards the stationary end of the sample at a speed of about 0.5 inch per second. Occasionally more than one instability band was moving along the gage-length at the same time, but never was one instability-band seen to overtake another or reverse directions in its travel along the gage-length. No evidence of diffuse flow, which was defined by Ernst and Spretnak (64) as being "characterized by a regional shear-gradient over a significant portion of the gage-length," was exhibited by any specimen. Microhardness values taken both near the fracture surface, in the strong instability associated with the fracture, and near the undeformed shoulder of the sample, which appeared to have undergone only uniform plastic-flow, are

summarized in Figure 99, and indicate that: (1) material within instability bands underwent a greater degree of work-hardening that adjacent material which appeared to have undergone only uniform plastic strain; and (2) localized plastic flow is not just a surface phenomenon, but extends through the entire cross-section of the bar, as indicated by the increase in centerline hardness within an instability band relative to centerline hardness values in portions of the specimen outside the instability band. Similar observations have been reported by Meyerer (75) for heat-treated AISI 4340 steel.

Examination of microstructures of samples which exhibited one or more macroscopic instabilities prior to fracture indicate that, while some evidence of crack-initiation by second phase: matrix decohesions existed in regions of the samples far from the strong-instability that led to fracture (Figures 45, 55, 76), a much greater incidence of secondary cracking, defined as cracks that are not associated with the final fracture, was seen in regions of the samples close to the fracture surface and associated instability. Compare Figures 59 with 60 and 74 with 76. These observations indicate that, at first, crack-initiation occurs as a result of matrix: second phase decohesions caused by uniform deformation. Once localization of plastic flow occurs in the form of macroscopic instability bands that are wide compared to the size of the second-phase particles, additional decohesions or pore-formation, takes place within the region undergoing intense localized plastic flow, as has been suggested by Spretnak (18). Propagation of cracks in solution-annealed type 304 stainless steel bar occurred in a transgranular mode, after the fibre axis had been rotated approximately 90 degrees from its

initial orientation parallel to the bar-axis to an orientation approximately parallel to the planes of maximum shear-strain along which macroscopic instabilities were seen to form and move during torsion-testing. On the microscopic level, propagation of cracks appeared to be associated with very narrow regions of highly-localized plastic flow, whose widths appeared to be greater than the size of the non-metallic inclusions associated with crack-initiation. Use of Nomarski differential interference contrast during metallographic examination indicated that these regions of highly-localized plastic flow were several grains wide, and existed on both sides of as well as ahead of the cracks. The best examples of this behavior are seen in welded samples in Figures 87 and 98. The orientation of these microscopic regions of highly localized plastic flow also tended to be at approximately 90° to the original bar axis, i.e., parallel to planes of maximum shear-strain (Figures 59, 62, 77, 84).

Propagation of cracks in sensitized type 304 stainless steel bar occurred mainly by intergranular cracks that appeared to grow along interfaces between grain-boundary precipitates of $(Fe,Cr)_{23}C_6$ carbides and the austenitic matrix (Figures 64, 65, 67, 69, 71, 75). Orientation of the cracks seemed to be at approximately right angles to the original bar-axis i.e., parallel to planes of maximum shear-strain. Occasionally, cracks deviated from their intergranular paths to travel either towards decohesions formed at non-metallic inclusion: matrix-interfaces (Figure 64), or from a small crack formed at the interface between twin-boundary carbides and austenite towards a carbide-laden grain-boundary favorably oriented for crack-propagation (Figure 65).

Propagation of cracks in welded samples took place by growth of decohesions formed at delta ferrite: austenite interfaces and by extension of these cracks through the austenitic matrix accompanied by an intense localization of plastic flow on a scale larger that the pools of delta-ferrite. (Figures 87, 98). Similar crack-propagation behavior has been reported for duplex austenite: delta-ferrite weldments deposited on types 304 and 316 base metals by a variety of processes by Shahinian, Smith, and Hawthorne (70), James (71), and Goodwin, Cole, and Slaughter (72). The predominant direction of propagation was close to right angles to the bar centerline, along planes of maximum shear strain (Figures 77, 81, 84, 87, 90, 97, 98). The "intense localization of plastic flow" referred to above was seen to exist at the edges of the fracture surface of several samples (Figures 77, 84, 91, 93) and might be the thinner portion of the macroscopic instability-band associated with fracture.

In summation, crack-propagation in both conditions of wrought material, as well as the cast weld-metal, appears to have involved localization of plastic flow on planes of maximum shear-strain with the thickness of the planes being greater than the size of the dispersed second phase, be it one or more of the following; non-metallic inclusions, $(Fe,Cr)_{23}C_6$ carbides, or delta-ferrite. Although some pore-formation undoubtedly occurred under the action of uniform deformation, the existence of macroscopic instability bands, together with the metallographic observations of regions of intense plastic flow of widths greater than the dispersed second phase, confirms that the mode of fracture was instability controlled as described by McGarry (74). However, since these

fractures were driven by continued straining, achievement of the ideal plastic state ($\frac{d\sigma}{d\varepsilon} = 0$) was not attained.

2. Comments on Deformation of Welded Samples

The tendency for each grain in the aggregate of the coarse-grained weld-metal to stand out in relief soon after torsion-testing began created a system of mechanical notches on the surface of the sample akin to a roughly-knurled surface. Since Zilova, Demina, and Fridman (56) have shown that strain-to-fracture values increase with decreasing surface roughness, and that the strain to the onset of the first instability also increases with decreasing surface roughness (76), the lower values of both parameters exhibited by welded specimens relative to unwelded specimens might have been due, in part, to the mechanical notch-effect introduced by this deformation-induced surface-roughening. Also, Chakrabarti (77) found that the strain to the onset of the first instability decreased with increasing grain size. In addition to these effects, which are respectively mechanical and metallurgical in nature, inherent differences in the fine-grained wrought product and the coarse-grained cast weldment, due to such factors as relations between microsegregation and ability to undergo extensive uniform plastic deformation, would be expected to reduce the total ductility (strain to fracture).

Differences in detailed behavior of strain to fracture and to the onset of the first instability between all weld-metal samples and weld-joint samples are attributed to the difference in the components of the weldment present in the two types of specimen. In the former case, where the gage section is composed entirely of weld-metal, the response to torsional straining is that of a cast, coarse-grained, multi-phase alloy

containing austenite, delta-ferrite, and non-metallic inclusions. In the latter case, where the gage section is composed of the centrally-located weld metal, sandwiched between the wrought heat-affected zone with a variation in grain-size due to the variation in peak temperature during welding, and surrounded finally by the fine-grained wrought base metal, the response to torsional straining is expected to be complex, and reflect the relative abilities of these three radically-different microstructures to resist localization of plastic flow and fracture when subjected to the same degree of strain.

3. Dynamic Strain Aging

In the present investigation, evidence of dynamic strain-aging was seen in the wrought bar stock in both material-conditions but not at all in temperature: strain-rate combinations. The occurrence of serrated flow-curves (actually torque-twist records) is summarized in Table 7. Thus, the occurrence of dynamic strain-aging, as indicated by serrated flow curves, is confined to the slowest strain-rate (0.07 per minute) at temperatures of 500°F (260°C) and 1000°F (538°C), and all strain rates (0.07 per minute to 4.8 per minute) at 1200°F (649°C).

Evidence of dynamic strain-aging in the form of serrated torque-twist curve was seen in some weld-joint specimens, which contained heat-affected zone and base-metal as well as weld-metal, but was absent in the tests performed on all weld-metal samples (Table 7). Serrated torque-twist curves on tests run on weld-joint samples were seen for the slowest strain-rate (0.07 per minute) at temperatures of 500°F (260°C) and 1000°F (538°C), and all strain-rates (0.07 per minute to 4.8 per minute) at

1200°F (649°C). These conditions of occurrence exactly parallel the conditions for the occurrence of serrated torque-twist curves exhibited by solution-annealed bar-stock. Hence, it is concluded that the portion of the gage-length in weld-joint samples that is comprised of base metal was responsible for the serrated torque-twist curves. The weld-metal or heat-affected zone did not appear to contribute to the occurrence of serrated torque-twist curves.

The occurrence of negative strain-rate sensitivity, or the decrease in flow-stress with increasing strain-rate, was examined by plotting the flow-stress at 10% significant strain determined on base metal samples, calculated by a method outlined in Dieter (78), versus nominal shear-strain rate, as shown in Figure 100. Both material-conditions show some evidence of negative strain-rate sensitivity at all temperatures.

Barnby (29), in his investigation of dynamic strain-aging in Type 316 stainless steel, made use of a "work-hardening parameter", which he defined as the stress-increment between the initial yield stress and the flow-stress for a given amount of strain. To exclude the temperature variation of elastic-constants from the comparison of stress-levels at different temperatures, Barnby normalized this stress-increment with respect to Young's modulus at room-temperature. Plotting it versus increasing test temperature, he found it to increase rather than decrease as expected for pure metals, and concluded that this increase was additional evidence of dynamic strain-aging.

Barnby's definition of his "work-hardening parameter" was adopted to analysis of torque-twist curves by conversion of torque-twist plots to

plots of significant stress versus significant strain by the method described by Dieter (78), determination of flow-stresses at various increments of significant strain (10%, 15%, 25%, and 50%) from interpolations from the significant stress-significant strain plots, and replacement of Barnby's temperature normalization with a correction based on the shear modulus rather than Young's modulus. Because the initial yield stress in torsion is masked by movement of the elastic: plastic boundary inward from the surface of the bar as yielding progresses, the writer chose to define a modified "work-hardening parameter as the stress-increment between the flow-stress at an indicated amount of significant strain and the flow stress at 10% significant strain, normalized for temperature effects as modified above. Plots of this parameter, determined at significant strain-levels of 15%, 25%, and 50%, against temperature are presented in Figures 101 through 104 for nominal strain rates of 4.8, 2.5, 0.6, and 0.07 per minute, respectively. The solution-annealed material showed some evidence of dynamic strain-aging at 500°F (260°C) through 1000°F (538°C), with the greatest evidence seen at a strain-rate of 0.07 per minute. The sensitized material showed evidence of dynamic strain-aging at 1000°F-1200°F (538°C-649°C) for the three fastest strain-rates (4.8, 2.5, and 0.6 per minute). At a strain-rate of 0.07 per minute, the sensitized material showed evidence of dynamic strain-aging at 500°F-1200°F (260°C-649°C). In summation, it appears that dynamic strain-aging does occur in both solution annealed and sensitized Type 304 stainless steel. The most probably temperature-range of occurrence of 500°F-1200°F (260°C-649°C) for solution-annealed material, and 1000°F-1200°F (538°C-649°C) for sensitized material.

A simple kinetic relationship for the strain at the onset of serrations may be written (80-81),

$$\gamma_S = A \exp\left(\frac{Q}{RT}\right)$$

where γ_S is shear strain at the onset of serrated flow, A is a factor independent of γ_S and T, but dependent on strain-rate, Q is an energy, and R and T have their usual meanings.

Assuming such a relationship is true, then straight lines of constant slope should result from a plot of $\ln \gamma_S$ versus $\frac{1}{T}$ if the process causing the serrations is induced by strain. Figure 105 presents such graphs for the solution-annealed, sensitized, and weld-joint samples tested at a nominal strain-rate of 0.07 per minute. Note that, despite the change in slopes, the lines for the solution-annealed bar and weld-joint samples closely parallel each other, suggesting that the same process or processes may be responsible for causing the serrated torque-twist curves. The slopes of these lines suggest activation energies of about 7 Kcal per mole in the high temperature region and 1 Kcal per mole in the low-temperature region. Limited data for sensitized bar stock suggests an activation energy of about 13 Kcal per mole. The change in slopes of the curves for the solution-annealed bar and weld-joint samples suggests a change in the mechanism for serrations. Also, the pre-exponential factor, A, does not seem to be independent of strain and temperature. A difference in the form of the serrations in the two regions of temperature (500°F to 1000°F (260°C-538°C), 1000°F to 1200°F (538°C- 649°C)) could not be distinguished. Jenkins and Smith (82), in their studies of the causes of dynamic strain-aging in Type 330 stainless steel, found that

the activation energy for the onset of serrations in tensile-tests was about 32 Kcal per mole for solution-annealed material. They also found that a plot of the strain for the first serration versus reciprocal temperature, consisted of two straight line, similar to Figure 105. However, their activation-energies for the low-temperature and high temperature regions were considerably higher than those determined from the torsion specimens, being about 8.8 Kcal per mole and 20 to 30 Kcal per mole, respectively. Since the difference in activation-energies between Jenkins and Smiths' results and the present results do not differ by a constant amount throughout, the most that may be concluded from this analysis is that two separate processes may be responsible for a dynamic strain-aging response in type 304 stainless steel over the range of temperatures employed.

Chakrabarti (77) has correlated serrated torque-twist curves obtained with room-temperature torsion-tests of alpha and alpha-beta brasses with the development of weak instabilities, which manefested themselves as "fleeting illuminations of very thin bands of material...". No such correlation was seen for the austenitic stainless steel employed in this investigation, possibly because: (1) no weak or diffuse instabilities were observed; and (2) "fleeting illuminations" would be quite difficult to detect against the intense background radiation emmitted by the tungsten-filament quartz lamps used to heat the gage-length.

Possible causes for dynamic strain aging of type 304 stainless steel can be divided into two categories: (a) dislocation: precipitate interactions; and (b) dislocation: solute atom interactions. The first cause, dislocation: precipitate interactions, has been studied by Harding

and Honeycombe (82), who determined that the cause of serrated tensile stress-strain curves in types 321 (18% Cr-10% Ni-1% Ti-0.09% C) and 347 (18% Cr-10% Ni-1% Cb-0.07% C) stainless steels was the locking of dislocations by formation of fine precipitates of TiC and CbC, respectively, on the dislocations. Similar results were seen in a modified type 330 grade (15% Ni-35% Cr-1% Ti-0.11% C) and were attributed to TiC precipitation on, and locking of dislocations. Naybour (83), in his study of strain-aging of a type 347 stainless steel, found that a portion of the dynamic strain-aging effect was due to an Orowan-dispersion hardening interaction between dislocations and CbC precipitates that did not necessarily form directly on the dislocations. Barnby (79), in his study of dynamic strain-aging of a type 316 (17% Cr-11% Ni-2.5% Mo-0.05% C) stainless steel, identified the cause of his serrated flow-curves as the precipitation of $(Fe,Cr)_{23}C_6$ particles on dislocations during testing.

The second cause, dislocation-solute atom interactions, has been studied by Tamhankar, Plateau, and Crussard (84) on a 10% Cr-35% Ni-0.03% C austenitic alloy, who attributed serrations in their flow-curves to interaction of dislocations with solute atmospheres. No attempt was made to identify the nature of the solute-species. Recently, Marek and Hochman (85) studied the static strain-aging behavior of a type 316 stainless steel, and tentatively identified the cause of the increased flow-stress as involving the segregation of carbon atoms to dislocations. However, no mention was made of any attempts to rule out the existence of a fine precipitate by electron microscopic examination of aged samples. Naybour (83) identified the cause of strain-aging at low plastic strains (up to 1%) in a type 347 stainless steel as being the formation of

columbium atmospheres on dislocations prior to actual precipitation of CbC.

Extensive studies of dynamic strain-aging in austenites with and without chromium have been conducted by Rose and Glover (80) and Jenkins and Smith (81). The former group worked with iron-nickel and iron-nickel-carbon austenites, with the elimination of chromium being done to prevent precipitation of $(Fe,Cr)_{23}C_6$ carbides on dislocations during testing. They found that the serrations were produced by dislocation-locking associated with stress-induced ordering of carbon-vacancy pairs (Snoek effect). The latter group worked with type 330 stainless steel with and without carbon, as well as iron-nickel and iron-nickel-carbon alloys. Dynamic strain-aging was attributed to strong interactions between dislocations and solute atoms. Between 392°F (200°C) and 932°F (400°C), the defect interacting with dislocations was suggested to be a carbon-vacancy pair, similar to the observations of Rose and Glover (80). Above 932°F (400°C), the defect interacting with dislocations was thought to be chromium atom atmospheres.

In summation, type 304 stainless steel exhibited definite signs of dynamic strain-aging, in the form of serrated torque-twist curves, in the range of temperatures 500°F-1200°F (260°C-649°C) for solution annealed material and 1000°F-1200°F (538°C-649°C) for sensitized material. Observed as indirect evidence for the occurrence of this phenomenon was negative strain-rate sensitivity of the flow stress at 10% strain (Figure 100) and an increase in work-hardening with increasing temperature (Figures 101-104). A plot of the shear strain at the first serration against reciprocal temperature (Figure 105) indicated that dynamic strain aging

was probably caused by two different processes. Comparison of observations with previously-reported work on dynamic strain-aging in iron-base austenites led the writer to favor some form of solute-atom: dislocation interaction as the cause of the phenomenon. However, careful electron microscopy would be necessary to eliminate the existence of $(Fe,Cr)_{23}C_6$ or some other phase as a possible precipitate on dislocations as an alternative explanation.

APPLICATION TO DESIGN OF LIQUID METAL FAST BREEDER REACTOR

Two separate but related safety problem-areas, both of which involve impulsive or high strain-rate loading, are the response of the large containment vessel and top-cover during impact from within, and the behavior of the reactor-core components during conditions of rapid thermal variations and/or mechanical loading (10). Attempts to extrapolate the results of this investigation, with a maximum strain-rate of about 5 per minute, to conditions involving impulsive loading, with estimated strain-rates of 10^2-10^3 per minute (10), are risky, especially since the work of Steichen (11) on smooth tensile properties of types 304 and 316 stainless steel as a function of temperature [600°F to 1200°F (316°C to 871°C)] and strain rate (10^{-3} per minute to 10^4 per minute] indicates that at temperatures above about 1000°F (538°C) the properties of the materials become quite sensitive to strain-rate.

What is a more fruitful use of the results of this investigation is a consideration of the possible effects on mechanical integrity resulting from the interaction of irradiation-produced defects and mechanical strains. At temperatures of irradiation below 1030°F (554°C), which is 50% of the absolute melting temperature for type 304 stainless steel, the predominant effect of radiation is the production of point defects (interstitial atoms and vacant lattice sites), many point-defect clusters, and vacancy-rich cores in the center of displacement-cascades (86). Since the interstitials are very mobile and anneal out at temperatures

below about 35% of the absolute melting point, most of the effects on mechanical behavior are probably associated with vacancy-related defects. Microstructural observations on stainless steels (87-90) indicate that the passage of dislocations removes defect clusters, and that in irradiated material slip is limited to narrow channels of relatively soft material surrounded by large masses of irradiation-hardened material, resulting in sharp decreases in strain-hardening coefficient (91). These resulting low values of strain-hardening coefficient could be indicative of the impending achievment of the "ideal plastic state." If the ideal plastic state is attained, and if one or more of the narrow channels of relatively soft material were to be so oriented as to lie along a direction of maximum shear strain, microcracks initiated at inclusion: matrix interfaces as described in the "Discussion" could easily propagate by the formation of instabilities between them in a "mixed" mode failure (74). In addition, the much higher concentration of vacancies in irradiated materials, relative to unirradiated materials, might result in some vacancies diffusing to potential sinks, such as second phase: matrix interfaces or grain-boundaries, and participating in the formation of decohesions by one of the mechanisms described in the "Review of Previous Work". Since fracture-initiation in both type 304 wrought bar and as-cast weld metal was seen to involve the development of second phase: matrix decohesions, the possible interaction between high vacancy-concentrations due to low-temperature irradiation and the strain-induced decohesions are not to be dismissed.

At temperatures of irradiation above 1030°F (554°C), the predominant effect of irradiation is the precipitation of helium-filled bubbles

on discontinuities within the material, such as grain-boundaries, grain-boundary triple-points, and second-phase: austenite interfaces. These bubbles will act as pre-existing voids or decohesions, and as such fulfill two of the three necessary conditions for fracture involving instability-formation: a free-surface and a stress-gradient from the free-surface back into the austenite. Under conditions of low strain-rate loading, such as in long-time creep, failure might be expected to occur by localization of plastic flow on a microscopic scale and formation of microscopic instability bands between the pre-existing helium-filled voids. In the presence of mechanical strain concentrations, such as exist at the root of a notch, the combination of pre-existing irradiation-induced voids (or bubbles) and the localization of strain might result in the formation of a crack of sufficient length which, under the action of loads such as those introduced by the build-up of reaction stresses during welding, might be propagated by the release of elastic energy stored in the structure. Under conditions of high strain-rate loading, such as in impulsive loading due to impact of moving objects, the preferential precipitation of helium-filled voids at grain-boundary triple points once again provides innumerable pre-existing crack nuclei which grow by the localization of plastic flow in planes of maximum shear strain, i.e., by instability formation and propagation in the manner described in the "Discussion".

CONCLUSIONS

1. The mode of fracture-initiation in type 304 austenitic stainless steel bar stock involved the formation of pores by decohesions at second phase particle: matrix interfaces. In solution-annealed material, the second phase particles appeared to be randomly-dispersed non-metallic inclusions such as oxides and carbo-nitrides. In sensitized material, the second phase particles included randomly-dispersed non-metallic inclusions and an extensive $(Fe,Cr)_{23}C_6$ precipitate localized primarily at grain-boundaries and twin-boundaries. For weld-metal deposited by the manual metal arc process from E308-15 electrodes, the mode of fracture-initiation involved the formation of pores at delta ferrite: austenite interfaces and within the delta ferrite itself. Isolated examples of pore-formation by decohesion at non-metallic inclusion: interfaces were also seen.

2. Fracture-propagation in the majority of cases for wrought type 304 stainless steel bar and in all cases for weldments deposited on type 304 stainless steel plate involved a form of instability-controlled fracture, wherein localization of plastic-flow on planes of maximum shear-strain results in final separation taking place along one of these planes. In the few cases where macroscopic localization of plastic flow was not observed, fracture-propagation was by a "mixed-mode" mechanism, wherein coalescence of pores created at second-phase particle: austenite interfaces by uniform deformation took place by means of microscopically-thin

instability-bands that limited the amount of plastic flow required to join the pores. In all cases, propagation of the fracture required continued plastic straining. Hence, all fractures occurred by the stable mode.

3. Both solution annealed and sensitized type 304 bar stock showed trends of decreasing strain to fracture and strain to formation of first instability with temperature in the ranges of 500°F-1200°F (260°C-649°C). Values of shear strain to fracture and to the formation of first instability are measures of the material's ability to accomodate plastic-strain in the presence of a notch, often referred to as the notch-ductility. These values do not usually correlate with values of ductility-parameters measured in the smooth-bar tension-test.

4. Dynamic strain-aging was observed in both solution-annealed and sensitized type 304 stainless-steel bar stock, and probably involves the occurrence of two different mechanisms, one operative up to about 1000°F (538°C), the other from about 1000°F to 1200°F (538°C-649°C).

5. Any clear cut effect of stress gradient on deformation behavior of solution annealed Type 304 bar stock at 500°F (260°C) was masked by a strong strain rate dependence of fracture strain and strain to first instability.

6. Deformation of both all weld-metal samples, and weld-joint samples which spanned the entire weldment, appears to be controlled primarily by the extremely heterogeneous grain-to-grain plastic flow of the large grained fusion zones. In general, strains to fracture and to first instability did not exceed 50% of base metal values for temperatures up to and including 1000°F (538°C). At 1200°F (649°C) the values of these

parameters for welded samples ranged from 70% to 150% of base metal values. This variation raises the question of the weld-metal's reproducibility of response to load-temperature spectra within the anticipaged operating range of the LMFBR. On this basis, it is concluded that ductility limitations to the use of type 304 stainless steel in LMFBR applications will be confined to the weldments.

Consideration of possible interactions between irradiation-induced lattice-defects and voids and the modes of fracture initiation and propagation discussed above indicate that such interactions are expected to aggravate any present propensities towards fracture-propagation by instability-formation and growth.

REFERENCES

1. Spretnak, J. W., Proceedings of the First International Conference on Structural Mechanics in Reactor Technology, Berlin, September 20-24, 1971.
2. Chakrabarti, A. K., Characteristics of Plastic Instability in the Direction of Pure Shear, Dissertation, Department of Metallurgical Engineering, The Ohio State University, 1973.
3. McGarry, D. L., The Effect of Strength Level and Strain Rate on the Mode of Fracture Initiation in AISI 4340 Steel, Master's Thesis, Department of Metallurgical Engineering, The Ohio State University, 1972.
4. Dieter, G. E., Mechanical Metallurgy, McGraw Hill, New York, 1961, p. 190.
5. McLean, D., Mechanical Properties of Metals, Wiley, New York, 1962, p. 240.
6. Van Iterson, F. K. T., Plasticity in Engineering, Blackie and Son, Ltd., London and Glasgow, 1947.
7. Meyerer, W. J., and Spretnak, J. W., USAEC Report No. COO-2048-3, The Ohio State University Research Foundation, July 1971.
8. Bauer, A. A., and Connor, J. G., A Survey of LMFBR Component Materials Limitations and Requirements, Battelle Memorial Institute, BMI-1901, January 1970.

9. Van Echo, A., U. S. Atomic Energy Commission, Division of Reactor Development and Technology, personal communication, September 1971.

10. Hoagland, R. G., Effect of Strain-Rate on Mechanical Properties of Austenitic Stainless Steels, Battelle Memorial Institute, BNWL-1105, September 1969.

11. Steichen, J. M., High Strain-Rate Mechanical Properties of Types 304 and 316 Stainless Steels, Hanford Engineering Development Laboratory HEDL-TME 71-164, November 1971.

12. McLean, D., Mechanical Properties of Metals, Wiley, New York, 1962, p. 224.

13. Low, J. R., Engineering Fracture Mechanics, 1, 1968, p. 47.

14. Rosenfield, A. R., Criteria for Ductile Fracture of Two Phase Alloys, Metals and Materials and Metallurgical Reviews, No. 121, April 1968, p. 29.

15. Broek, D., A Study on Ductile Fracture, Dissertation, Technical University of Delft (Netherlands), February 1971, pp. 30-46.

16. Van Iterson, F. K. Th., Plasticity in Engineering, Blackie and Son Limited, 1947.

17. Spretnak, J. W., Proceedings of the International Conference on the Strength of Metals and Alloys, Supplement to the Transactions of the Japanese Institute of Metals, 9, 1968, pp. 305-312.

18. Spretnak, J. W., Transactions of the Metallurgical Society of AIME, 236, (11), November 1969, p. 1639.

19. Ludwik, P., Zeitschrift für Metallkunde, 18, 1926, p. 269.

20. Puttick, K. E., Philosophical Magazine, 4, 1959, p. 964.

21. Rogers, H. C., Transactions of the Metallurgical Society of AIME, 218, 1960, p. 498.

22. Beachem, C. D., Transactions of the American Society for Metals, 56, 1963, p. 318.

23. Goodier, J. N., Journal of Applied Mechanics, 1, (2), 1933, p. 39-44.

24. Gurland, J., and Plateau, J., Transactions of the American Society for Metals, 56, 1963, pp. 442-454.

25. Ashby, M. F., Philosophical Magazine, 14, 1966, pp. 1157-1178.

26. Tipnis, V. A., and Cook, N. H., Journal of Basic Engineering of ASME, 92, (3), 1967, pp. 533-540.

27. Brower, W. E., Jr., and Flemings, M. C., Solidification-Structure-Fracture-Relationship in Inclusion-Bearing Iron, Dissertation, Department of Metallurgy and Materials Science, Massachusetts Institute of Technology, 1969.

28. Broek, D., A Study on Ductile Fracture, Dissertation, Technical University of Delft (Netherlands), February 1971, p. 25.

29. Baker, T. J., and Charles, J. A., Journal of the Iron and Steel Institute, 210, (9), 1972, pp. 680-690.

30. Pickering, F. B., Journal of the Iron and Steel Institute, 189, 1958, p. 148.

31. Rudnik, S., Journal of the Iron and Steel Institute, 204, 1966, p. 374.

32. Charles, J. A., and Uchiyama, I., Journal of the Iron and Steel Institute, 207, 1969, p. 979.

33. Gurland, J., Transactions of the Metallurgical Society of AIME, 227, (10), 1963, pp. 1146-1150.

34. Barnby, J. T., Acta Metallurgica, 15(5), May 1967, p. 903.

35. Shapiro, E., and Dieter, G. E., Metallurgical Transactions, 1, (6), 1970, pp. 1711-1219.

36. Driver, J. W., Metal Science Journal, 6, 1971, pp. 47-50.

37. Palmer, G., and Smith, G. C., Bases of Yield and Fracture, Physics Society Conference Series, 1, Oxford, 1966, pp. 53-59.

38. Olsen, R. J., American Society for Metals Transactions Quarterly, 62, 1969, pp. 711-719.

39. Ruedl, E., Journal of Materials Science, 4, 1969, pp. 814-815.

40. Barnby, J. T., and Peace, F. M., Acta Metallurgica, 19, (12), 1971, pp. 1351-1358.

41. Thomason, P. F., Journal of the Institute of Metals, 96, 1968, pp. 360-365.

42. Thomason, P. F., Metal Science Journal, 5, 1971, pp. 64-67.

43. McClintock, F. A., Koplan, S. M., and Berg, C. A., Jr., International Journal of Fracture Mechanics, 2, 1966, pp. 614-627.

44. Broek, D., A Study on Ductile Fracture, Dissertation, Technical University of Delft (Netherlands), February 1971, pp. 53-56.

45. Hirsch, P. B., Journal of the Institute of Metals, 86, 1957, pp. 13-14.

46. Ashby, M. F., Zeitschrift fur Metallkunde, 55, 1964, pp. 5-17.

47. Friedel, J., Dislocations, Pergamon-Adison Wesley, New York, 1964.

48. Bowden, P. B., Philosophical Magazine, 22, 1970, p. 455.

49. Williams, D. C., Gray Iron News, February 1962, p. 7.

50. Blum, J. I., and Morressey, R. J., Proceedings of the First International Conference on Fracture, Sandai (Japan), 1966, p. 1739.

51. Beavers, C. J., and Honeycombe, R. W. K., Philosophical Magazine, 7, 1962, p. 763.

52. Hayden, H. W., and Floreen, S., Acta Metallurgica, 17, 1969, p. 213.

53. Rybalko, F. R., Doklady Akademii Nauk, 93, (3), 1953, pp. 471-473.

54. Rybalko, F. R., and Yakutovich, M. V., Physics of Metals and Metallography, 1, 1955, pp. 231-238.

55. Rybalko, F. R., and Yakutovich, M. V., Physics of Metals and Metallography, 4, 1957, p. 450.

56. Zilova, T. K., Demina, N. I., and Fridman, Ya. B., Physics of Metals and Metallography, 4, 1957, p. 455.

57. Mostovoy, S., and Polakowski, N., Transactions of the American Society for Metals, 54, 1961, pp. 567-579.

58. Troiano, A. R., and Kochera, J. W., AFML TR-67-82, Case Institute of Technology, March 1967.

59. McGarry, D. L., The Influence of Strength Level and Strain Rate on the Mode of Fracture Initiation in AISI 4340 Steel, Master's Thesis, Department of Metallurgical Engineering, The Ohio State University, 1972.

60. Griffis, C. A., and Spretnak, J. W., Metallurgical Transactions, 1 (2), 1970, p. 550.

61. Chang, L. C., Journal of the Mechanics and Physics of Solids, 3, 1955, p. 212.

62. Fields, D. S., and Backofen, W. A., Proceedings of the American Society for Testing and Materials, 57, 1957, pp. 1259-1271.

63. Griffis, C. A., and Spretnak, J. W., Transactions of the Iron and Steel Institute of Japan, 9, 1969, pp. 372-387.

64. Ernst, R. H., and Spretnak, J. W., Transactions of the Iron and Steel Institute of Japan, 9, 1969, pp. 361-371.

65. Chakrabarti, A. K., The Effect of Degree of Saturation of Terminal Solid Solutions on Susceptibility to Plastic Instability in Pure Shear, Master's Thesis, Department of Metallurgical Engineering, The Ohio State University, 1971, pp. 66-68.

66. Vanecko, J. M., The Role of Plastic Instability in the Temperature Transition on Toughness of Rimmed Carbon Steel, Master's Thesis, Department of Metallurgical Engineering, The Ohio State University, 1970, pp. 62-64.

67. Stuwe, H. P., and Asbeck, H. O., Archiv für das Eisenhüttenwesen, 40, 1969, p. 124.

68. Meyerer, W. J., Effect of Shear Strain-Rate and Temperature on the Susceptibility of AISI 4340 Steel to Plastic Instability in Torsion, Master's Thesis, Department of Metallurgical Engineering, The Ohio State University, 1970, pp. 32-35.

69. Tanaka, K., and Spretnak, J. W., Metallurgical Transactions, 4 (2), 1973, pp. 443-454.

70. Shahinian, P., Smith, H. H., and Hawthorne, J. R., Welding Journal, 51 (11), November 1972, p. 527S.

71. James, L. A., Welding Journal, 52 (4), April 1973, p. 173S.

72. Goodwin, G., Cole, N., and Slaughter, G., Welding Journal, 51 (9), September 1972, p. 425S.

73. Michel, D. J., Nahm, H., and Moteff, J., Materials Science and Engineering, 11, 1973, pp. 97-102.

74. McGarry, D. L., The Influence of Strength-Level and Strain Rate on the Mode of Fracture Initiation in AISI 4340 Steel, Master's Thesis, Department of Metallurgical Engineering, The Ohio State University, 1972, p. 5.

75. Meyerer, W. L., Effect of Shear Strain Rate and Temperature on the Susceptibility of AISI 4340 Steel to Plastic Instability in Torsion, Master's Thesis, Department of Metallurgical Engineering, The Ohio State University, 1972, pp. 30-31.

76. McGarry, D. L., Private Communication.

77. Chakrabarti, A. K., The Effect of Degree of Saturation of Terminal Solid Solutions on Susceptibility to Plastic Instability in Pure Shear, Master's Thesis, Department of Metallurgical Engineering, The Ohio State University, p. 62.

78. Dieter, G. E., Mechanical Metallurgy, McGraw-Hill, New York, 1961, pp. 276-280.

79. Barnby, J. T., Journal of the Iron and Steel Institute, 203, 1965, pp. 392-397.

80. Rose, K. S. B., and Glover, S. G., Acta Metallurgica, 14, 1966, pp. 1505-1516.

81. Jenkins, C. F., and Smith, G. V., Transactions of the Metallurgical Society of AIME, 245, 1969, pp. 2149-2156.

82. Harding, H. J., and Honeycombe, R. W. K., Journal of the Iron and Steel Institute, 204, 1966, pp. 259-267.

83. Naybour, R. D., Acta Metallurgica, 13, 1965, pp. 1197-1207.

84. Tamhankar, R., Plateau, J., and Crussard, C., Revue de Metallurgie, 55, (4), 1958, pp. 383-400.

85. Marek, M., and Hochman, R., Scripta Metallurgica, 3, 1969, pp. 693-698.

86. Steigler, J. O., and Weir, J. R., Jr., "Effects of Irradiation on Ductility," Ductility, American Society for Metals, 1967, pp. 311-342.

87. Greenfield, I. G., and Wilsdorf, H. G. F., Journal of Applied Physics, 32, 1961, p. 827.

88. Mastel, B., Kissinger, H., Laidter, J. J., and Bierlein, T. K., Journal of Applied Physics, 34, 1963, p. 3637.

89. Brimhall, J., Transactions of the Metallurgical Society of AIME, 233, 1965, p. 1737.

90. Sharp, J. V., Philosophical Magazine, 16, 1967, p. 77.

91. Bloom, E. E., Martin, W. R., Stiegler, J. O,, and Weir, J. R., Jr., Journal of Nuclear Materials, 22, 1967, p. 68.

Table 1.

Summary of Selected Applications of Type 304 Stainless Steel in the Liquid Metal Fast Breeder Reactor (8)

Reactor Sub-System	Component	Product Forms	Probable Range of Temperatures	Special Environmental Requirements
Coolant transport sub system	Piping	Thin wall (3/8 inch) large diameter (28 in. outside diameter) seamless tubing	900-1200°F (482-649°C)	Liquid Na
	Valves	Forgings, castings, weldments	900-1200°F (482-649°C)	Liquid Na
Intermediate heat exchanger	Tubing	Thin wall large-diameter seamless tubing	970-1200°F (521-649°C)	Liquid Na
	Shell	Plate, weldments	900-1150°F (482-621°C)	Air
	Tube Sheet	Rolled plate	970-1200°F (521-649°C)	Inert Atmosphere
Control-rod drive and fuel-handling mechanism	Control-rod drive	Rod, tubing, weldments	Ambient to 1200°F (649°C)	Inert gas, high levels of irradiation
	Fuel-handling mechanism	Plate, seamless tubing, forgings, weldments	Ambient to 1200°F (649°C)	Inert gas, high levels of irradiation

Table 2.

Composition of Materials Used in This Investigation

Material Form	Composition, weight percent									
	C	N	Cr	Ni	Mn	Si	Cu	P	S	Mo
Type 304 Bar 1 inch diameter	0.069	0.020	18.38	9.18	1.78	0.45	--	0.027	0.030	--
Type 304 plate-- 2 inches thick	0.056	0.051	18.36	9.33	0.96	0.64	0.29	0.021	0.015	0.19
Type E308--15 welding electrode-1/4 inch diameter, all weld-metal deposit	0.060	0.041	19.50	9.48	1.77	0.46	0.11	0.043	0.007	0.20

Table 3.

Results of Torsion Tests of Type 304 Stainl

Specimen	Temperature	Shear Strain Rate	γ_i[a]	Γ_i	γ_M
[b]A19	75°F (24°C)	4.25 per min	0.238	270 in-lb	1.56
A20	75°F	2.36	1.75	480	1.48
A21	75°F	0.662	3.78	530	4.00
A22	75°F	0.0703	---	---	3.59
[c]AS16	75°F	5.00	1.59	455	1.66
AS17	75°F	2.34	2.05	477	1.49
AS18	75°F	0.670	1.08	470	4.24
AS20	75°F	0.0720	---	---	4.63
A23	400°F (204°C)	2.43	2.30	331	5.70
A13	500°F (260°C)	4.80	2.22	368	4.84
A3	500°F	2.58	2.23	330	6.73
A4	500°F	0.620	1.29	345	6.76
A14	500°F	0.0634	---	---	6.50
AS9	500°F	4.87	1.67	310	4.95
AS3	500°F	2.64	2.43	330	5.78
AS10	500°F	0.628	1.48	358	5.59
AS11	500°F	0.065	---	---	4.54

Table 3.

esults of Torsion Tests of Type 304 Stainless Steel Bar Stock

hear Strain Rate	γ_i[a]	Γ_i	γ_M	Γ_M	γ_F	Γ_F	$\gamma_F-\gamma_i$	$\frac{1}{\gamma_F-\gamma_i}$
.25 per min	0.238	270 in-lb	1.56	470 in-lb	3.59	450 in-lb	3.35	0.298
.36	1.75	480	1.48	480	3.45	460	1.70	0.589
.662	3.78	530	4.00	530	4.00	530	0.27	3.71
.0703	---	---	3.59	595	3.59	595	---	---
.00	1.59	455	1.66	460	3.61	435	2.01	0.499
.34	2.05	477	1.49	480	2.32	470	0.27	3.71
.670	1.08	470	4.24	510	4.24	510	3.16	0.371
.0720	---	---	4.63	590	4.63	590	---	---
.43	2.30	331	5.70	458	5.70	458	3.40	0.293
.80	2.22	368	4.84	423	5.33	405	3.11	0.321
2.58	2.23	330	6.73	406	6.73	406	4.50	0.222
.620	1.29	345	6.76	470	6.76	470	5.47	0.183
.0634	---	---	6.50	480	6.50	480	---	---
.87	1.67	310	4.95	358	5.20	348	3.53	0.282
2.64	2.43	330	5.78	387	5.78	387	3.35	0.299
.628	1.48	358	5.59	465	5.65	462	4.17	0.239
.065	---	---	4.54	488	4.56	485	---	---

Table 3. (Cont.)

Specimen	Temperature	Shear Strain Rate	γ_i	Γ_i	γ_M
A24	600°F (316°C)	2.42	2.18	306	5.04
A11	1000°F (538°C)	4.72	1.15	247	1.73
A7	1000°F	2.49	1.48	310	2.11
A8	1000°F	2.48	1.26	320	1.91
A9	1000°F	0.630	1.63	318	3.47
A10	1000°F	0.070	---	---	2.62
AS8	1000°F	4.81	0.832	274	1.34
AS5	1000°F	2.35	1.27	328	2.74
AS6	1000°F	0.570	1.52	311	4.38
AS7	1000°F	0.083	2.03	330	3.30
A15	1200°F (649°C)	4.79	0.842	252	1.09
A16	1200°F	2.50	0.864	235	0.965
A17	1200°F	0.665	0.739	244	1.02
A18	1200°F	0.0730	0.519	241	0.519
AS12	1200°F	4.80	0.911	246	1.08
AS13	1200°F	2.54	0.892	257	1.00
AS14	1200°F	0.590	0.832	250	0.925
AS15	1200°F	0.0731	0.538	224	0.821

Table 3. (Cont.)

hear Strain Rate	γ_i	Γ_i	γ_M	Γ_M	γ_F	Γ_F	$\gamma_F-\gamma_i$	$\frac{1}{\gamma_F-\gamma}$
.42	2.18	306	5.04	398	5.70	380	3.52	0.28
.72	1.15	247	1.73	303	2.42	283	1.27	0.78
.49	1.48	310	2.11	316	2.82	305	1.34	0.74
.48	1.26	320	1.91	324	2.66	300	1.40	0.71
.630	1.63	318	3.47	338	3.47	338	1.84	0.54
.070	---	---	2.62	400	2.83	394	---	---
.81	0.832	274	1.34	290	2.57	275	1.74	0.57
.35	1.27	328	2.74	328	2.98	309	1.71	0.58
.570	1.52	311	4.38	337	4.38	337	2.86	0.34
.083	2.03	330	3.30	340	3.41	340	1.38	0.72
.79	0.842	252	1.09	259	1.52	245	0.678	1.47
.50	0.864	235	0.965	237	1.67	220	0.806	1.24
.665	0.739	244	1.02	248	1.98	246	1.241	0.80
.0730	0.519	241	0.519	241	1.23	235	0.711	1.41
.80	0.911	246	1.08	260	1.87	238	0.959	1.04
.54	0.892	257	1.00	260	1.67	248	0.778	1.29
.590	0.832	250	0.925	253	2.03	253	1.198	0.83
.0731	0.538	224	0.821	225	1.42	214	0.882	1.1

Table 3. (Cont.)

a γ_i--Shear strain at onset of instability; Γ_i--torque at γ_i; γ_M--she

γ_F--shear strain at fracture; Γ_F--torque at fracture.

b "A" specimens have been solution-annealed as follows: 2000°F (109

c "AS" specimens have been sensitized as follows: "A" treatment plus

--- No instabilities observed in this test.

Table 3. (Cont.) .

set of instability; Γ_i--torque at γ_i; γ_M--shear strain at maximum torque; Γ_M--maximum torque;
fracture; Γ_F--torque at fracture.

n solution-annealed as follows: 2000°F (1093°C)--10 minutes--water quenched.

en sensitized as follows: "A" treatment plus 1200°F (649°C)--24 hours--water quenched.

ved in this test.

Table 4.

Results of Torsion Tests Conducted at 500°F (2
Bar Specimens of Various Diameter

Specimen	Bar Diameter	Shear Strain Rate	γ_i[a]	Γ_i	γ_M	
A27	0.2491 in	4.67 per min	1.23	208 lb-in	5.71	26
A26	0.2492	2.72	1.66	218	6.00	27
A28	0.2464	0.642	1.56	211	5.03	26
A29	0.2425	0.063	---	---	5.40	27
A30	0.1982	4.76	0.810	100	5.70	18
A31	0.1987	2.59	0.571	104	5.88	13
A32	0.1980	0.618	1.39	109	5.11	14
A33	0.1827	0.064	---	---	4.85	11

a γ_i--Shear strain at onset of instability; Γ_i--torque at γ_i; γ_M--shear st
γ_F--shear strain at fracture, Γ_F--torque at fracture.

Table 4.

Results of Torsion Tests Conducted at 500°F (260°C) on Type 304 Bar Specimens of Various Diameters

Shear Strain Rate	γ_i[a]	Γ_i	γ_M	Γ_M	γ_F	Γ_F	$\gamma_F-\gamma_i$	$\frac{1}{\gamma_F-}$
4.67 per min	1.23	208 lb-in	5.71	265 lb-in	6.26	249 lb-in	5.03	0.1
2.72	1.66	218	6.00	274	6.58	273	4.92	0.2
0.642	1.56	211	5.03	269	5.03	269	3.47	0.2
0.063	---	---	5.40	270	5.40	270	---	--
4.76	0.810	100	5.70	187	6.60	185	5.79	0.1
2.59	0.571	104	5.88	135	6.03	133	5.46	0.1
0.618	1.39	109	5.11	140	5.22	136	3.83	0.2
0.064	---	---	4.85	110	5.02	109	---	--

t of instability; Γ_i--torque at γ_i; γ_M--shear strain at maximum torque; Γ_M--maximum torque; racture, Γ_F--torque at fracture.

Table 5.

Results of Torsion Tests of Type 3

Specimen	Temperature	Shear Strain Rate	γ_i[a]	Γ_i	γ_M
[b]W10	75°F (24°C)	4.91 per min	0.241	337 lb-in	1.13
W11	75°F	0.642	0.098	318	1.12
W12	75°F	0.0688	0.062	286	1.08
[c]J10	75°F	4.80	0.302	365	1.07
J11	75°F	0.661	0.136	303	1.22
J12	75°F	0.0612	0.104	250	1.02
W1	500°F (260°C)	4.85	0.916	371	1.53
W2	500°F	0.584	0.251	312	1.24
W3	500°F	0.0651	0.090	268	1.16
J1	500°F	4.24	0.649	345	2.17
J2	500°F	0.648	0.222	280	1.9
J3	500°F	0.0690	0.113	233	2.0
W4	1000°F (538°C)	4.83	0.970	322	1.1
W5	1000°F	0.583	0.359	268	1.1
W6	1000°F	0.0721	0.151	252	1.0
J4	1000°F	4.87	1.54	289	3.6
J5	1000°F	0.587	0.296	253	1.1
J6	1000°F	0.0670	0.359	266	1.0

Table 5.

Results of Torsion Tests of Type 304 Welded Plate

ar Strain Rate	γ_i[a]	Γ_i	γ_M	Γ_M	γ_F	Γ_F	$\gamma_F - \gamma_i$	$\frac{1}{\gamma_F - \gamma_i}$
)1 per min	0.241	337 lb-in	1.13	502 lb-in	1.28	497 lb-in	1.039	0.964
342	0.098	318	1.12	542	1.16	535	1.062	0.940
)688	0.062	286	1.08	503	1.11	503	1.048	0.951
80	0.302	365	1.07	510	1.65	470	1.348	0.741
561	0.136	303	1.22	520	1.30	520	1.164	0.856
0612	0.104	250	1.02	434	1.02	434	0.916	1.09
85	0.916	371	1.53	387	1.53	307	0.614	1.63
584	0.251	312	1.24	383	1.24	383	0.989	1.01
.0651	0.090	268	1.16	392	1.16	392	1.070	0.932
.24	0.649	345	2.17	395	2.17	395	1.878	0.531
.648	0.222	280	1.95	392	1.95	392	1.728	0.580
.0690	0.113	233	2.04	394	2.04	394	1.927	0.519
.83	0.970	322	1.16	325	1.16	325	0.190	5.28
.583	0.359	268	1.11	328	1.16	318	0.803	1.24
.0721	0.151	252	1.01	328	1.01	328	0.859	1.16
.87	1.54	289	3.66	323	3.66	323	2.12	0.471
.587	0.296	253	1.14	317	1.17	317	0.874	1.14
.0670	0.359	266	1.06	311	1.06	311	0.701	1.43

Table 5. (Cont.)

Specimen	Temperature	Shear Strain Rate	γ_i	Γ_i	γ_M
W7	1200°F (649°C)	4.80	0.476	232	0.91
W8	1200°F	0.80	0.421	234	1.68
W9	1200°F	0.0720	0.280	232	0.95
J7	1200°F	4.86	0.325	221	0.96
J8	1200°F	0.630	0.266	216	0.92
J9	1200°F	0.0655	0.163	195	0.77

a γ_i--Shear strain at onset of instability; Γ_i--torque at γ_i; γ_M--she
γ_F--shear strain at fracture, Γ_F--torque at fracture.

b "W" specimens have a 1 inch long gage length centered completely wi

c "J" specimens have a 2.5 inch long gage length, centered on the wel
and base-metal.

Table 5. (Cont.)

ar Strain Rate	γ_i	Γ_i	γ_M	Γ_M	γ_F	Γ_F	$\gamma_F-\gamma_i$	$\frac{1}{\gamma_F-\gamma_i}$
10	0.476	232	0.915	251	1.50	248	1.024	0.970
10	0.421	234	1.68	251	1.96	248	1.539	0.650
1720	0.280	232	0.952	266	1.78	258	1.500	0.667
16	0.325	221	0.968	268	1.07	268	0.745	1.34
530	0.266	216	0.926	265	1.18	261	0.954	1.05
0655	0.163	195	0.772	241	1.05	237	0.887	1.13

F instability; Γ_i--torque at γ_i; γ_M--shear strain at maximum torque; Γ_M--maximum torque; ture, Γ_F--torque at fracture.

long gage length centered completely within the weld-metal.

ch long gage length, centered on the weld-metal, but also containing heat-affected zone

Table 6.

Summary of Temperature: Strain-Rate Conditions for Formation of Macroscopic Instabilities

Material Condition	Macroscopic Instabilities Seen at Strain-Rates Faster than those Indicated Below:			
	75°F (24°C)	500°F (260°C)	1000°F (538°C)	1200°F (649°C)
[a]Solution-annealed bar	.0.07 per min	0.07 per min	0.07 per min	All
[b]Sensitized bar	0.07	0.07	All	All
All Weld-metal	All	All	All	All
Weld joint	All	All	All	All

a Solution-annealed at 2000°F (1093°C) for 10 minutes and water-quenched.

b Solution-annealed plus 1200°F (649°C) for 24 hours and water-quenched.

Table 7.

Summary of Occurrence of Serrated Torque-Twist Records

Material Condition[a]	Nominal Strain Rate	Temperature 75°F	500°F	1000°F	1200°F
Solution-annealed	4.8 per min	No	No	No	Yes
	2.5	No	No	No	Yes
	0.6	No	No	No	Yes
	0.07	No	Yes	Yes	Yes
Sensitized	4.8	No	No	No	No
	2.5	No	No	No	Yes
	0.6	No	No	No	Yes
	0.07	No	No	Yes	Yes
All Weld-metal	4.8	No	No	No	No
	0.6	No	No	No	No
	0.07	No	No	No	No
Weld-joint	4.8	No	No	No	Yes
	0.6	No	No	No	Yes
	0.07	No	Yes	Yes	Yes

a Solution-annealed — 2000°F (1093°C)--10 minutes--H_2O quench.

Sensitized — Solution-anneal plus 1200°F (649°C)--24 hours--H_2O quench.

All weld-metal — Manual shielded metal-arc welded with E308-15 electrodes per Figure 13. Specimen configuration per Figure 15a.

Weld-joint — Manual shielded metal-arc welded with E308-15 electrodes per Figure 13. Specimen configuration per Figure 15b.

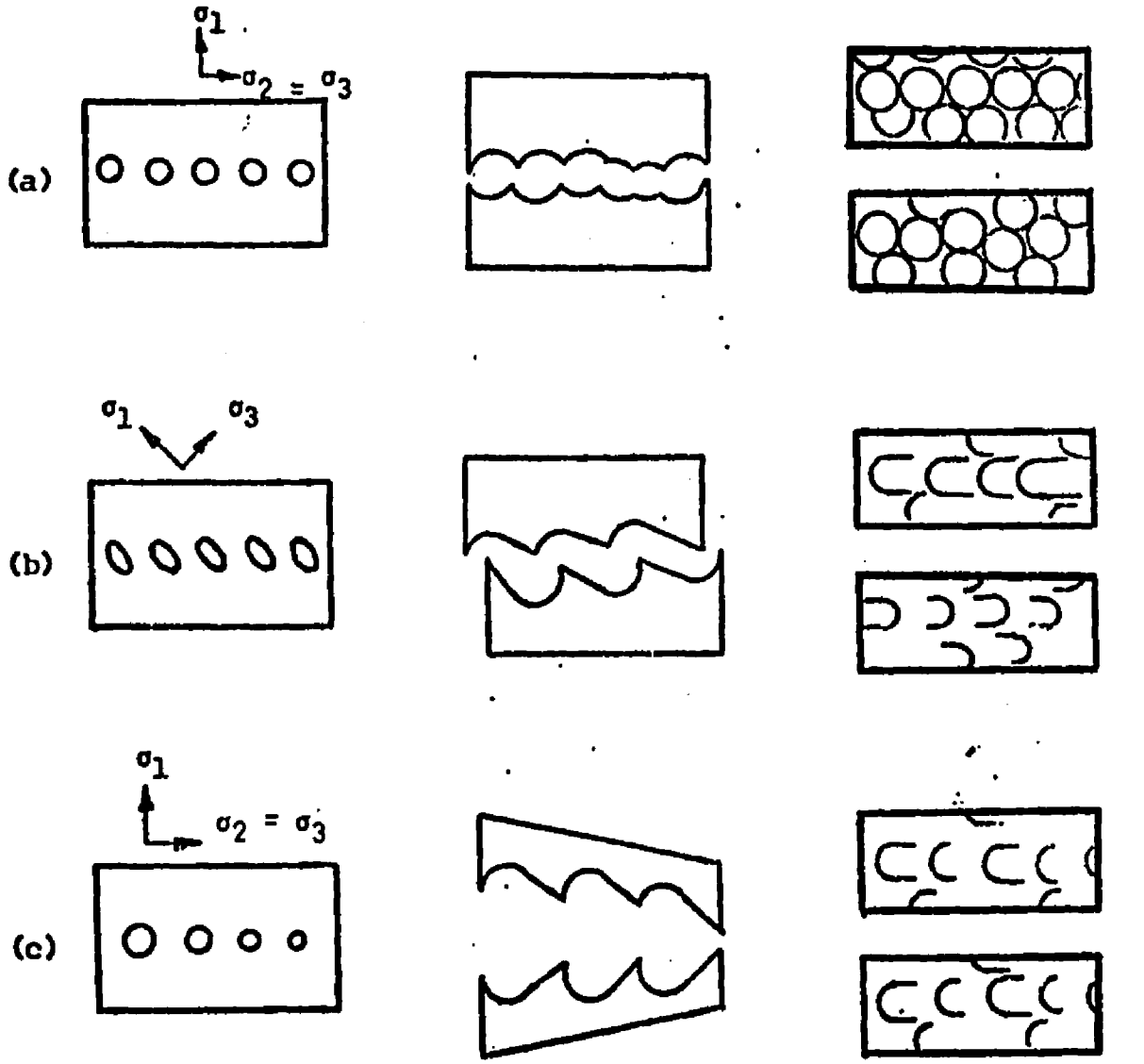

Figure 1. Schematic representation of three basic fracture surfaces in pore formation and coalescence fractures, after Beachem (22).

(a) Normal rupture, formation of equiaxed dimples; (b) shear rupture, formation of elongated dimples pointing in the direction of shear on each side of the plane of fracture; (c) tearing, formation of elongation dimples pointing away from propagation direction.

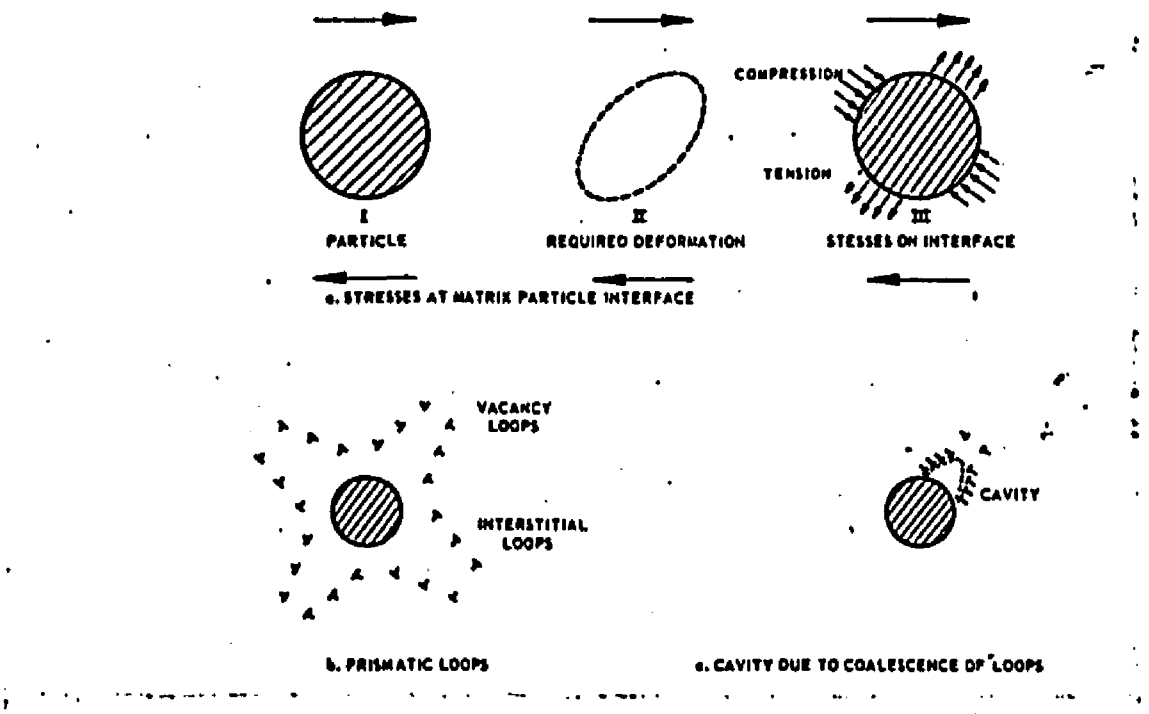

Figure 2. Ashby's model of cavity-initiation.

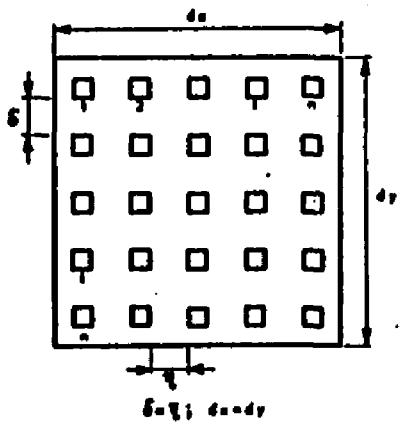

Figure 3. Prismatic voids in a sheet of unit thickness after Thomason (41).

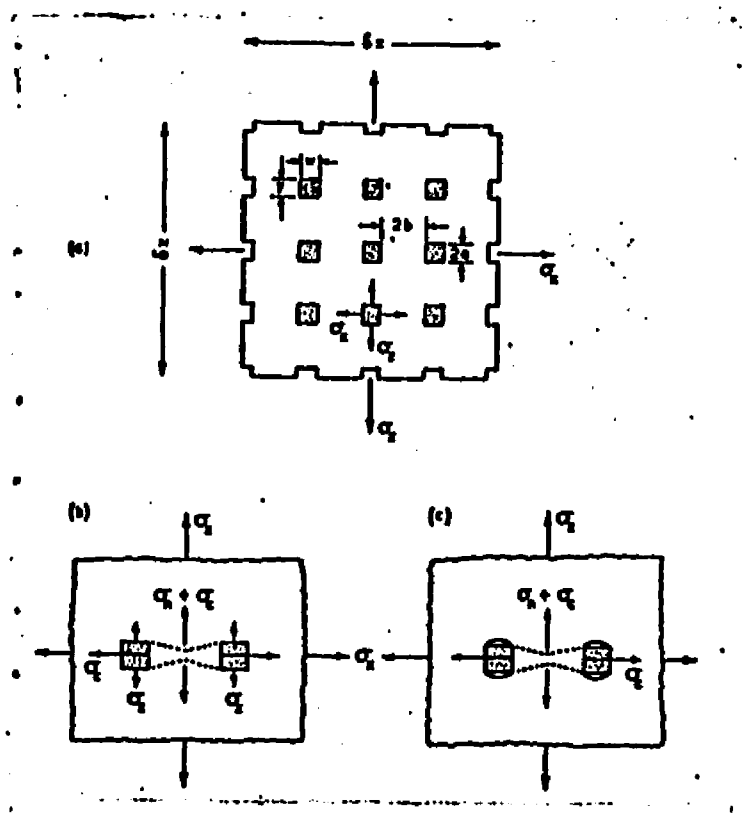

Figure 4. Rigid-plastic plane-strain element containing particles; (a) before tensile plastic instability, (b) at incipient instability without particle: matrix decohesion, (c) at incipient instability with decohesion at particle ends. (42)

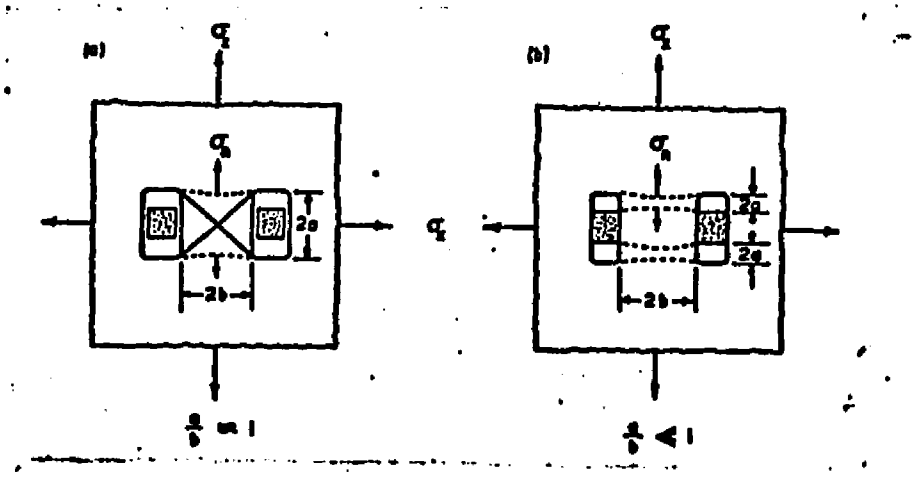

Figure 5. Illustration of situations leading to (a) low ductility when complete particle: matrix decohesion occurs; (b) increased ductility when the particle: matrix band remains intact at the sides of the particle. (42)

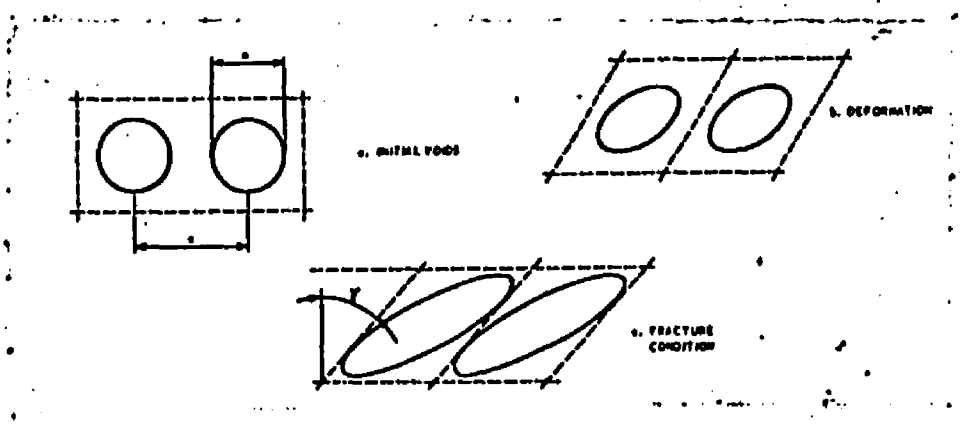

Figure 6. Cylindrical voids in the model of McClintock, Kaplan, and Berg (43).

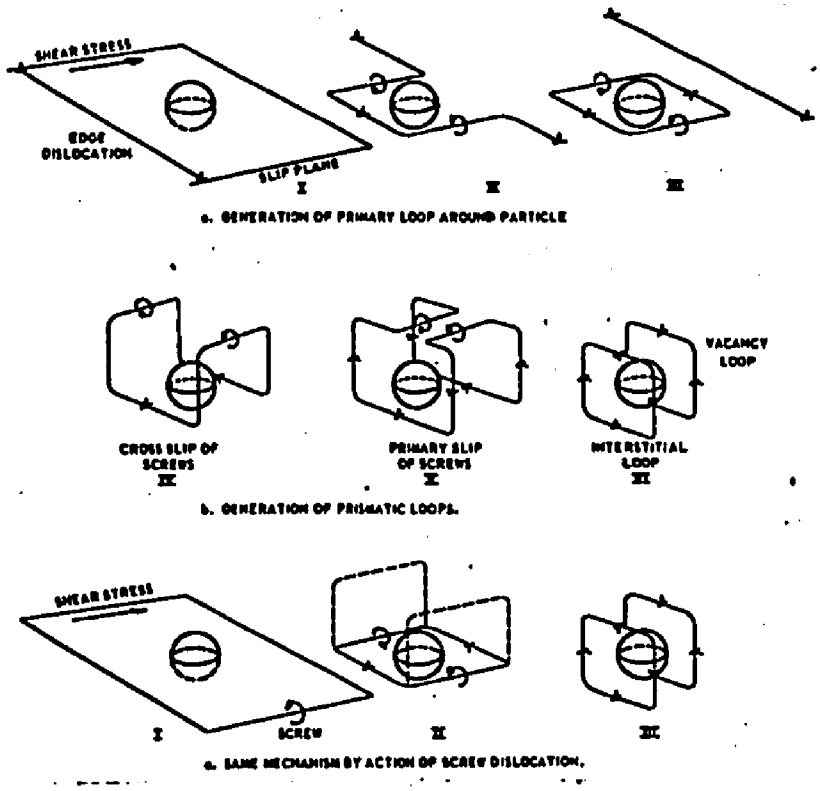

Figure 7. Generation of dislocation loops around particles by the mechanism of Hirsch (45) and Ashby (46).

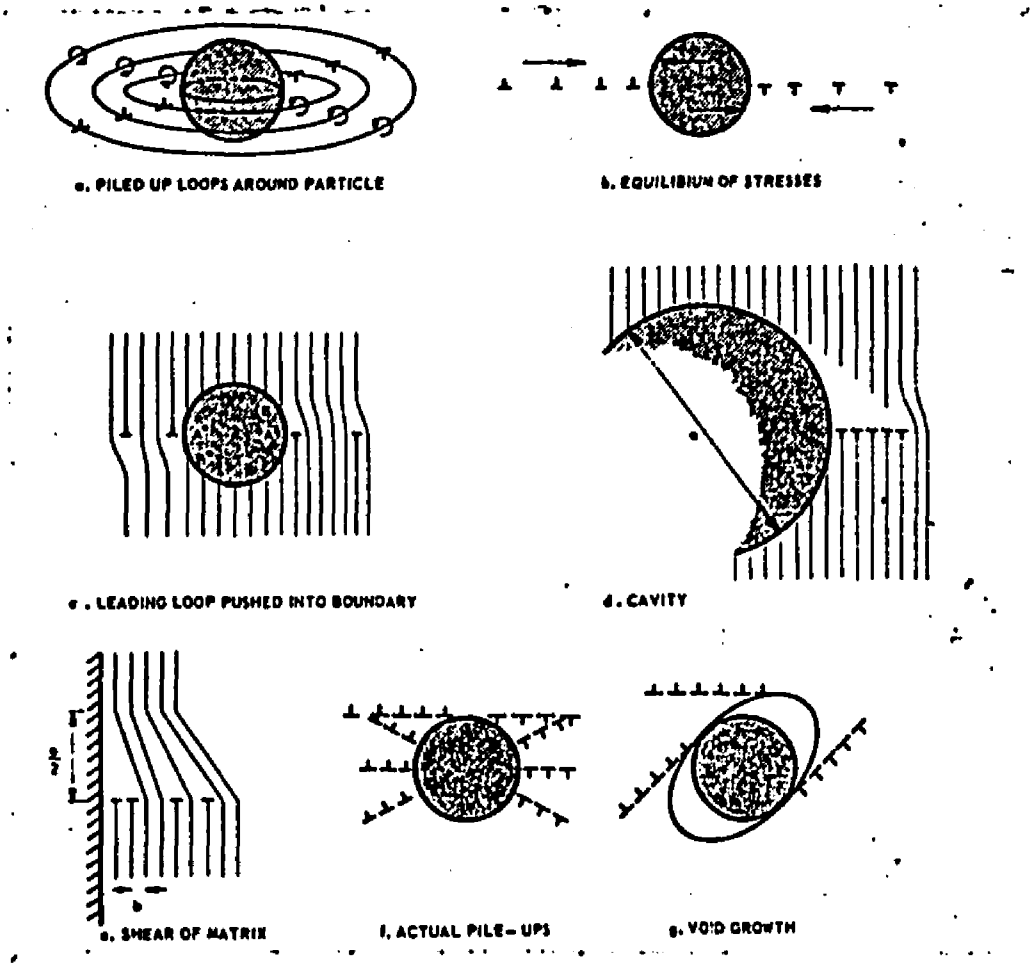

Figure 8 . Broek's (44) model of void initiation and growth.

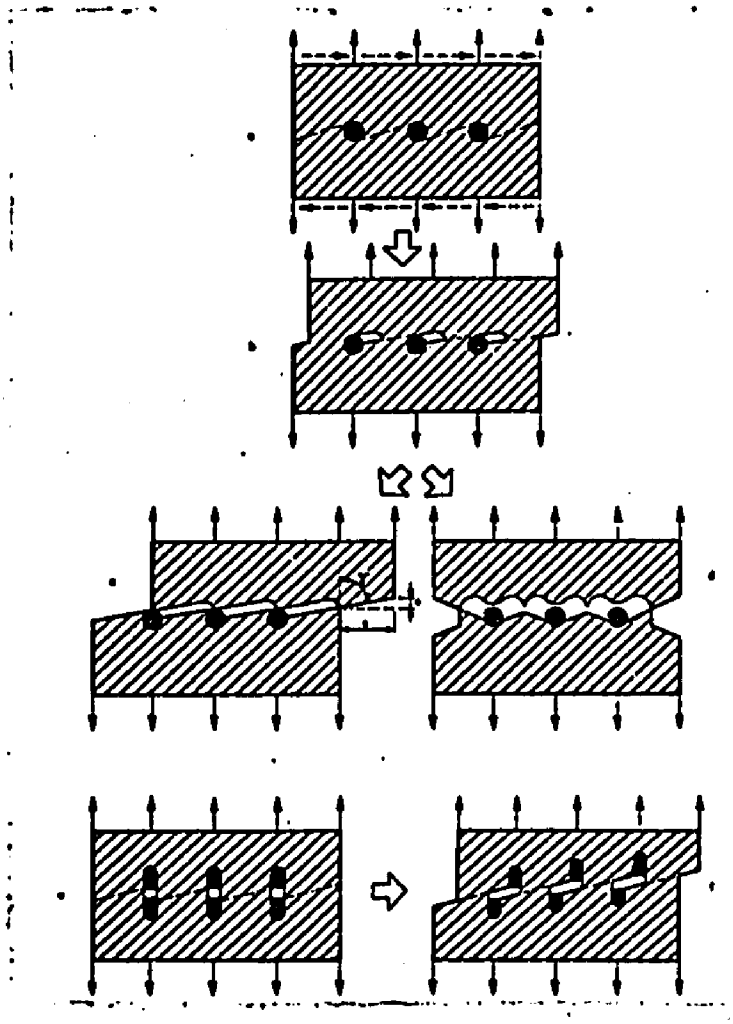

Figure 9. Void coalesence by the mechanism of Broek (44).

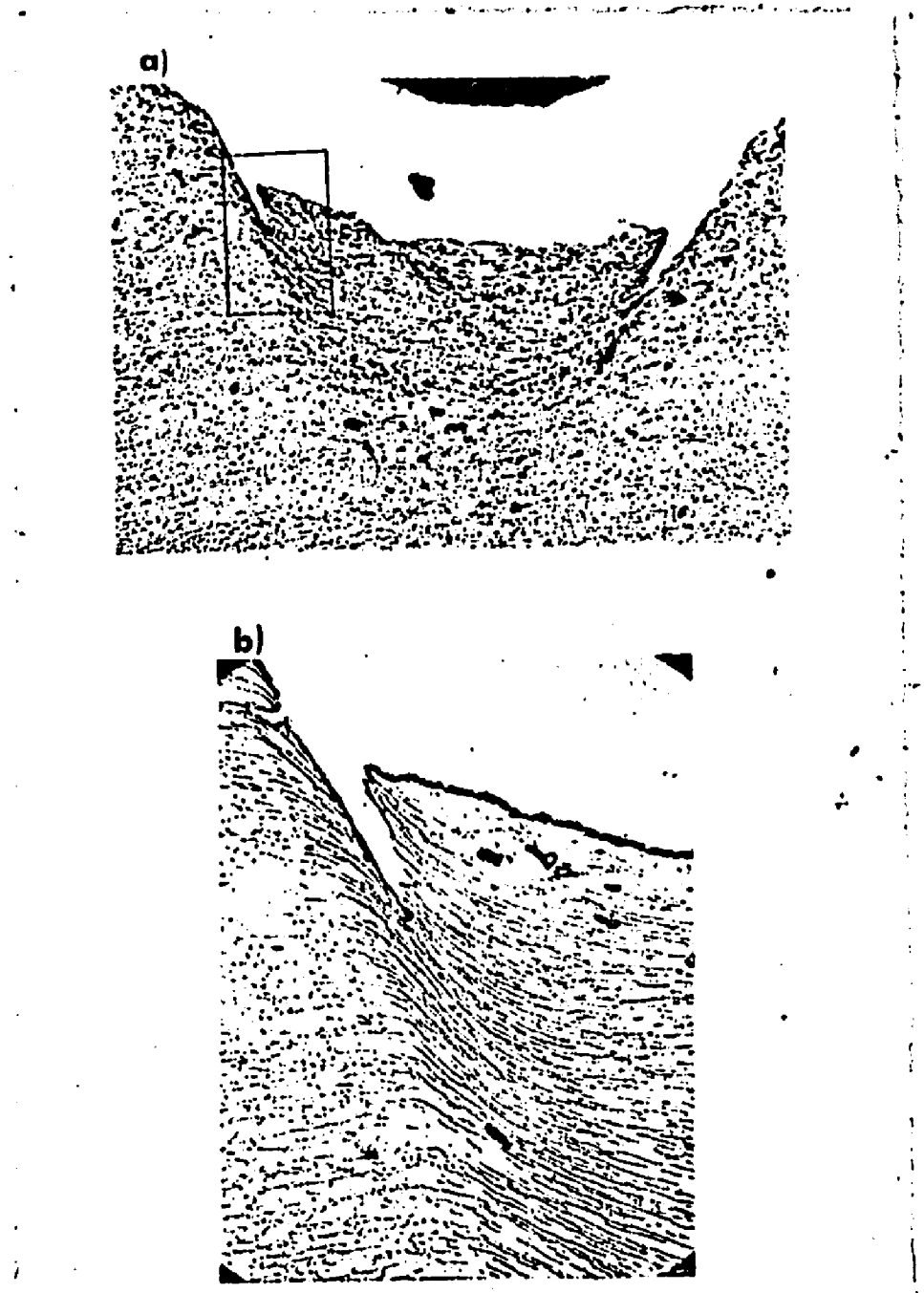

Figure 10. Localized flow at the notch in a DWT specimen of stainless steel, after Hayden and Floreen (52). (a) Cross-section of a nickel plated V-notch, 75X; (b) boxed in region of (a), 250X.

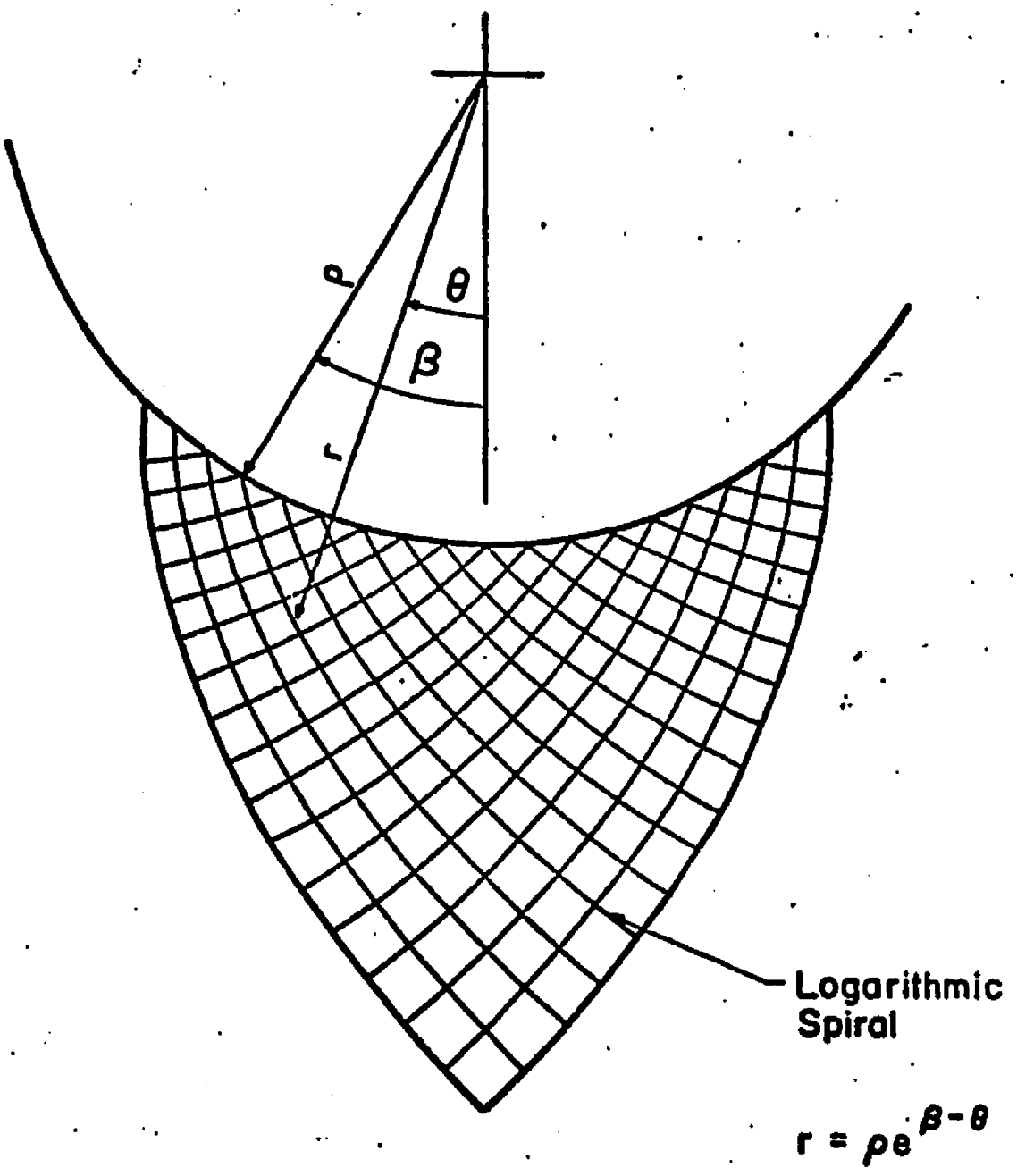

Figure 11. Theoretical slip-line field for circular stress-free boundary (Notch Root). (3)

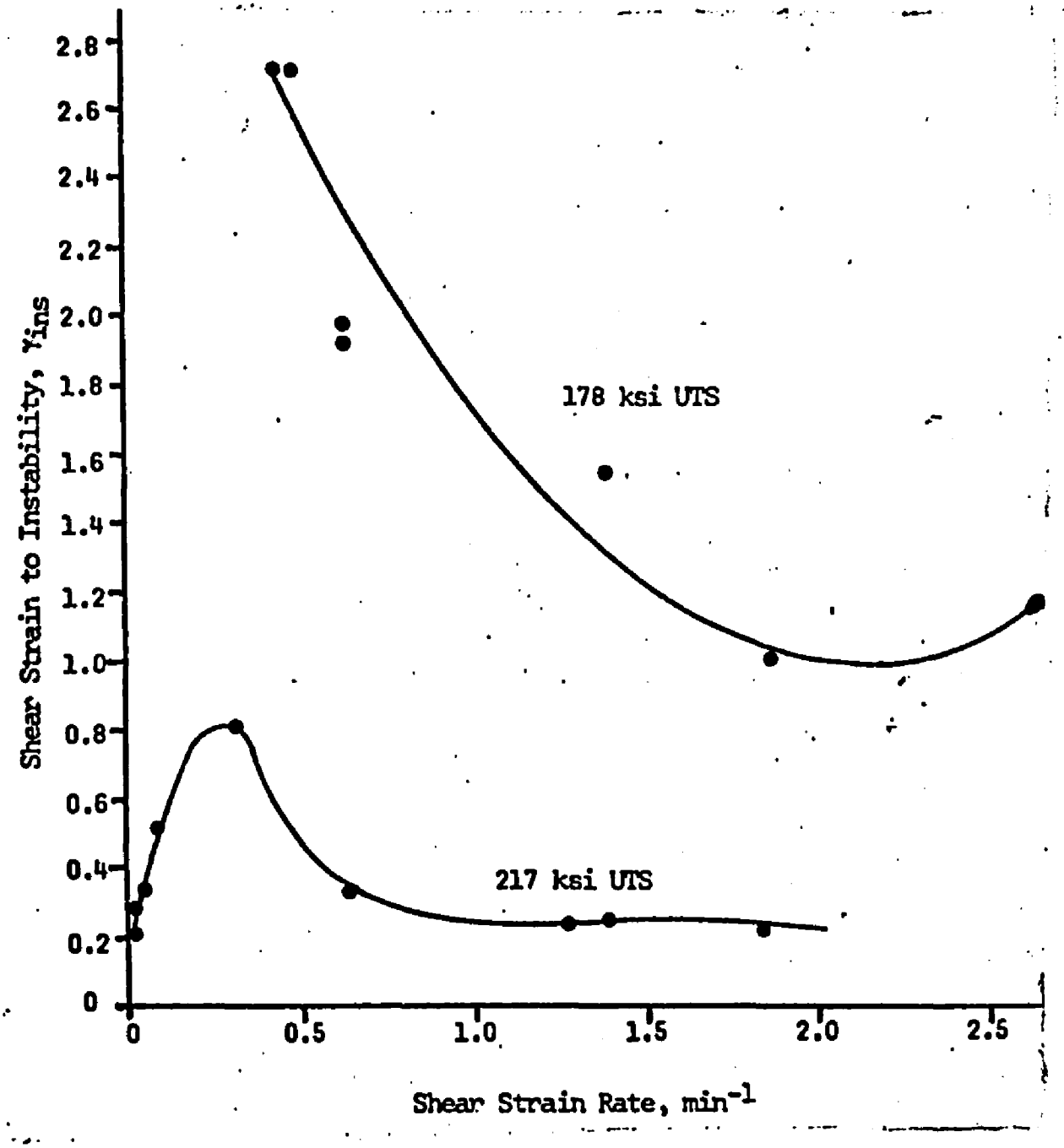

Figure 12. The effect of shear strain rate on the shear strain to instability in torsion of AISI 4340 steels, after Ernst and Spretnak (64).

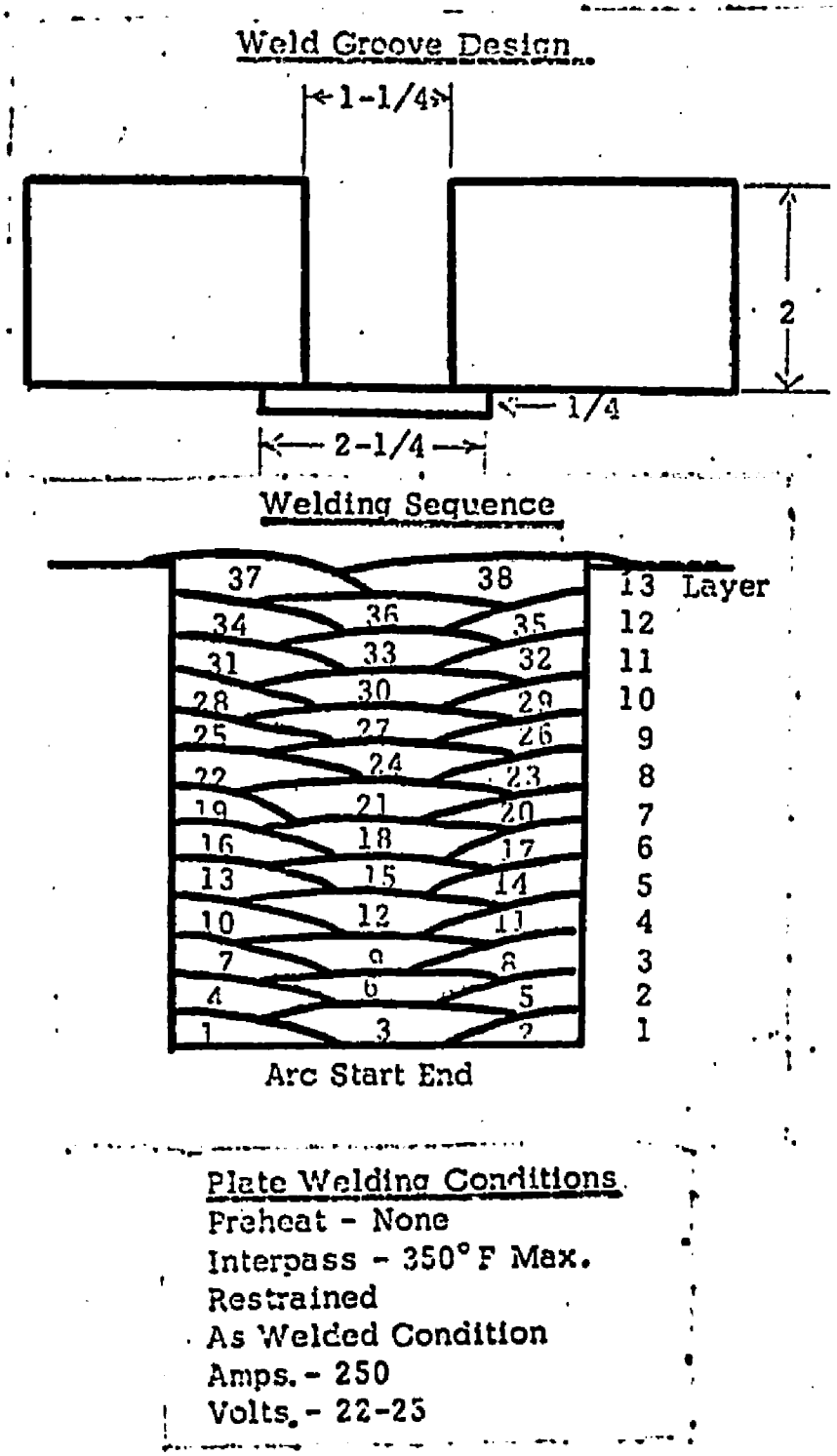

Figure 13. Summary of Preparation of Welded Plate.

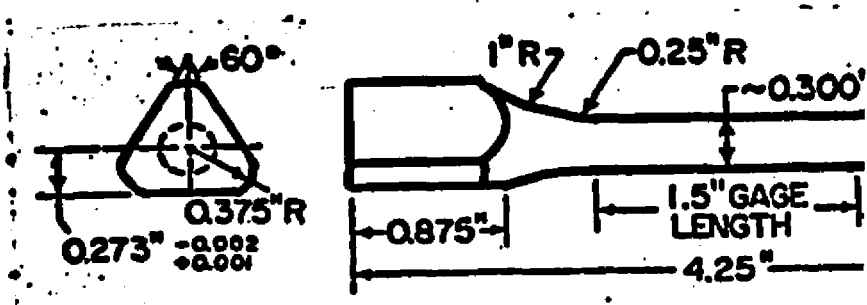

ROOM-TEMPERATURE TOR

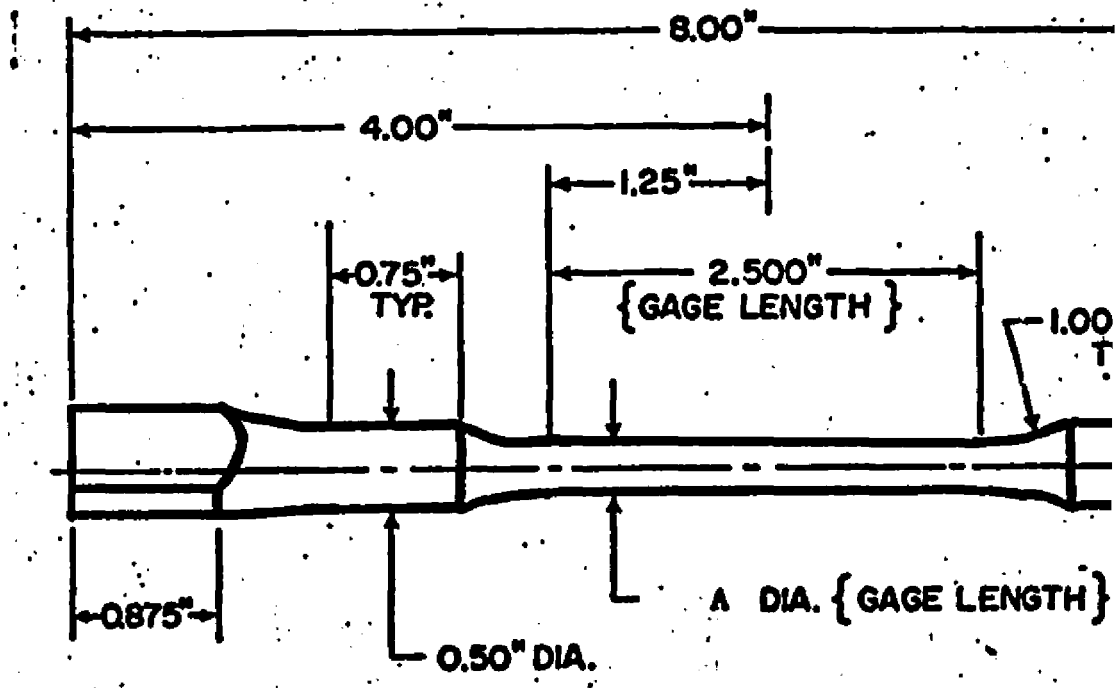

ELEVATED-TEMPERATURE TORSION SI

Diameter A	Specimen Ty
0.300 inches	Standard
0.250	Stress gradient st
0.200	Stress gradient st

Figure 14. Base Metal Torsion Test Specimens.

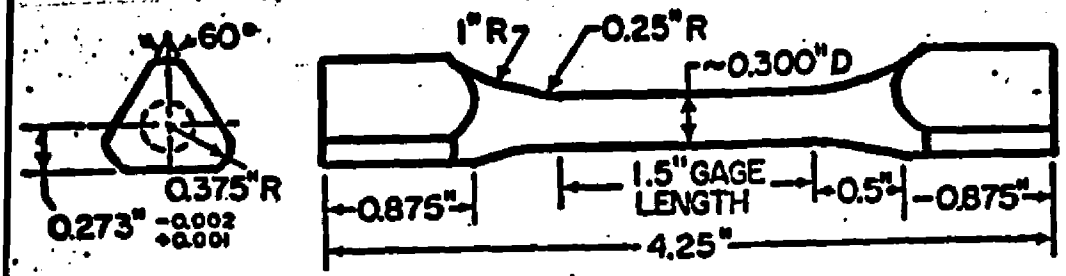

ROOM-TEMPERATURE TORSION SPECIMEN

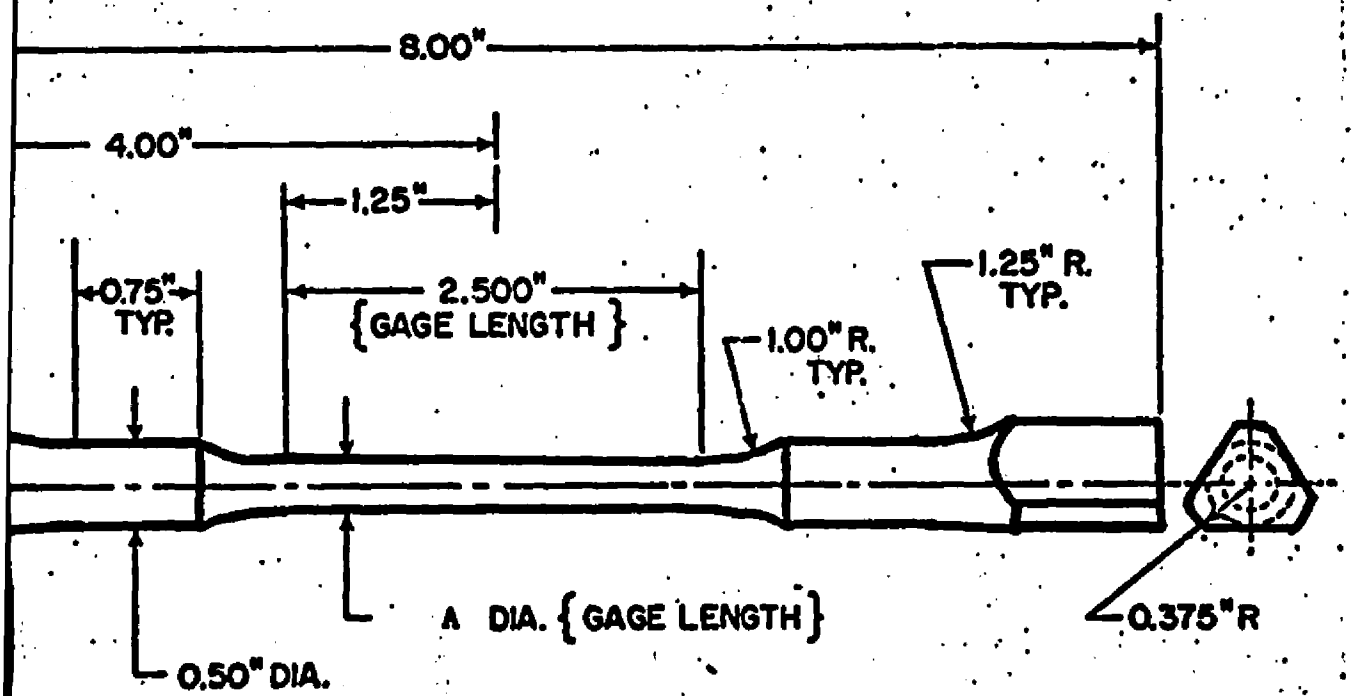

ELEVATED-TEMPERATURE TORSION SPECIMEN

Diameter A	Specimen Type
0.300 inches	Standard
0.250	Stress gradient studies
0.200	Stress gradient studies

ase Metal Torsion Test Specimens.

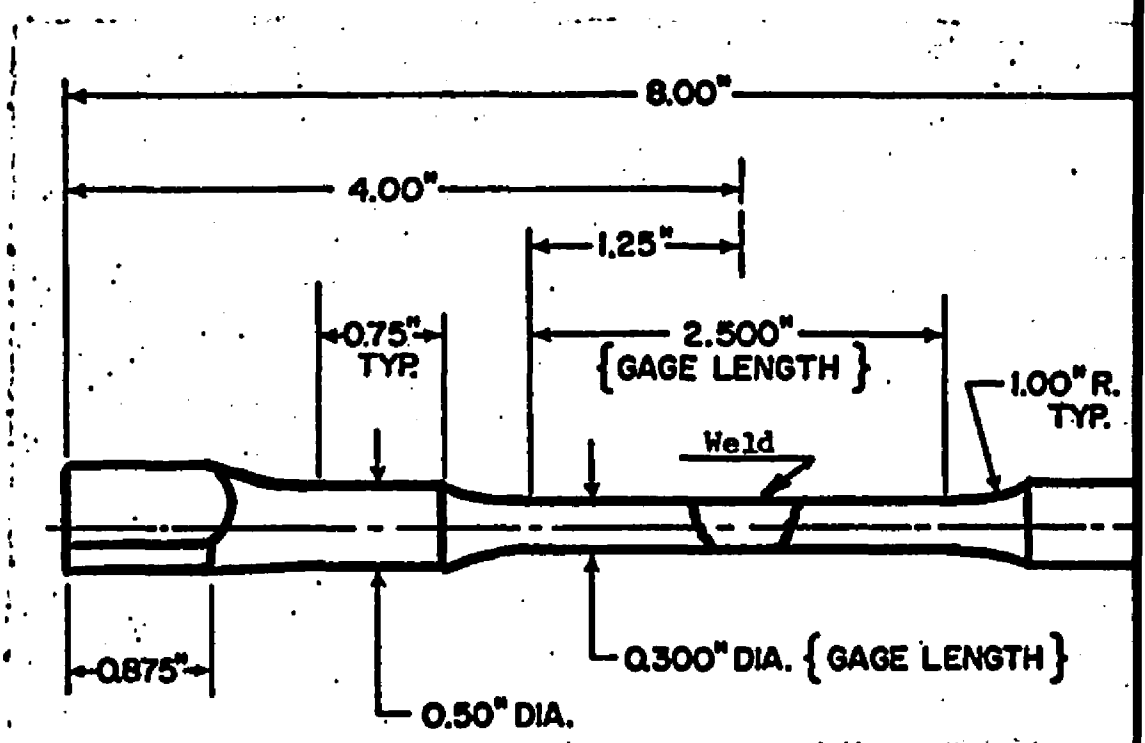

(b) Weld-Joint Torsion Specimen

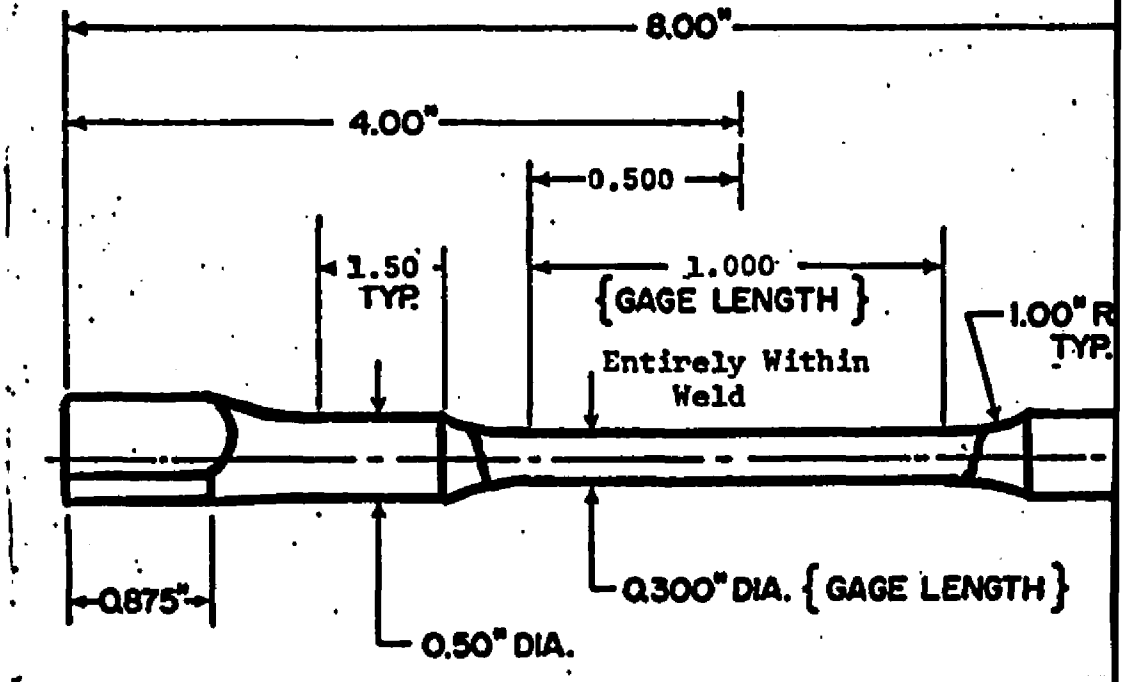

(a) Weld-Metal Torsion Specimen

Figure 15. Welded Torsion Specimens.

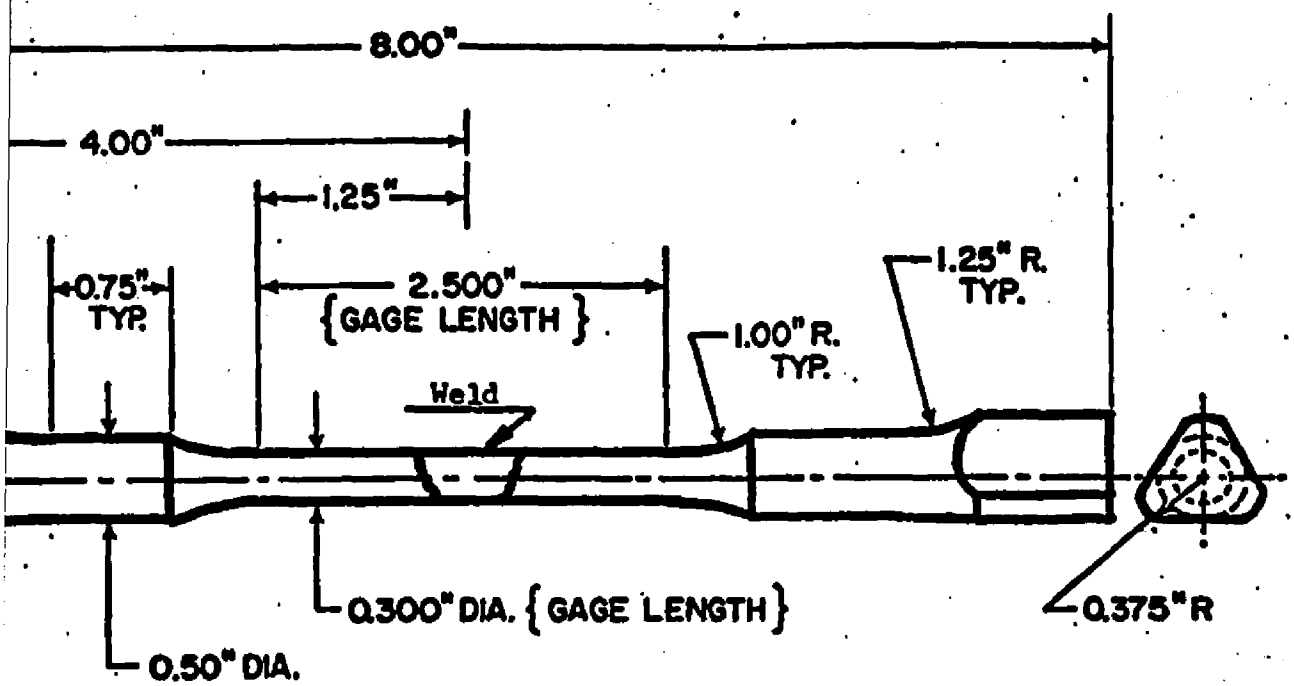

(b) Weld-Joint Torsion Specimen

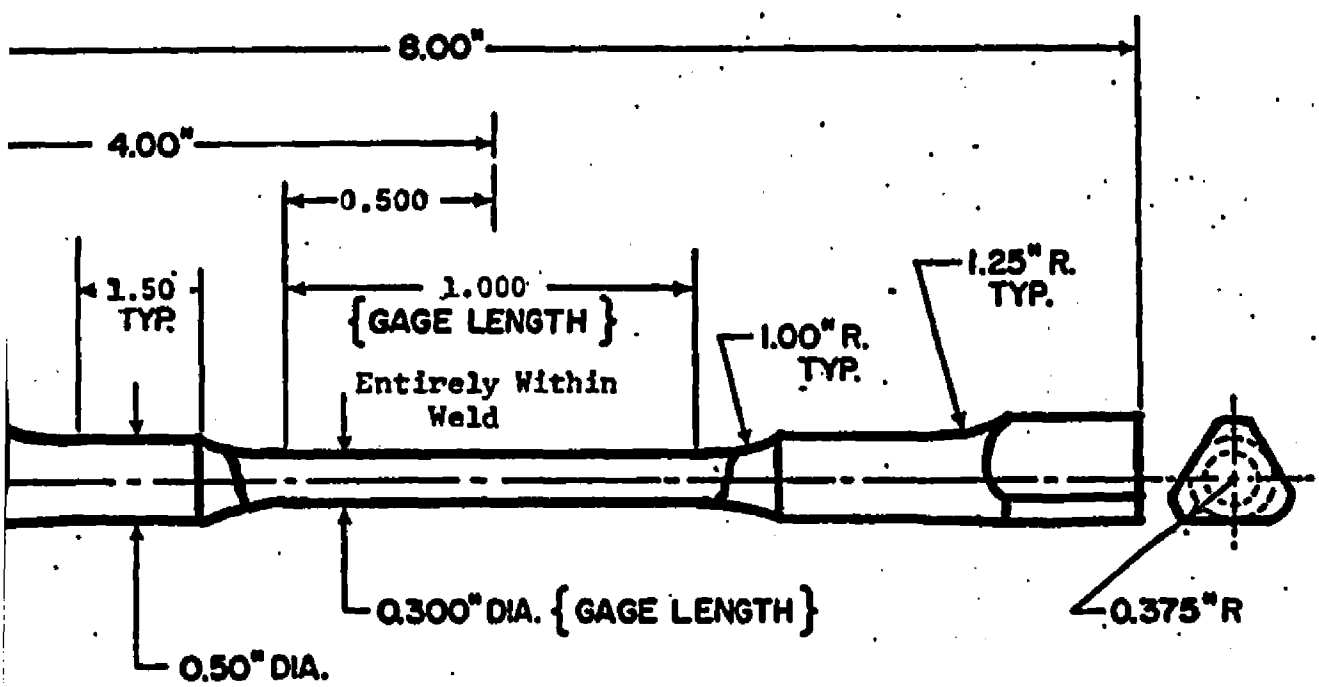

(a) Weld-Metal Torsion Specimen

Welded Torsion Specimens.

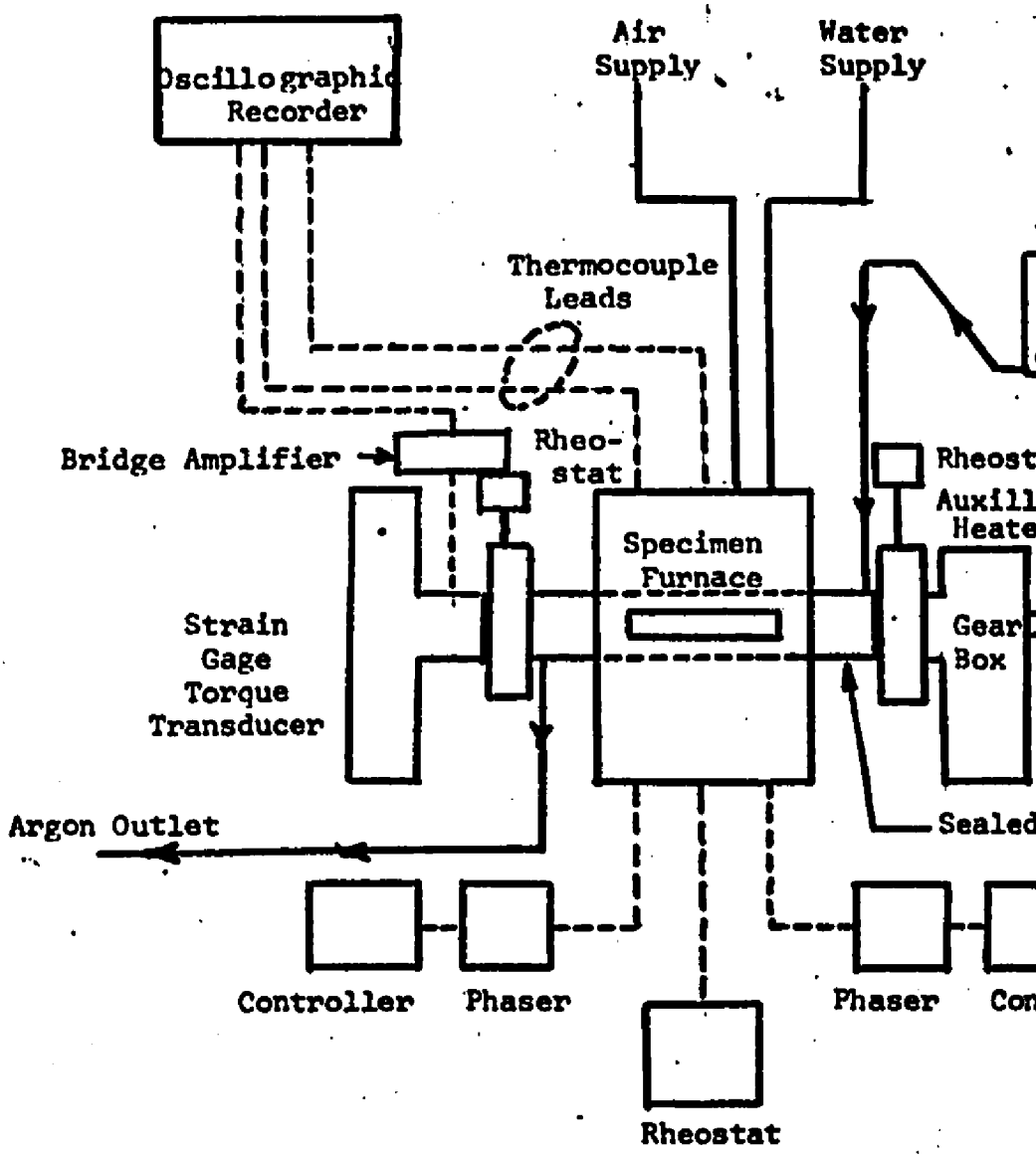

Figure 16. Schematic Diagram of Torsion Te

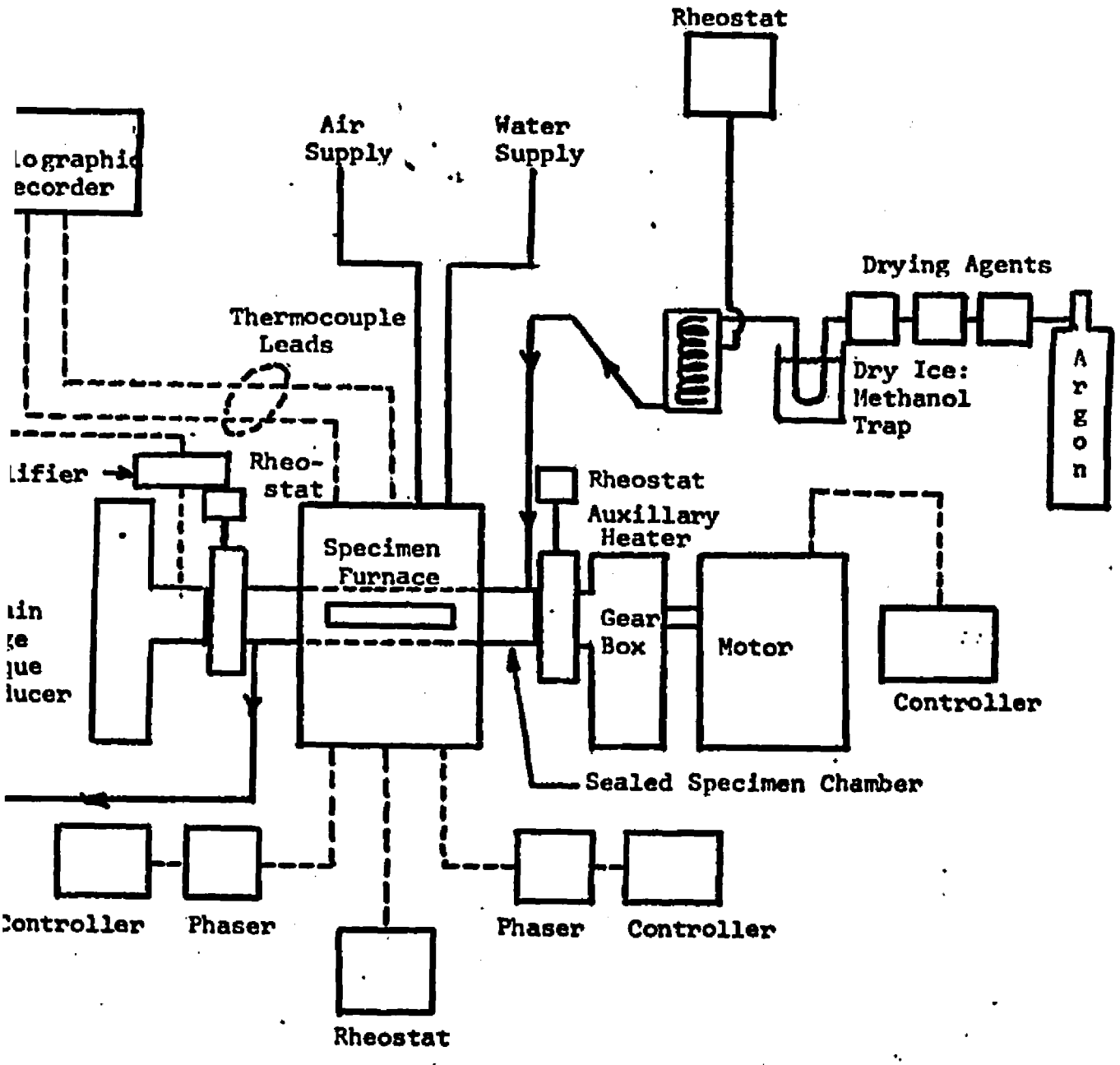

Figure 16. Schematic Diagram of Torsion Testing Equipment.

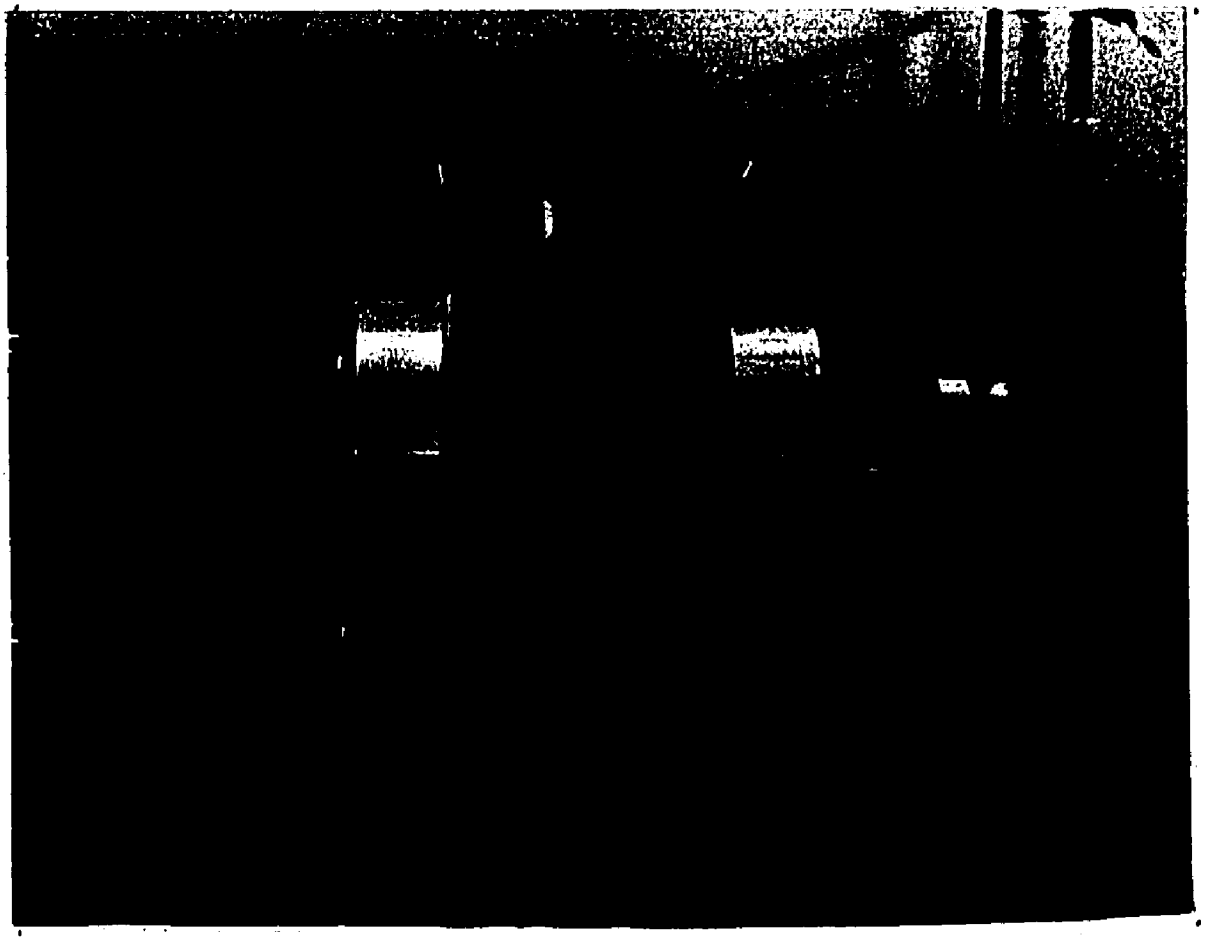

Figure 18. Elevated Temperature Torsion Testing Equipment.

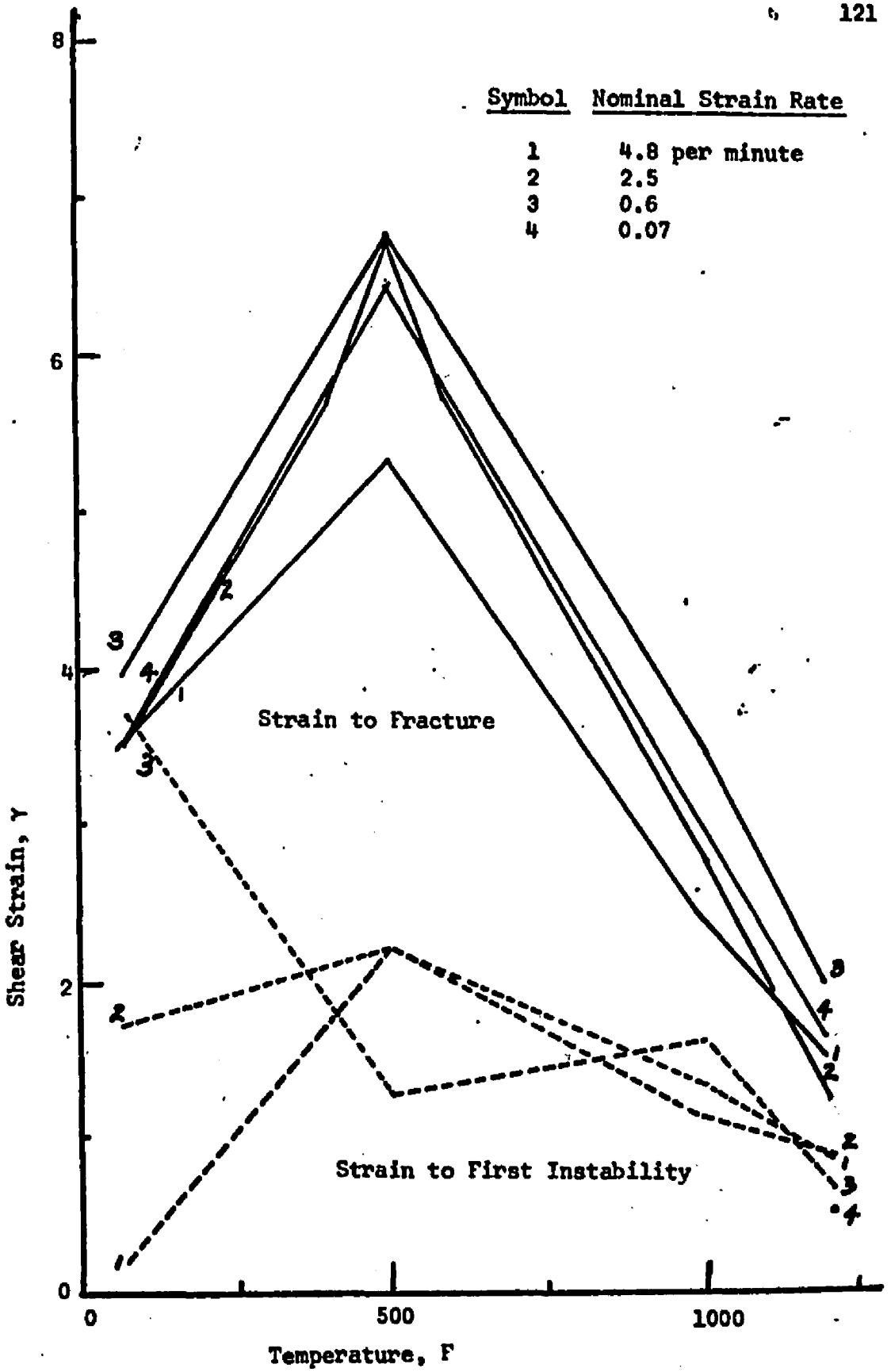

Figure 19. Strain to Fracture and Strain to First Instability versus Temperature at the Indicated Constant Strain-Rate for Solution Annealed Type 304 Stainless Steel Bar.

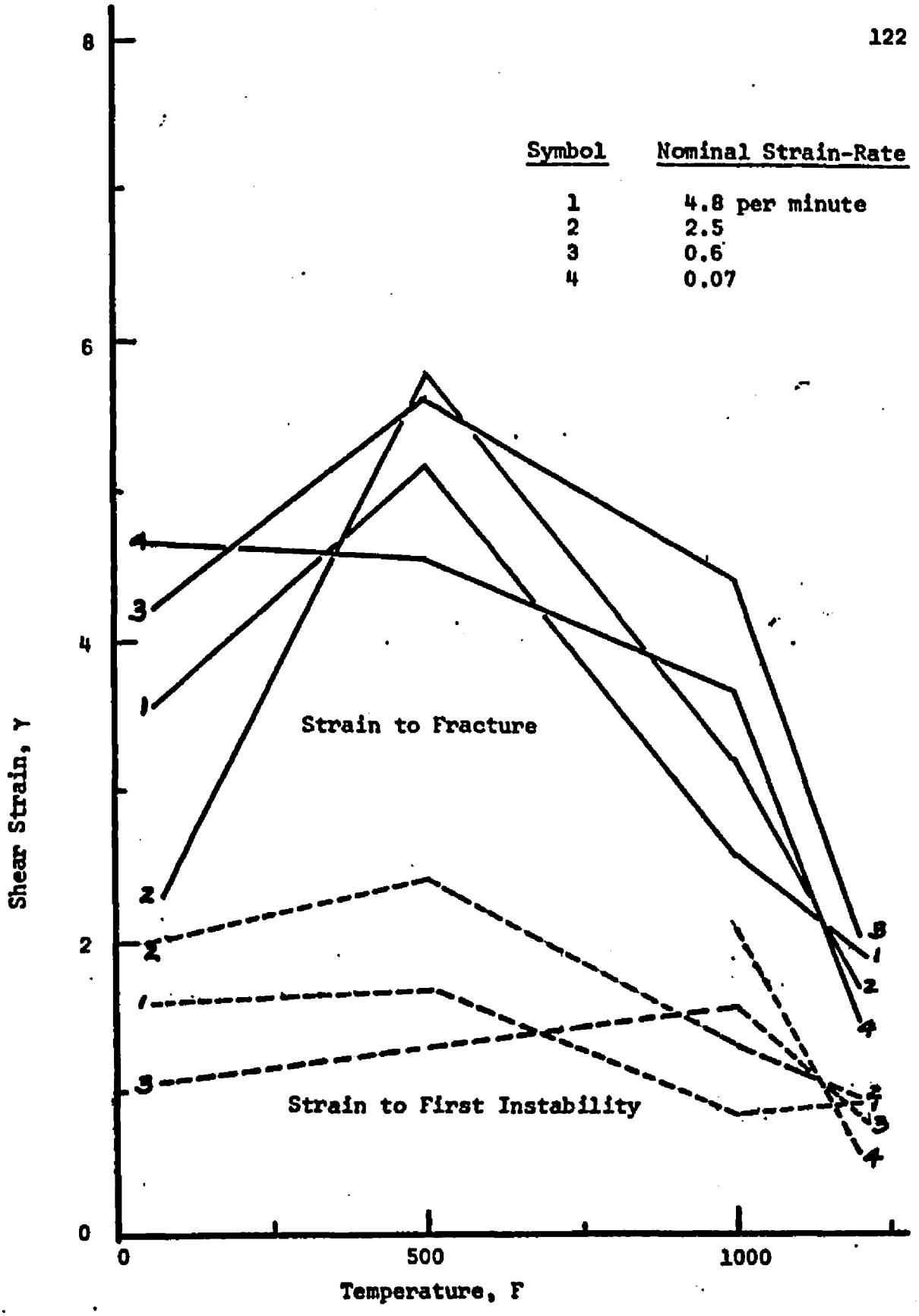

Figure 20. Strain to Fracture and Strain to First Instability versus Temperature at the Indicated Constant Strain-Rate for Sensitized Type 304 Stainless Steel Bar.

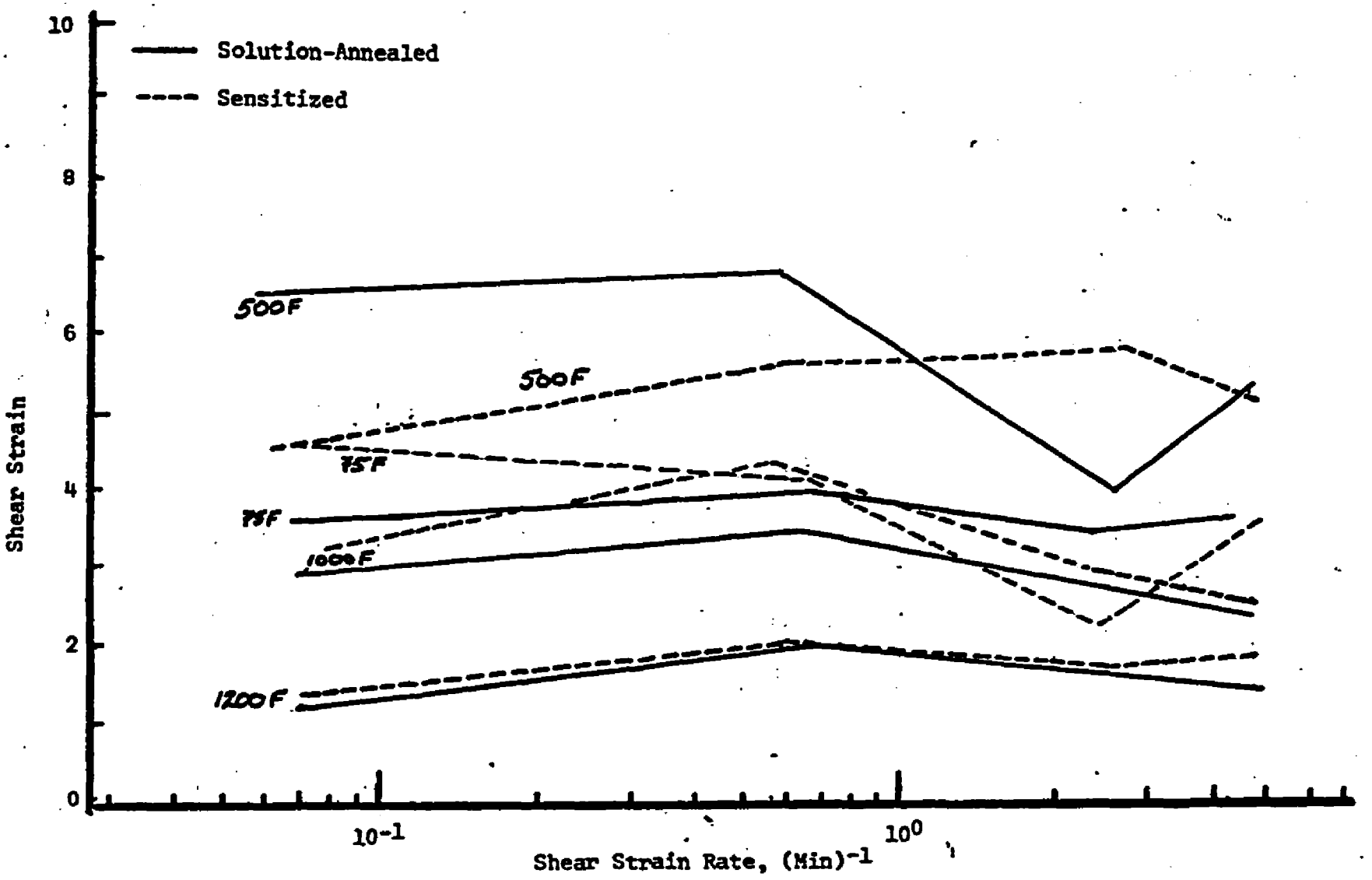

Figure 21. Strain to Fracture vs. Shear Strain-Rate at Constant Temperature for Solution-Annealed and Sensitized Type 304 Stainless Steel Bar.

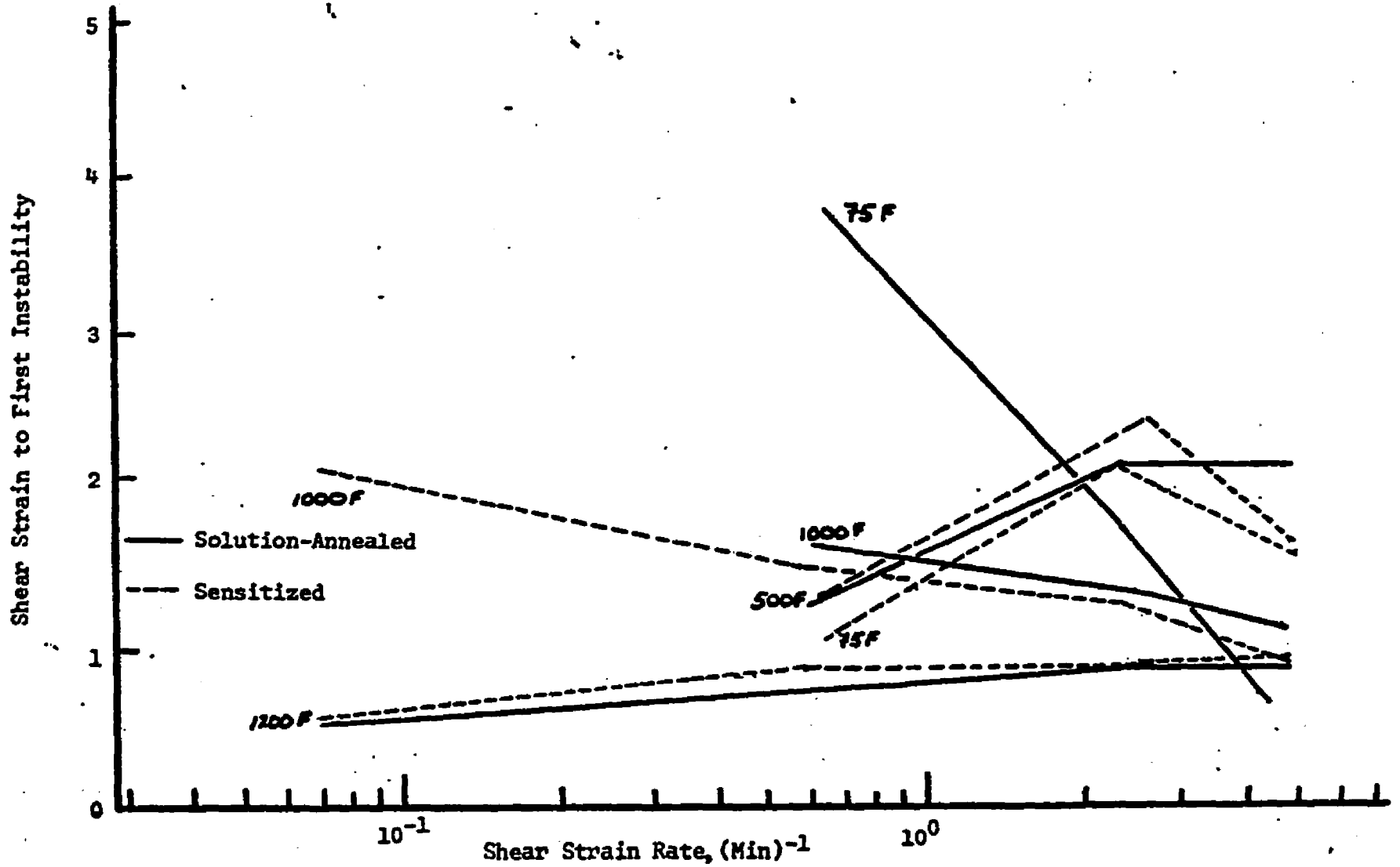

Figure 22. Strain to First Instability versus Shear Strain Rate at Constant Temperature for Solution-Annealed and Sensitized Type 304 Stainless Steel Bar.

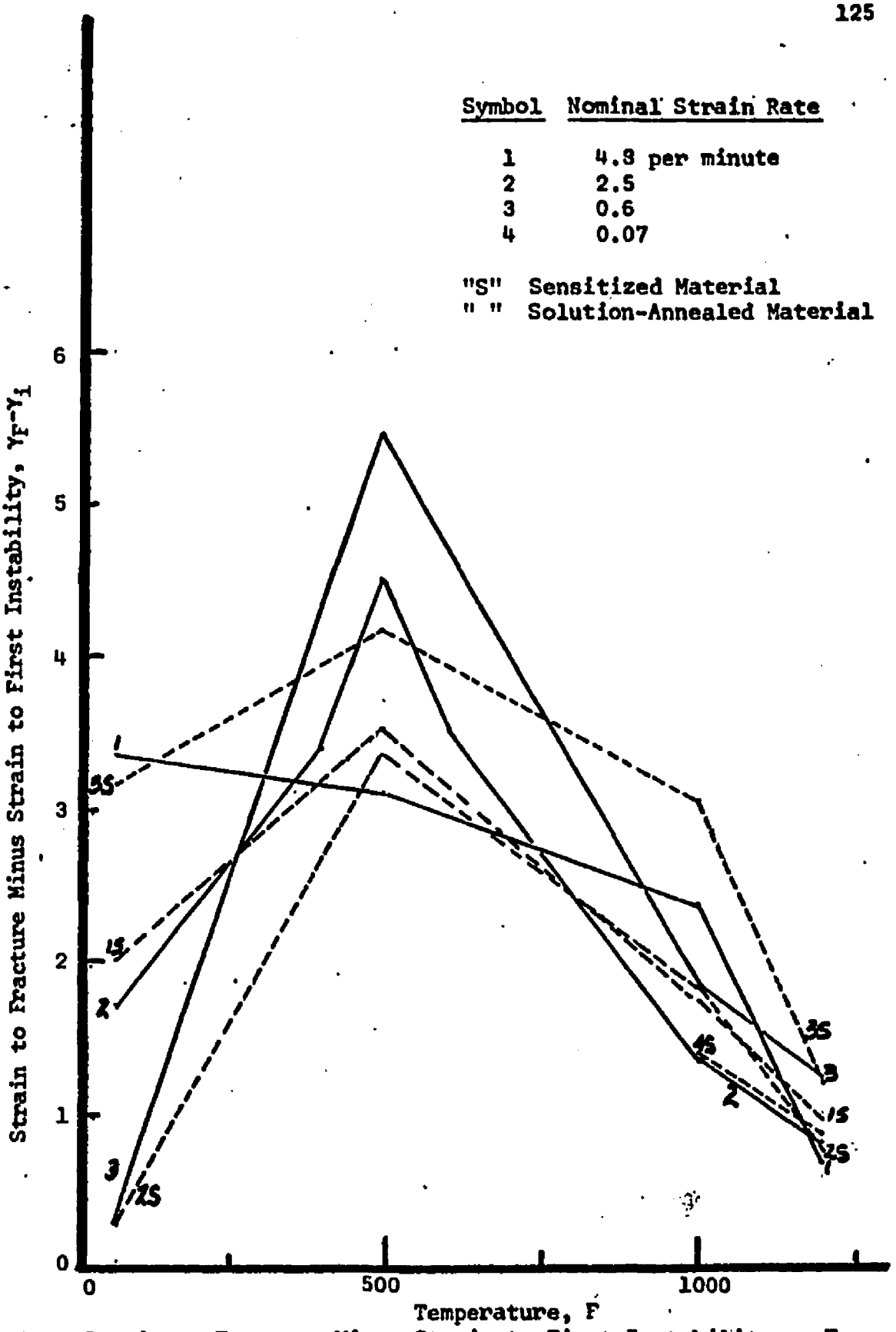

Figure 23. Strain to Fracture Minus Strain to First Instability vs Temperature at the Indicated Constant Strain-Rate for Type 304 Stainless Steel Bar.

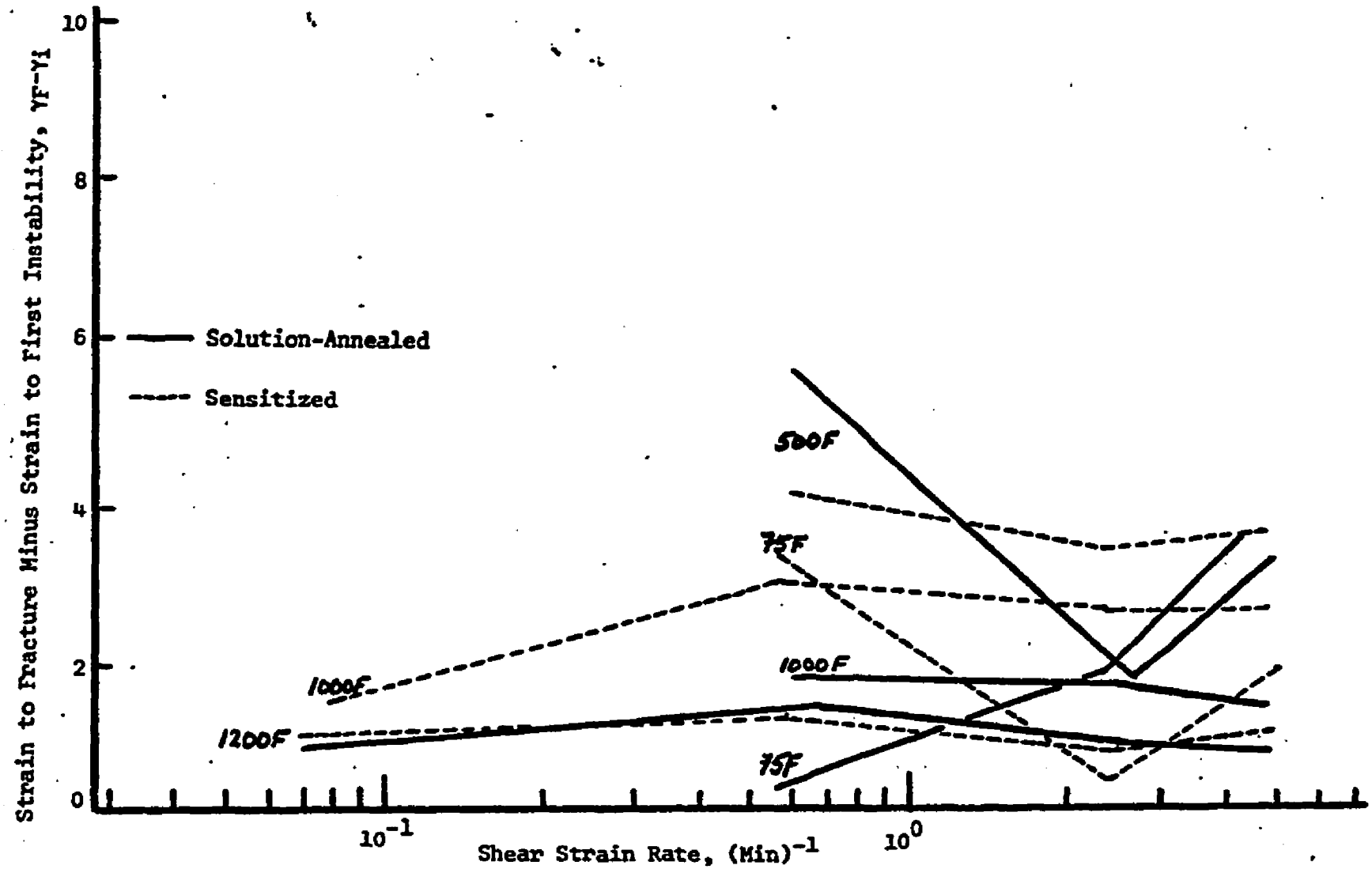

Figure 24. Strain to Fracture Minus Strain to First Instability versus Strain-Rate at Indicated Temperatures for Type 304 Stainless Steel Bar.

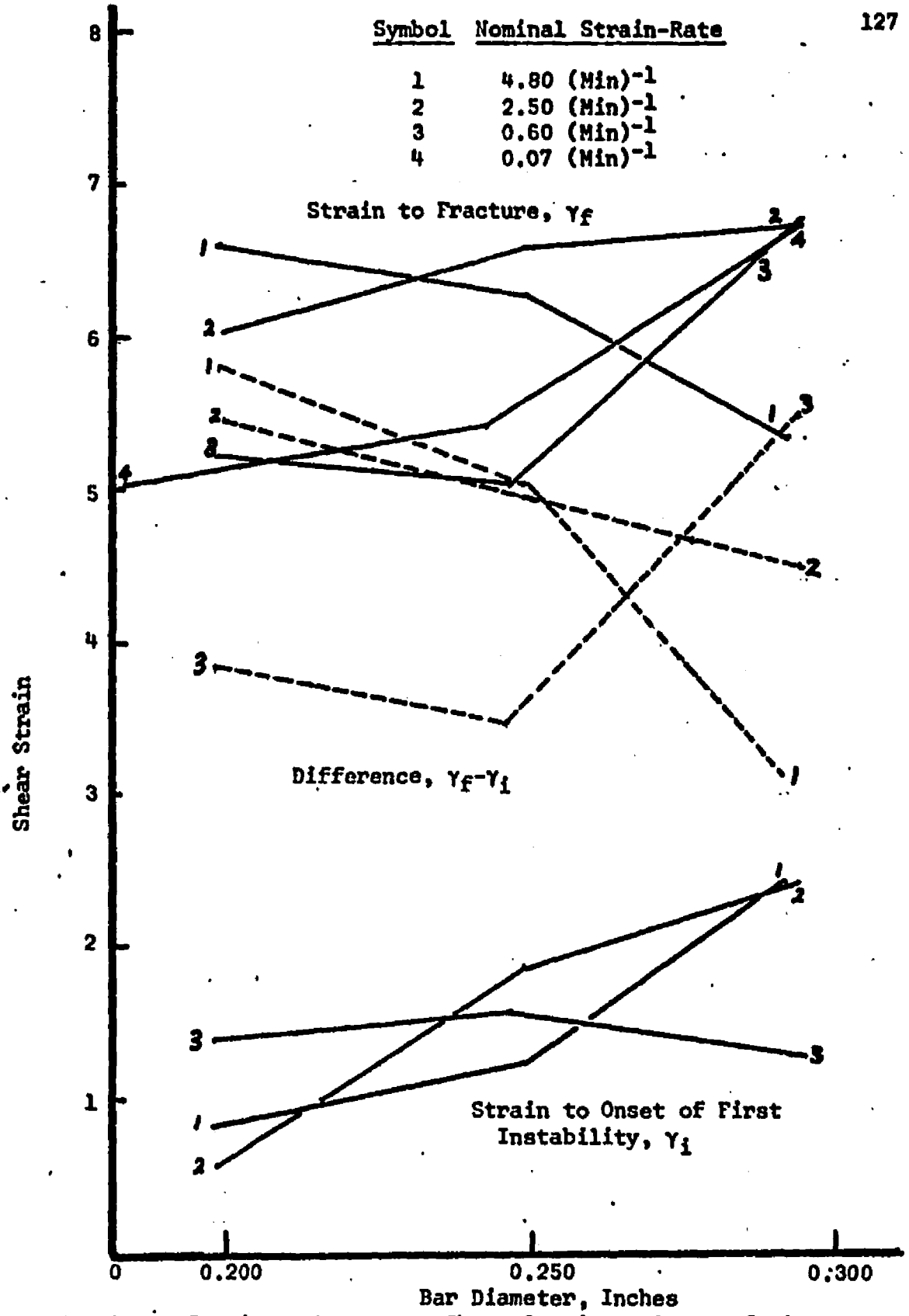

Figure 25. Shear Strain to Fracture, Shear Strain to Onset of First Instability, and their Difference versus Bar Diameter at 500°F and the Indicated Nominal Strain-Rates for Solution-Annealed Type 304 Stainless Steel Bar.

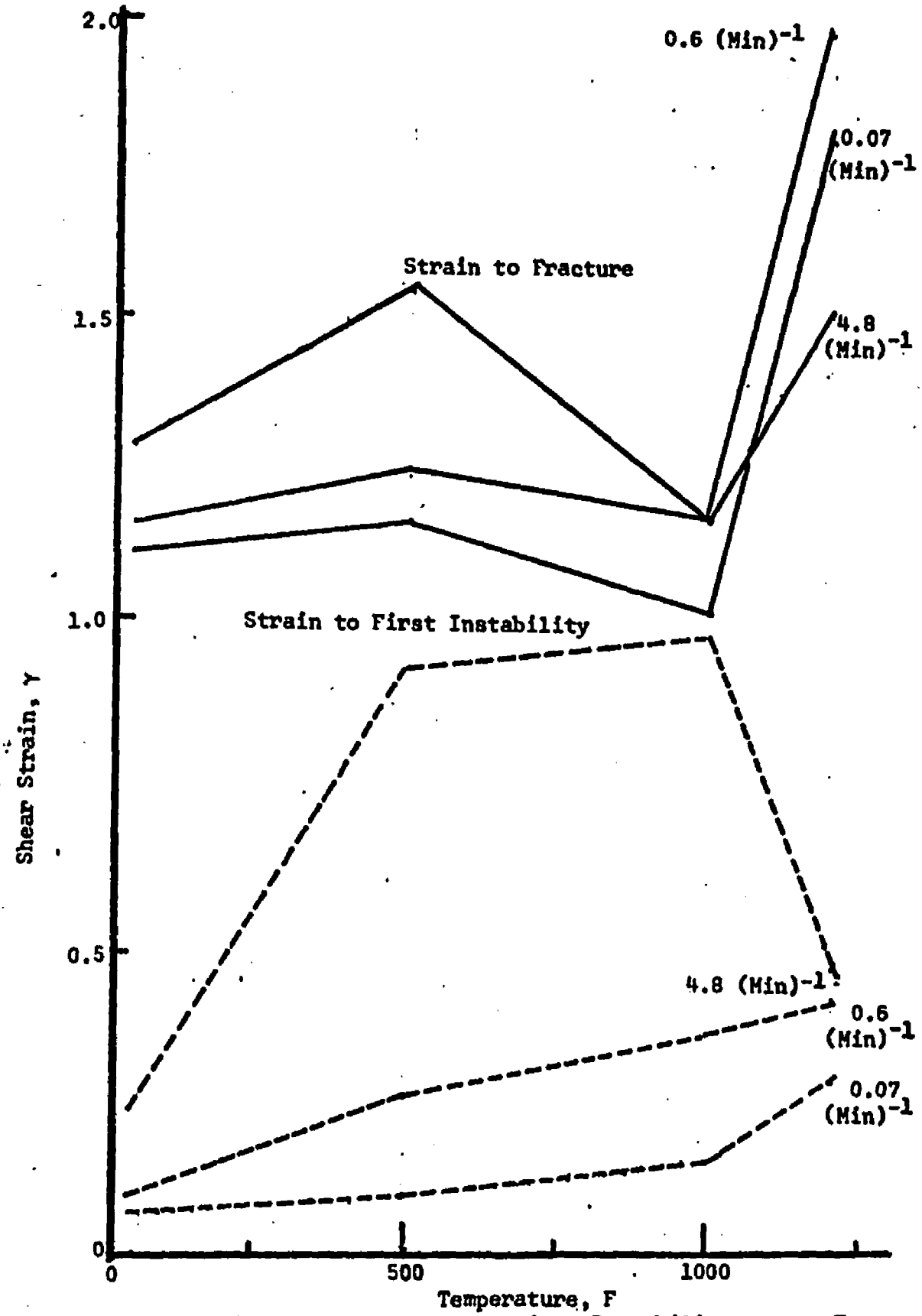

Figure 26. Shear Strain to Fracture and to First Instability versus Temperature at the Indicated Nominal Strain-Rates for all Weld-Metal Specimens.

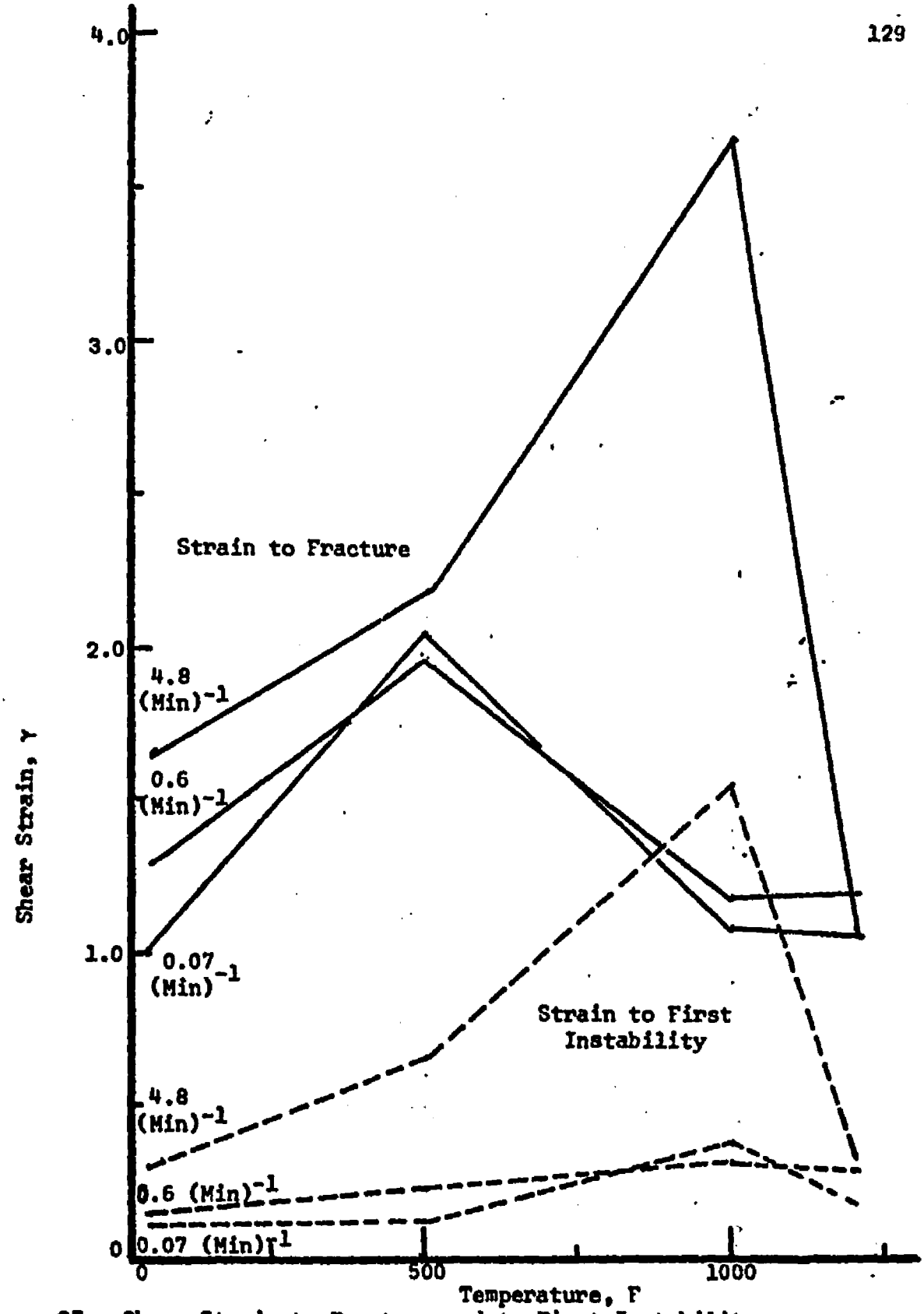

Figure 27. Shear Strain to Fracture and to First Instability versus Temperature at the Indicated Nominal Strain-Rates for Weld-Joint Specimens.

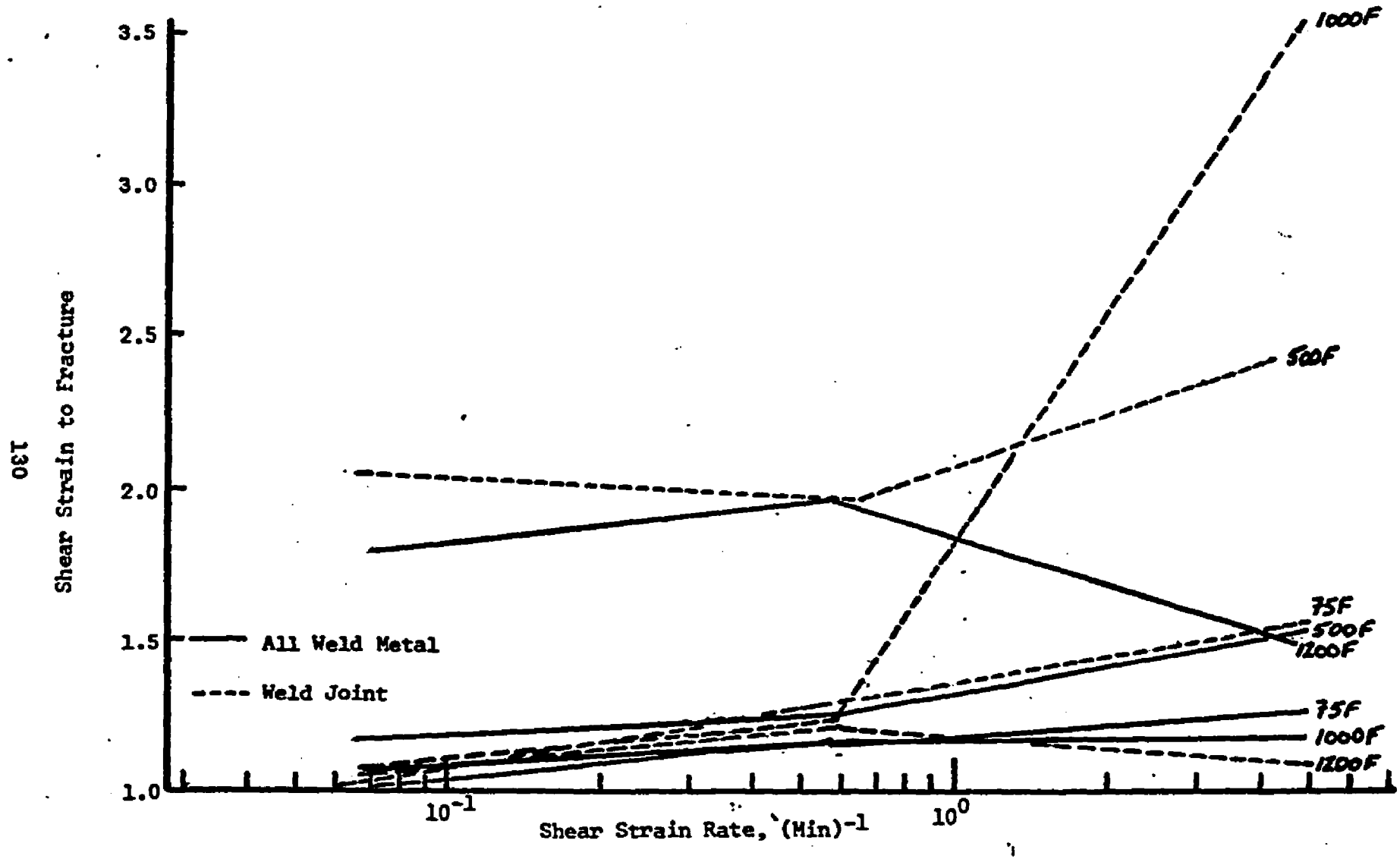

Figure 28. Shear Strain to Fracture versus Strain Rate at Constant Temperature for Welded Samples.

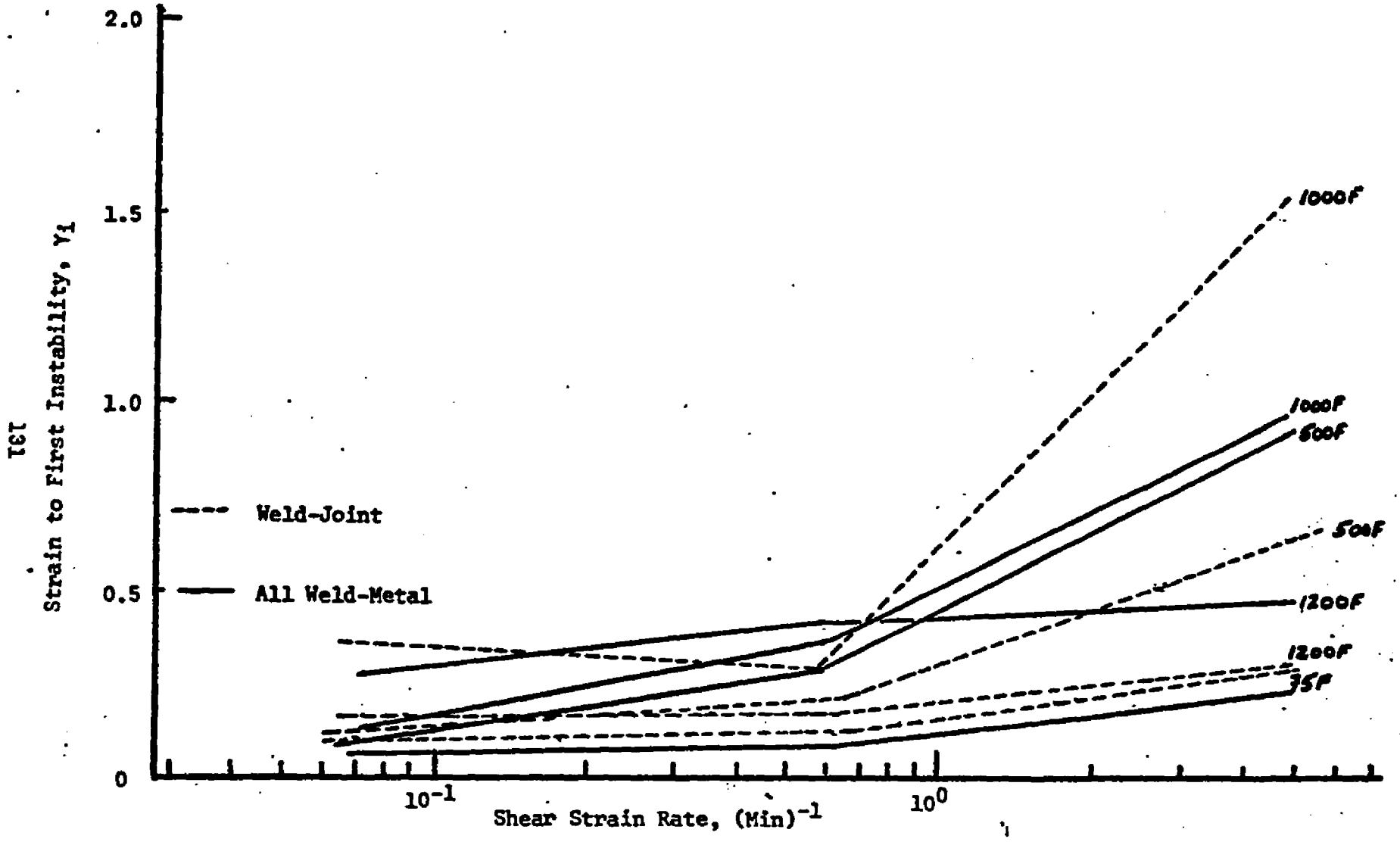

Figure 29. Strain to First Instability versus Strain-Rate at Indicated Constant Temperatures for Welded Samples.

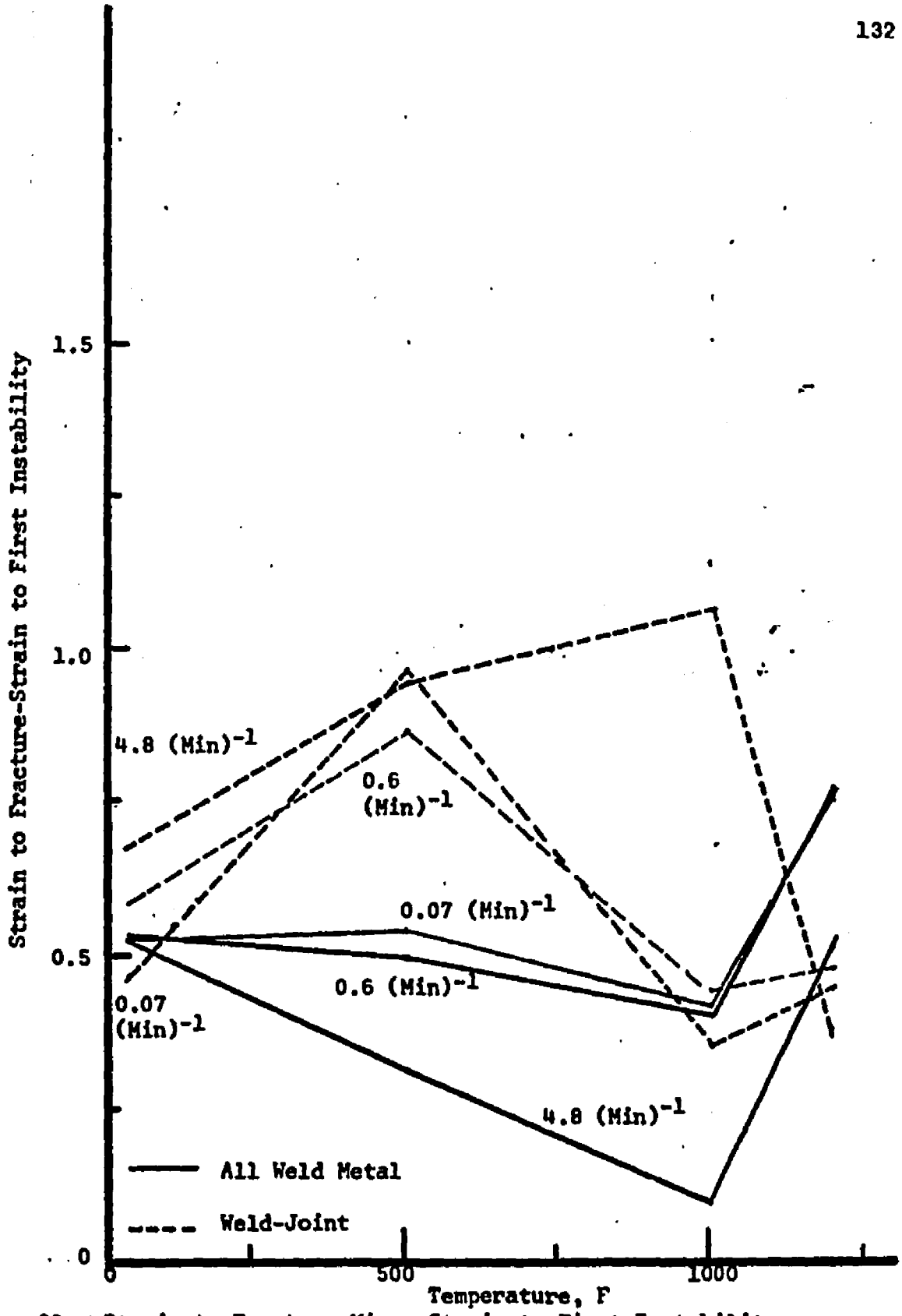

Figure 30. Strain to Fracture Minus Strain to First Instability versus Temperature at the Indicated Nominal Strain-Rates for Welded Specimens.

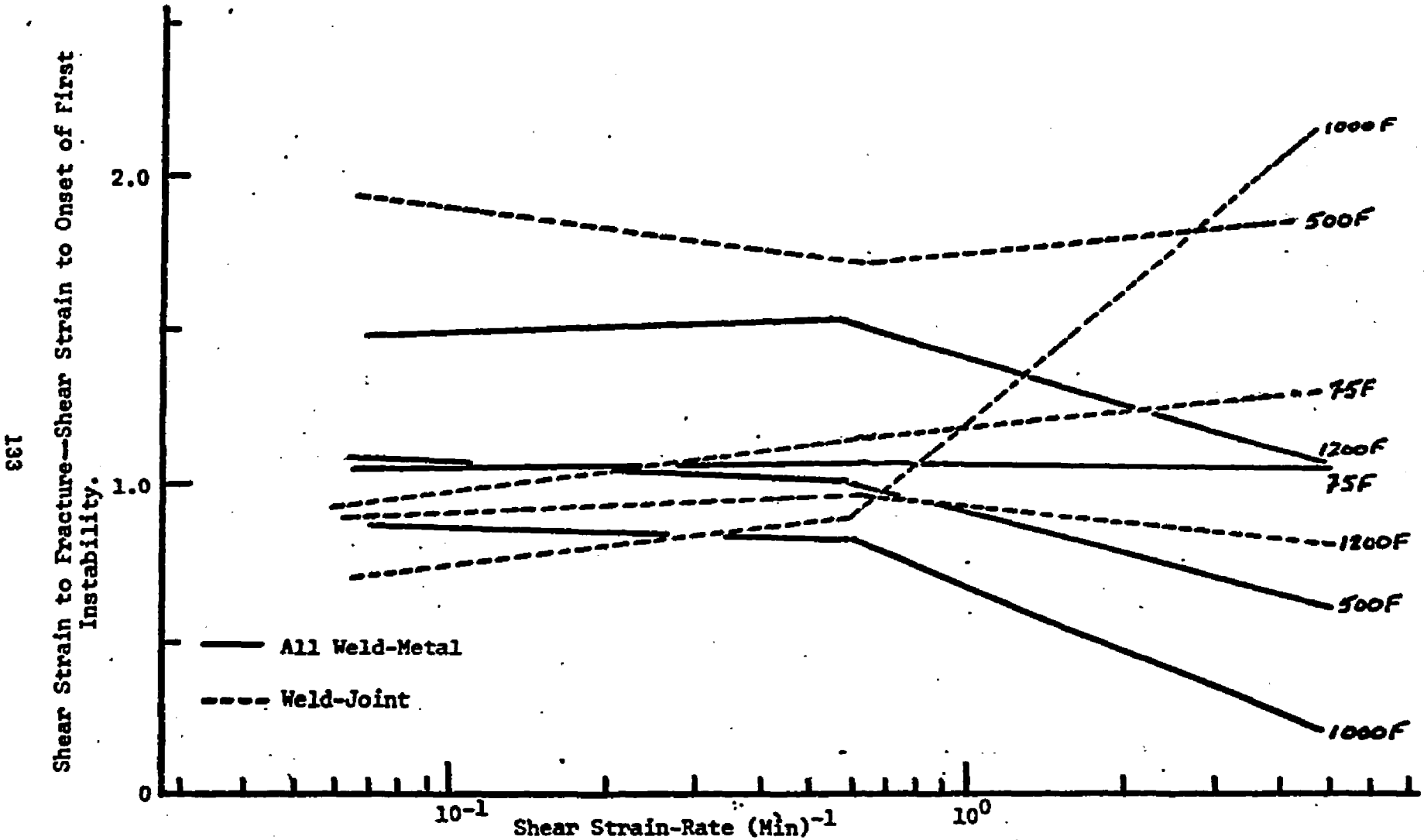

Figure 31. Shear Strain to Fracture Minus Shear Strain to First Instability versus Strain-Rate at the Indicated Constant Temperatures for Welded Specimens.

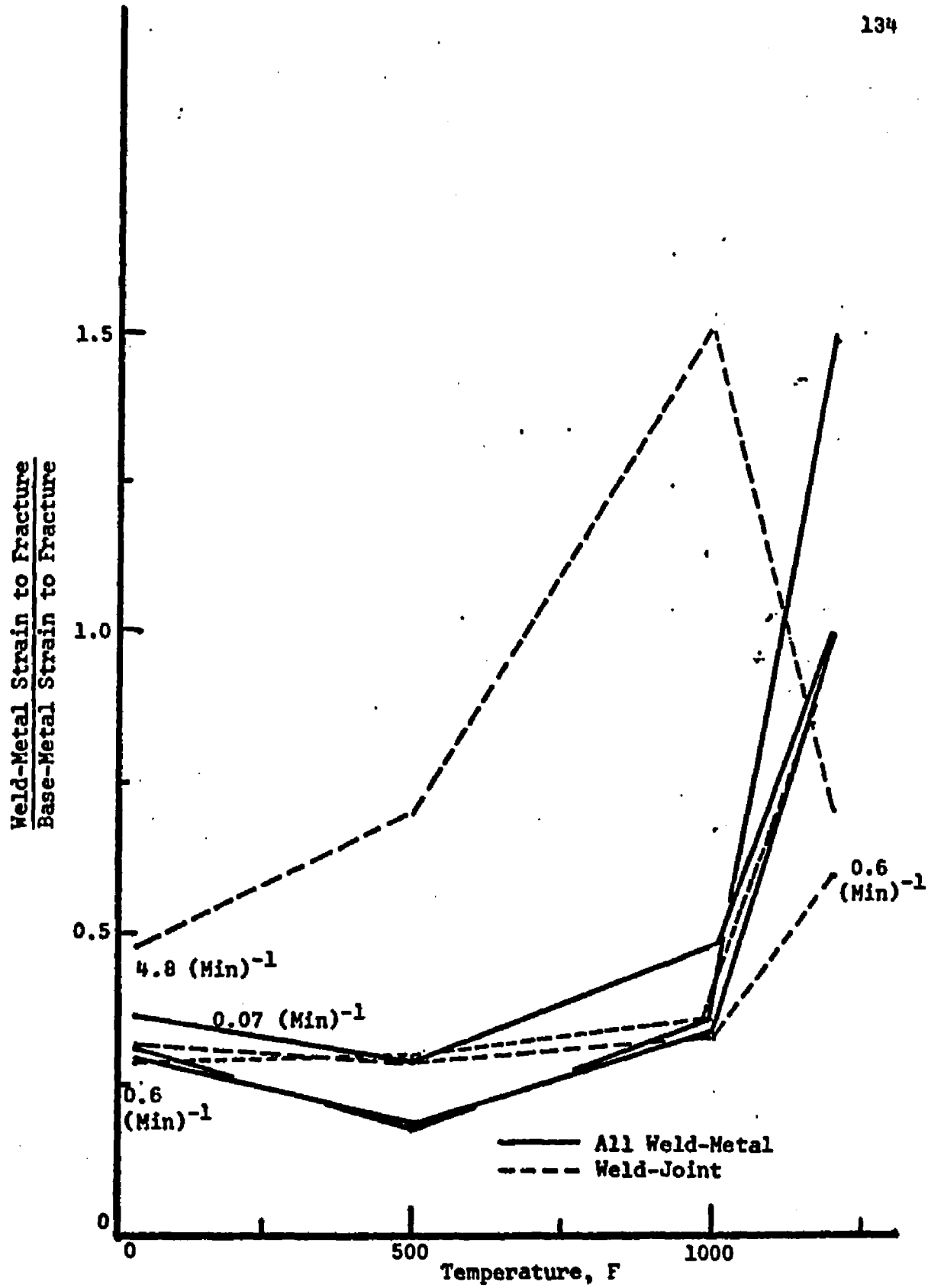

Figure 32. Ratio of Weld Metal Fracture-Strain to Base-Metal Fracture-Strain versus Temperature at Indicated Nominal Strain-Rates for Welded Specimens.

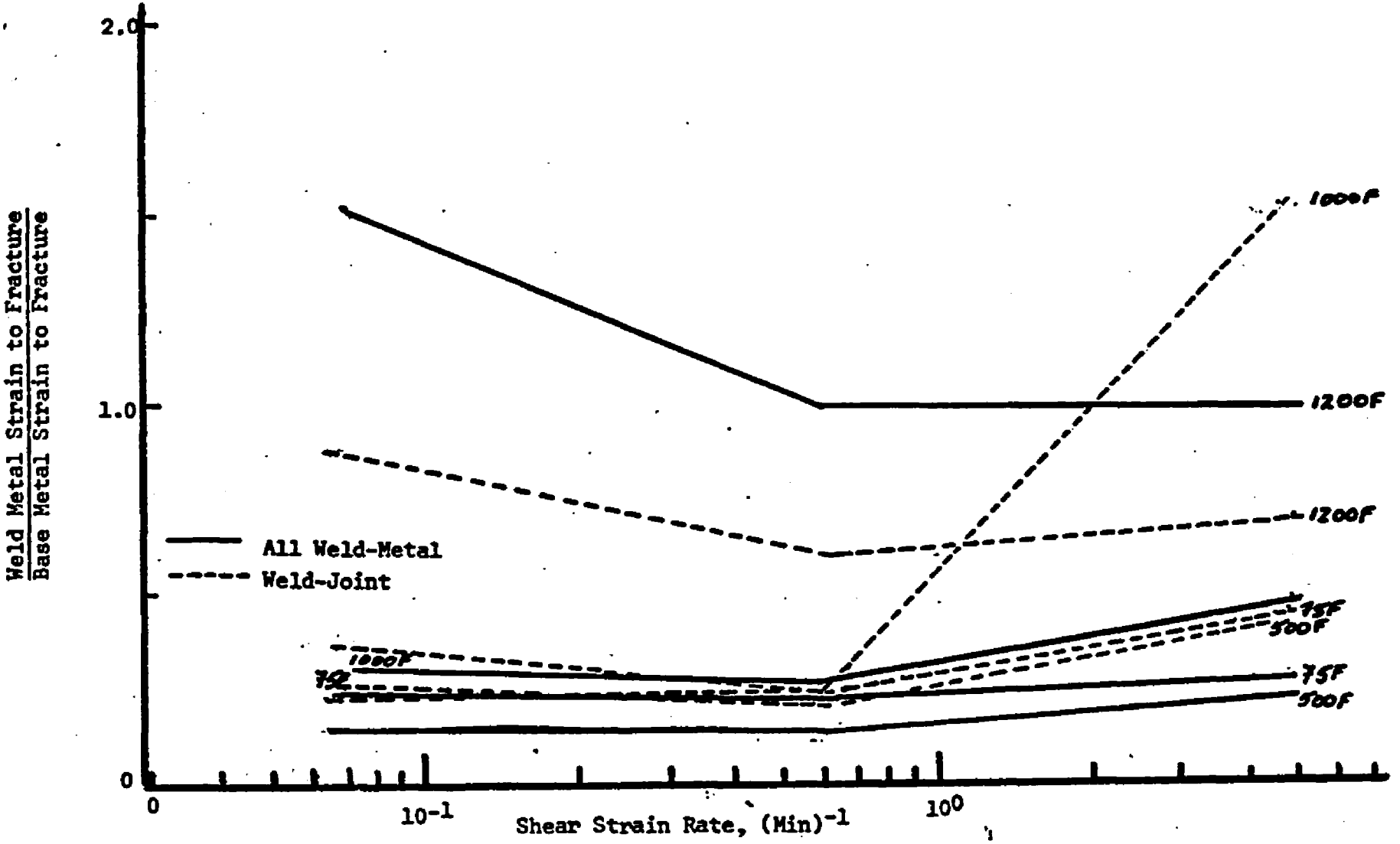

Figure 33. Ratio of Weld-Metal Fracture Strain to Base-Metal Fracture-Strain as a Function of Strain-Rate at the Indicated Temperatures.

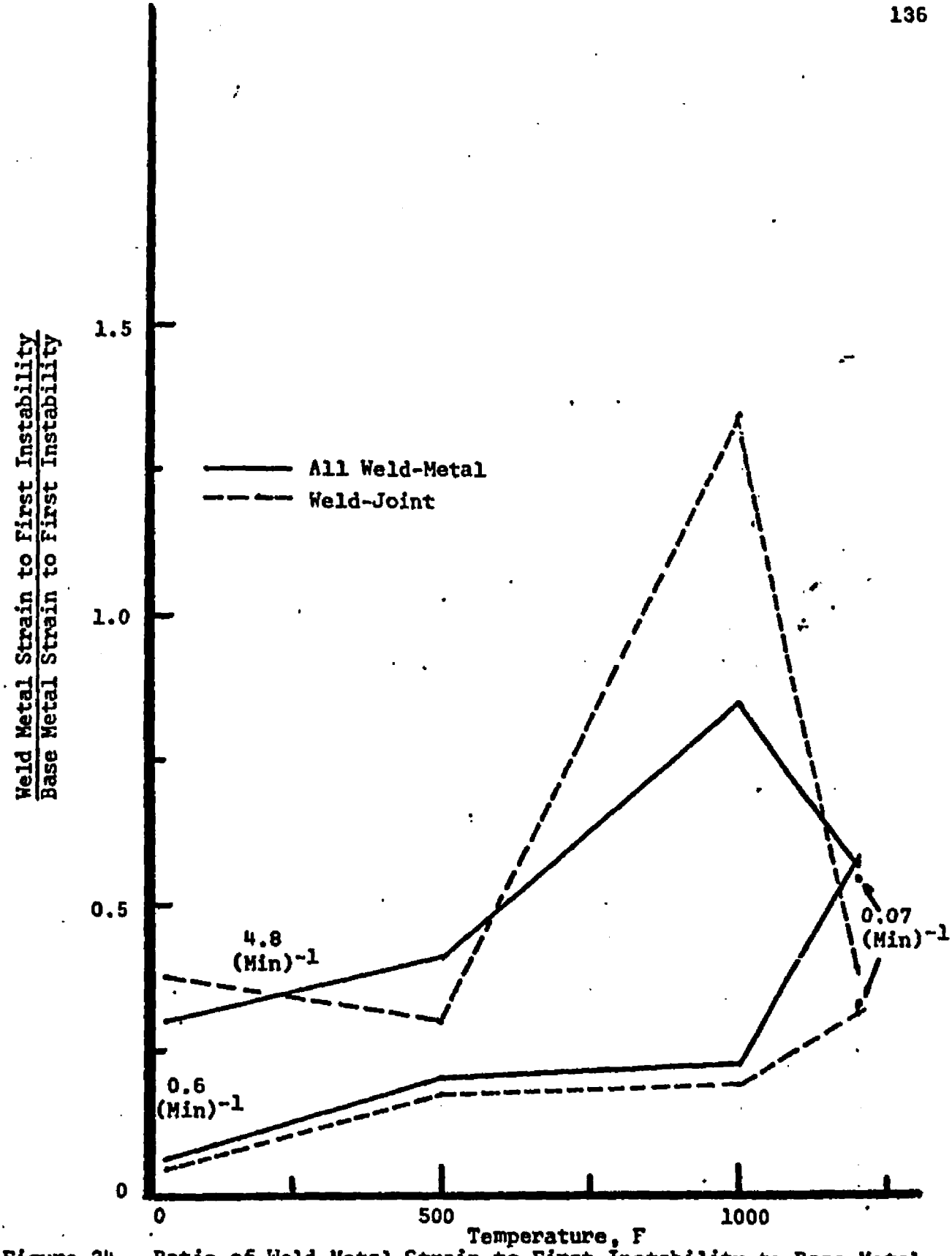

Figure 34. Ratio of Weld Metal Strain to First Instability to Base-Metal Strain to First Instability versus Temperature at Indicated Nominal Strain-Rates for Welded Specimens.

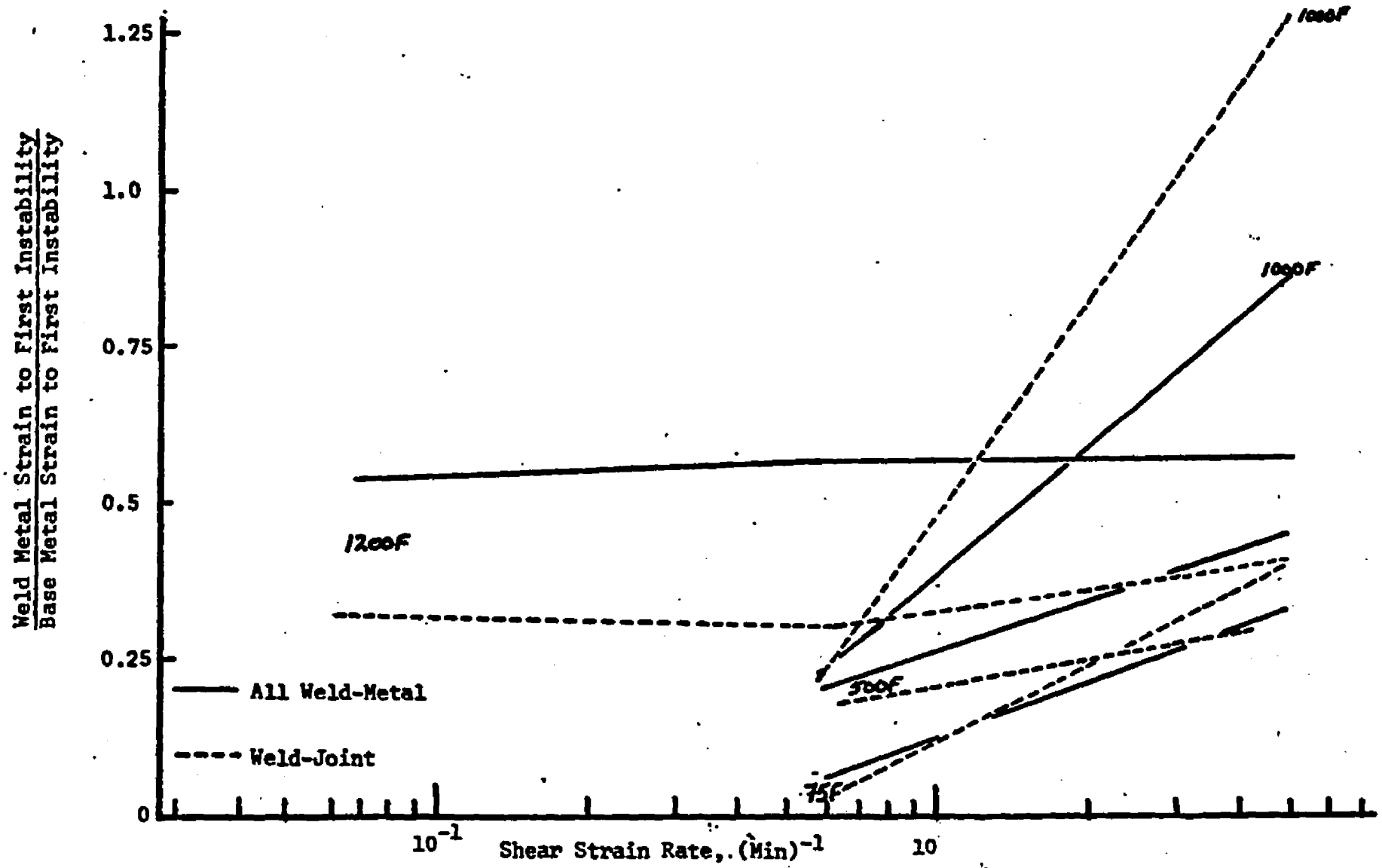

Figure 35. Ratio of Weld-Metal Strain to First Instability to Base-Metal Strain to First Instability as a Function of Strain-Rate at the Indicated Temperatures.

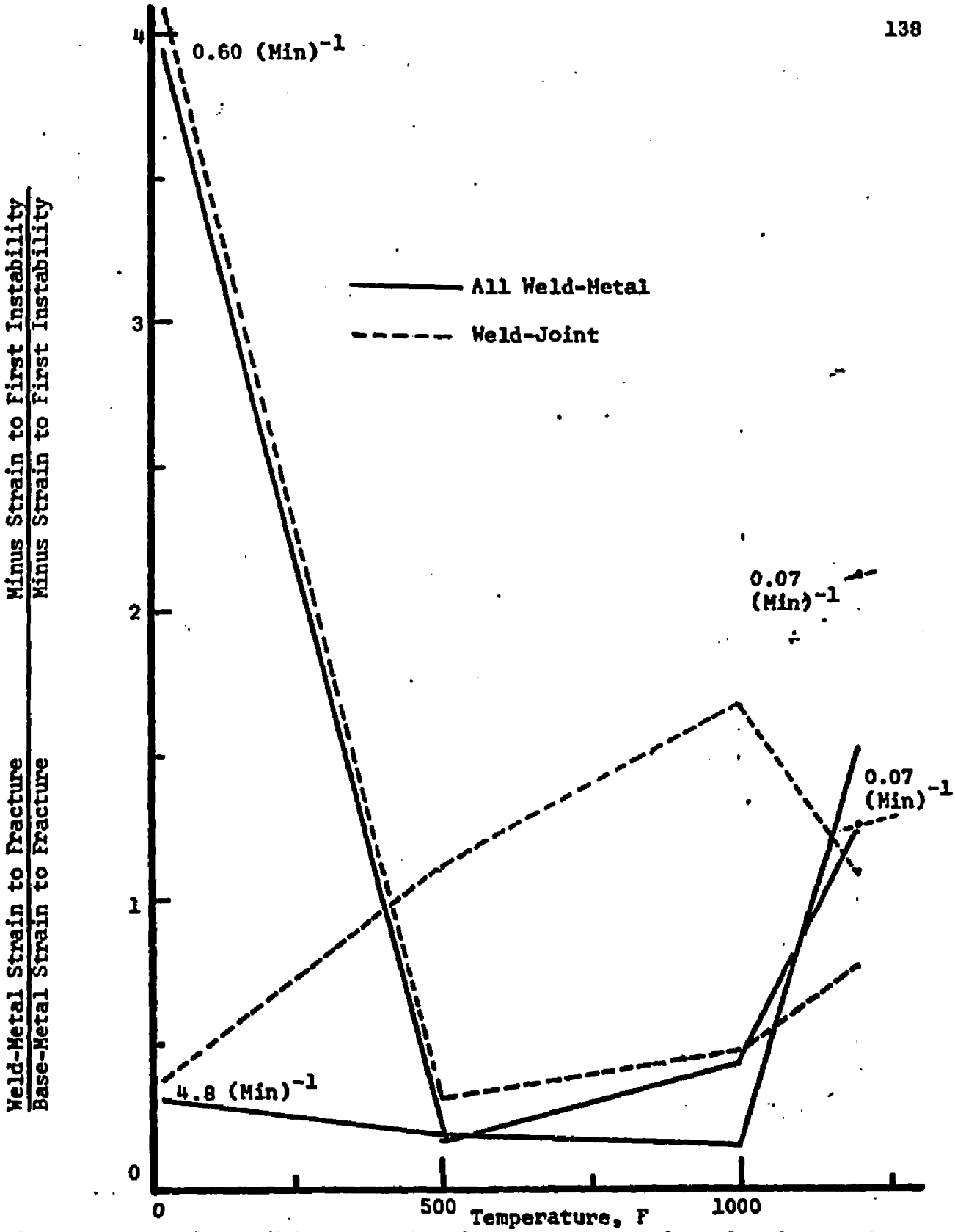

Figure 36.. Ratio of Weld-Metal Strain to Fracture Minus Strain to First Instability to Base-Metal Strain to Fracture Minus Strain to First Instability versus Temperature at Indicated Nominal Strain-Rates for Welded Specimens.

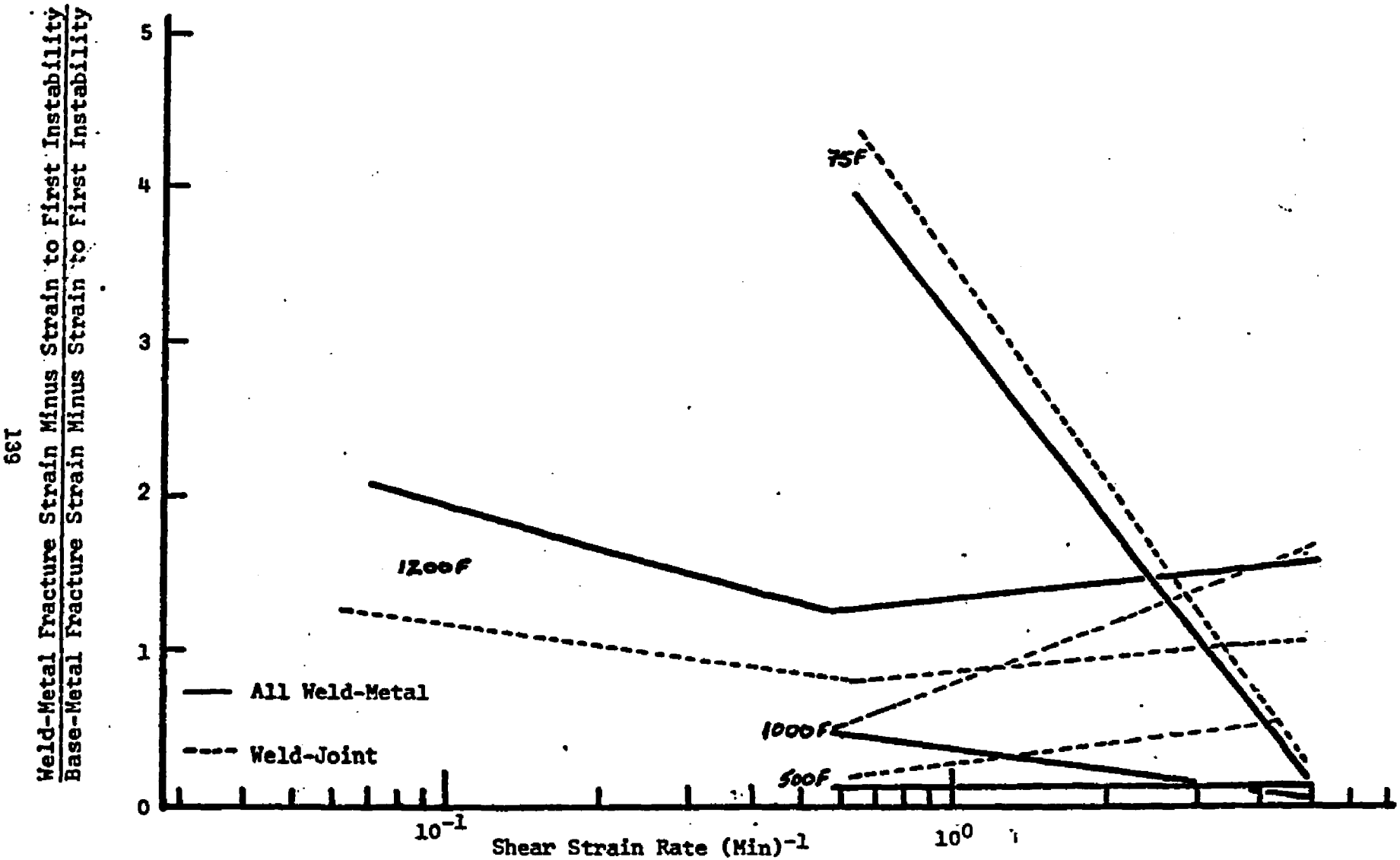

Figure 37. Ratio of Weld-Metal Strain to Fracture Minus Strain to First Instability to Base-Metal Strain to Fracture Minus Strain to First Instability versus Strain-Rate at the Indicated Temperatures.

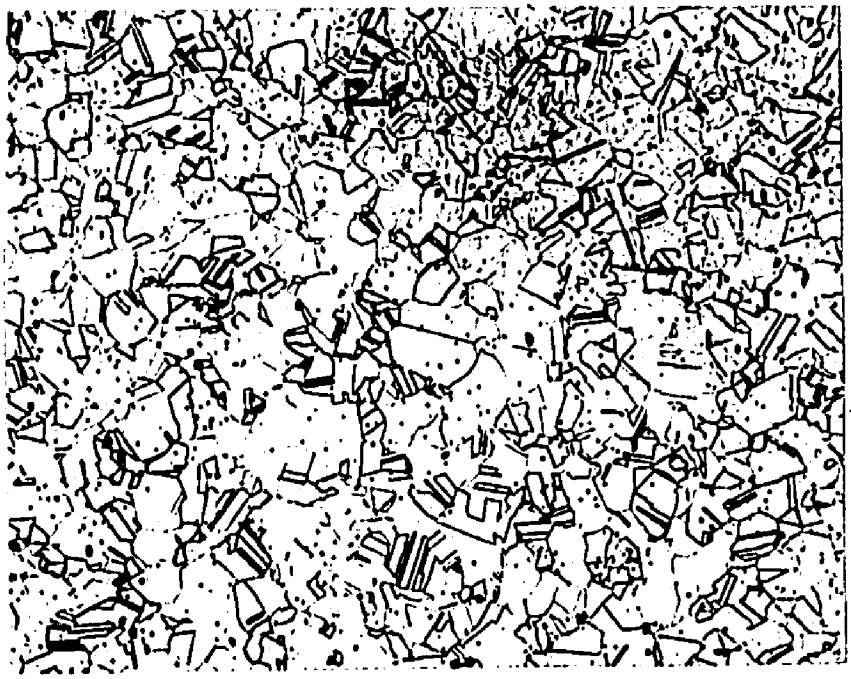

Figure 38. Glyceregia X100

Sample 4AO Transverse section through solution-annealed Type 304 stainless steel bar.

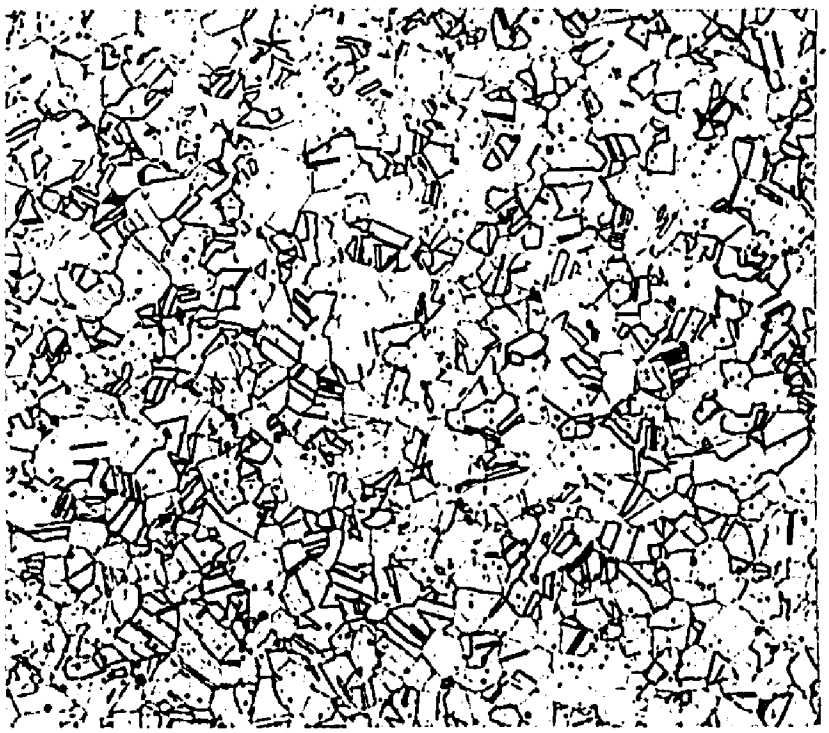

Figure 39. Glyceregia X100

Sample 4AOS Transverse section through solution-annealed and sensitized (1200°F--24 hours--water quench) Type 304 stainless steel bar.

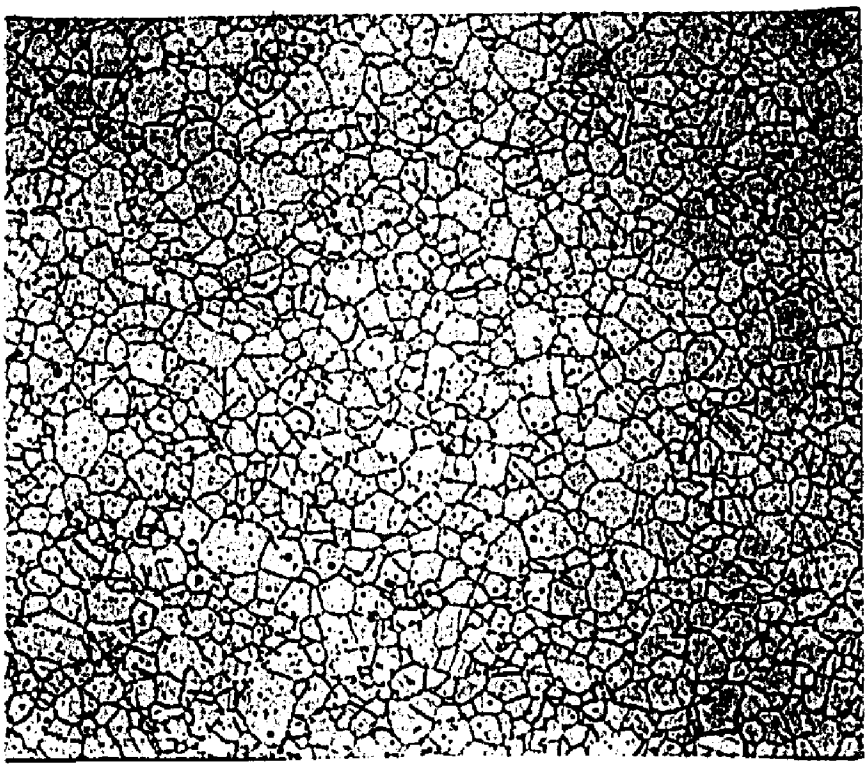

Figure 40. Oxalic Acid X100X

Sample 4AOS Transverse section through solution-annealed and sensitized (1200°F--24 hours--water quench) Type 304 stainless steel bar. Note outlining of grain-boundary carbide envelopes.

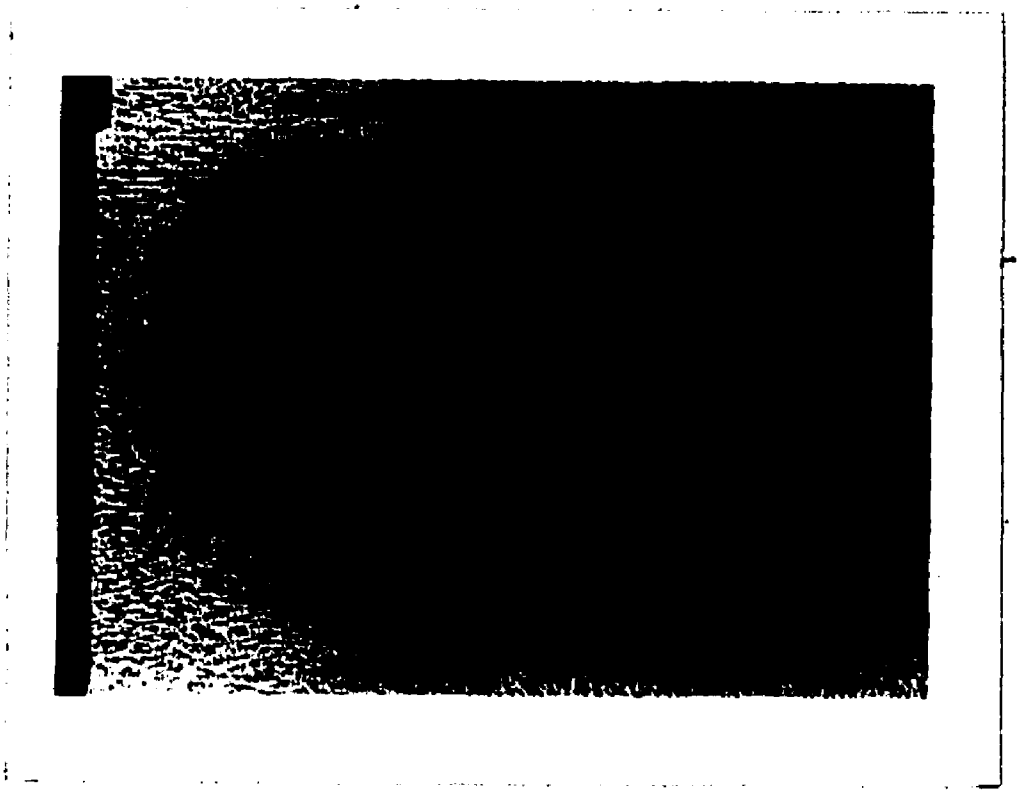

Figure 41. Glyceregia X125

Sample 0 Transverse section through as-deposited manual metal-arc weld in Type 304 stainless steel plate showing coarse as-deposited weld-metal (right) and finer-grained weld-metal after homogenization by re-heating by deposition of succeeding weld-passes (left).

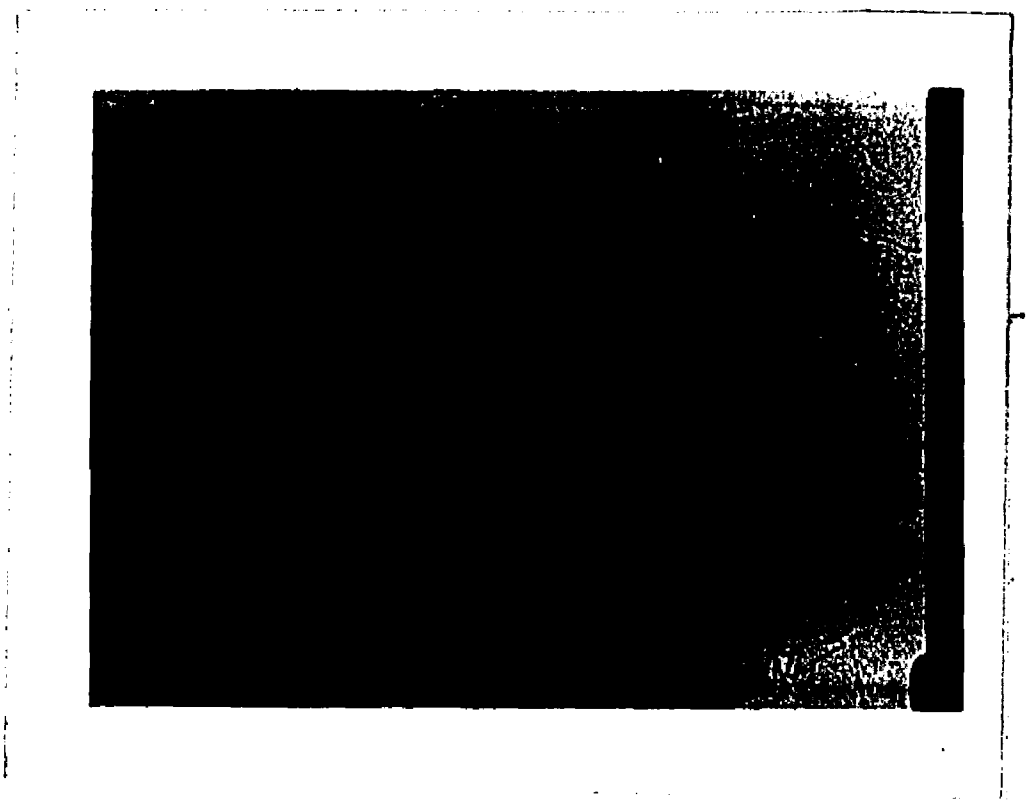

Figure 42. Oxalic Acid X125

Sample O Transverse section through heat-affected zone of manual metal-arc welded Type 304 stainless-steel plate. Note laminations associated with large inclusions (A) and long, narrow, stringer-type inclusion (B).

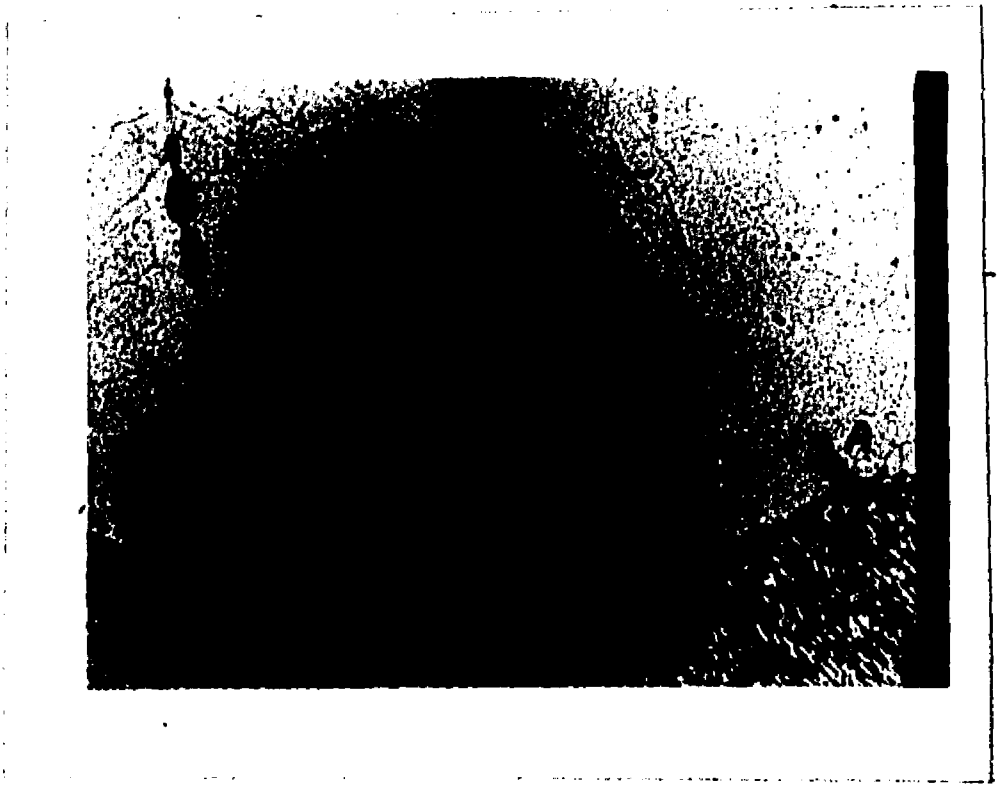

Figure 43. Glyceregia X125

Sample O Transverse section through as-deposited manual metal-arc weld in Type 304 stainless steel plate showing fusion-line hot-tear (A) and semi-continuous series of laminations in heat-affected-zone leading to a tight heat-affected-zone crack (B).

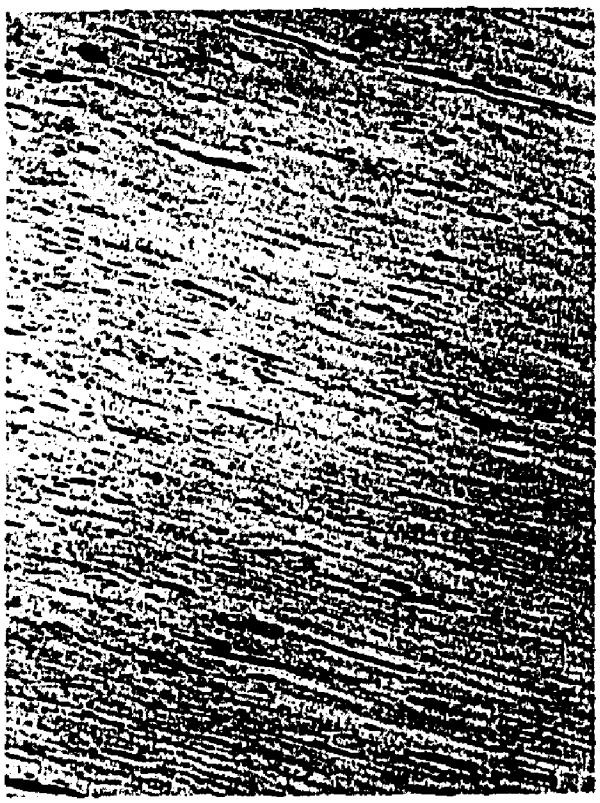

Figure 44. Glyceregia X125

Sample A19 (75°F--4.25 per minute) Interior of sample showing rotation of grains from original bar-axis (horizontal).

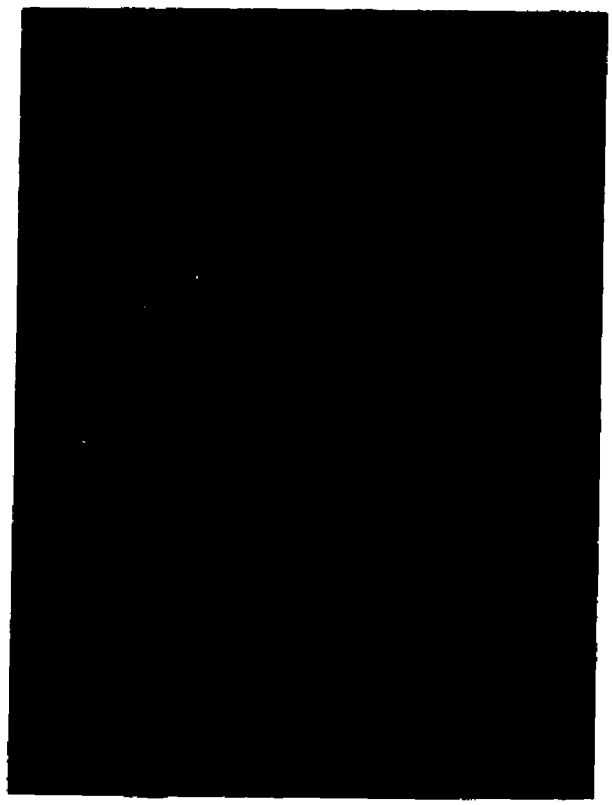

Figure 45. Glyceregia X600

Sample A19 (75°F--4.25 per minute) Interior of sample showing formation of internal cracks associated with inclusions.

Figure 46. Unetched X125

Sample A21 (75°F--0.6 per minute) Secondary crack just behind fracture. Note linking up of pores ahead of crack (A), scattered pores found throughout sample, and change in fiber-orientation due to torsional deformation from vertical (along bar axis) to nearly horizontal.

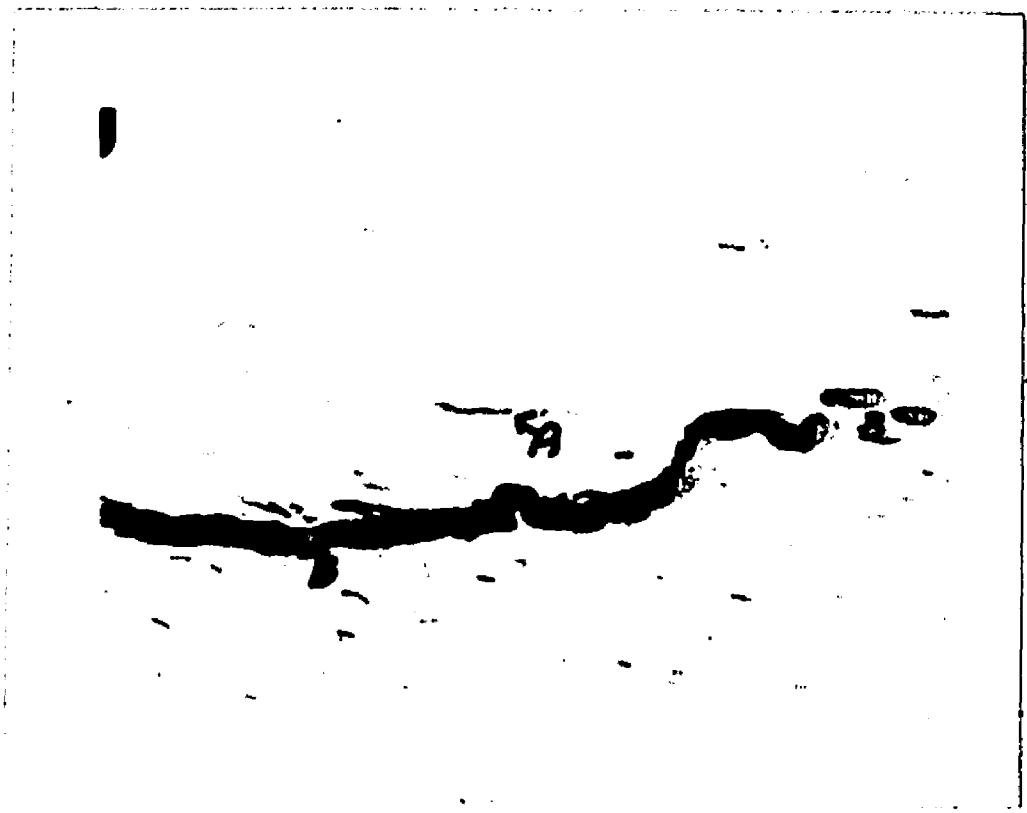

Figure 47. Unetched X600

Sample A21 (75°F--0.6 per minute) Enlargement of growing end of secondary crack shown in Figure 46. Note association of smaller cracks (A) and inclusions (B) with growth of large crack.

Figure 48. Glyceregia X600

Sample A19 (75°F--4.25 per minute) Details of fracture-surface, showing extreme rotation of grains and inclusions from original bar-axis (horizontal) and growth of a secondary crack (A) in from the fracture-surface.

Figure 49. Glyceregia X1500

Sample A19 (75°F--4.25 per minute) Enlargement of region shown in Figure 48, showing growth of secondary crack by formation and coalesence of pores (A) ahead of the advancing crack.

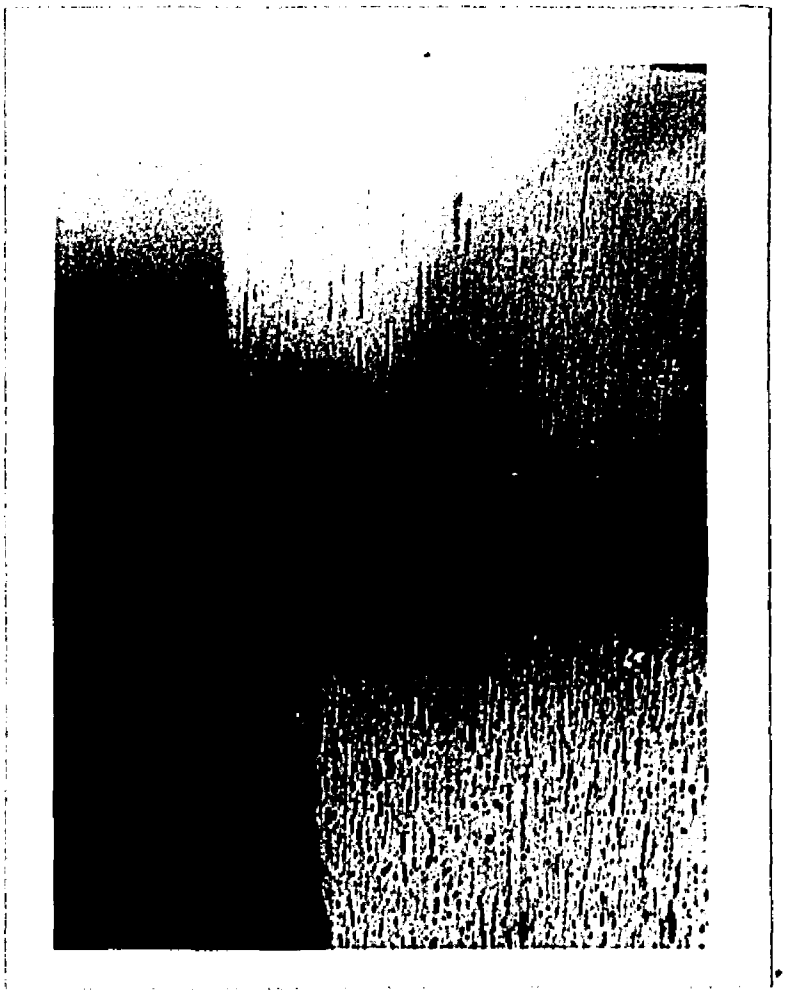

Figure 50. Glyceregia X125

Sample A4 (500°F--0.62 per minute) Details of fracture-surface showing extreme rotation of grains and inclusions from original bar-axis (horizontal).

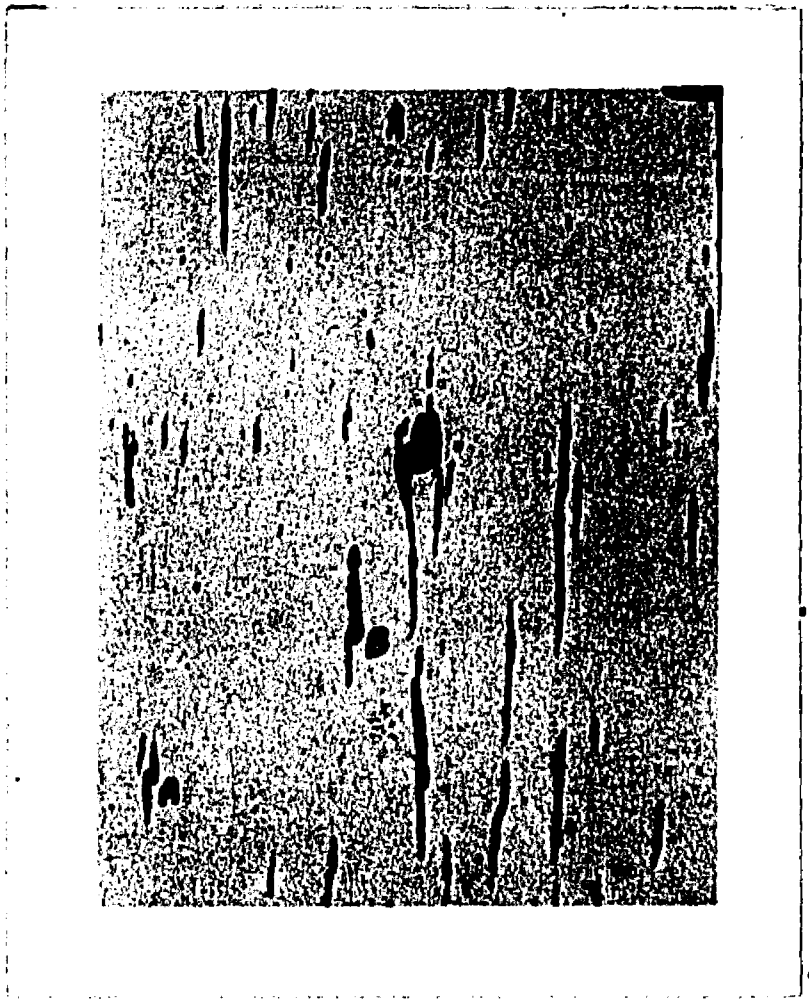

Figure 51. Glyceregia X600

Sample A4 (500°F--0.62 per minute) Microstructure just behind fracture-surface. Note decohesions at inclusion: matrix interfaces (A), and propagation of a crack towards a smaller inclusion with its associated pair of cracks (B).

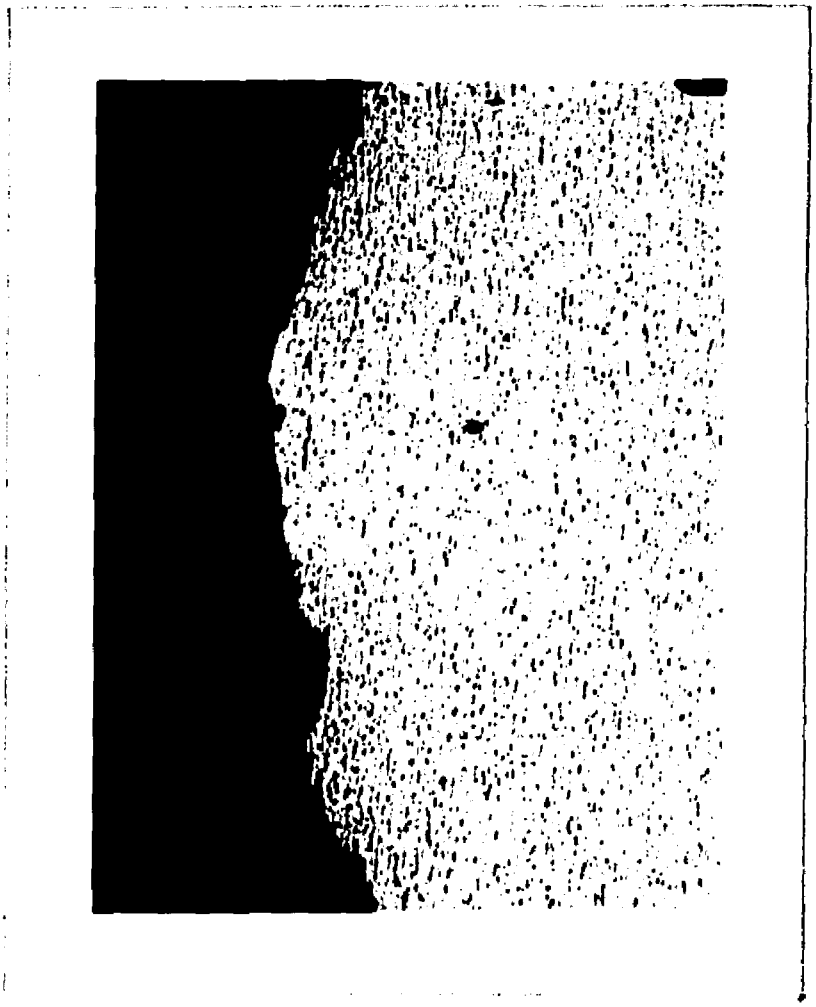

Figure 52. Glyceregia X125

Sample A14 (500°F--0.0634 per minute) Details of fracture-surface showing extreme rotation of grains and inclusions from original bar-axis (horizontal).

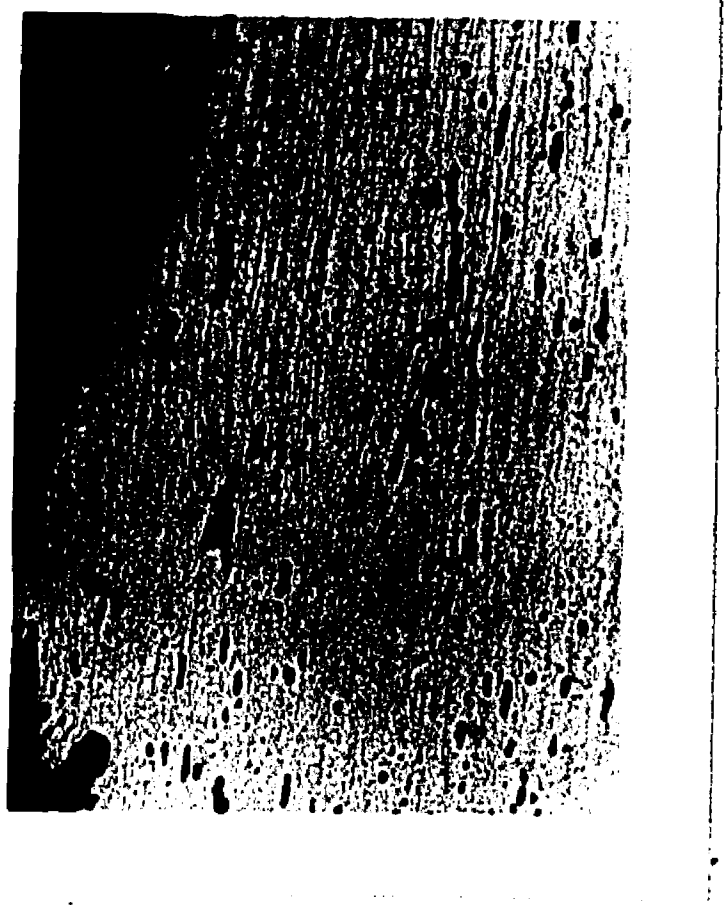

Figure 53. Glyceregia X600

Sample A14 (500°F--0.0634 per minute) Microstructure just behind fracture-surface showing growth of two secondary cracks by tearing of the material between them.

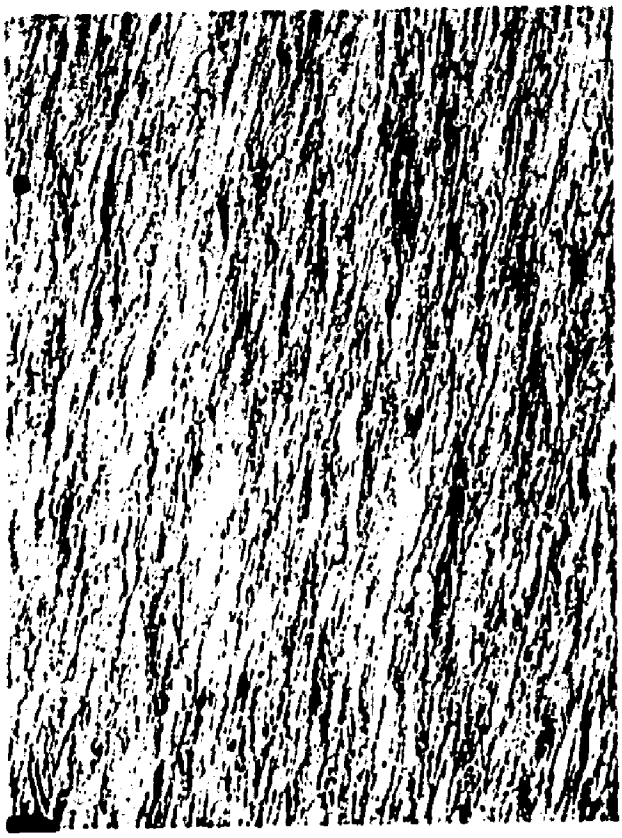

Figure 54. Glyceregia X125

Sample A11 (1000°F--4.72 per minute) Microstructure just behind fracture surface showing extreme rotation of grains and inclusions from original bar-axis (horizontal) by torsional deformation.

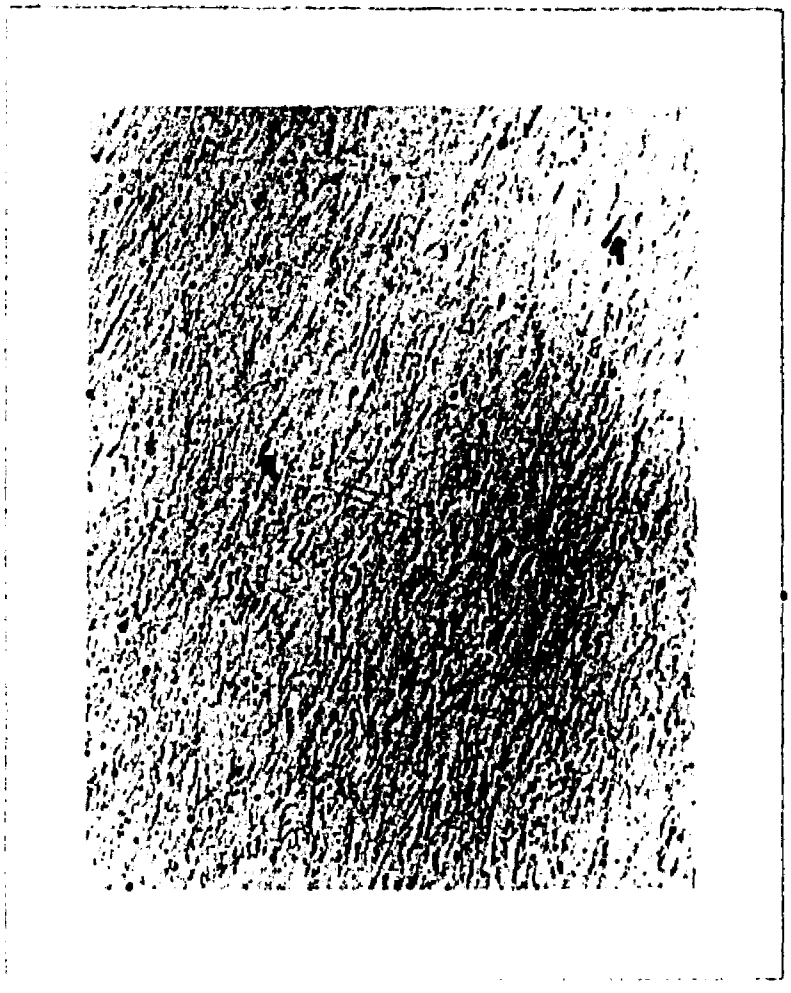

Figure 55. Glyceregia X125

Sample A11 (1900°F--4.72 per minute) Microstructure far from fracture-surface. Note secondary crack emanating from inclusion: matrix interface.

Figure 56. Glyceregia X600

Sample A11 (1000°F--4.72 per minute) Enlargement of Figure 55 showing crack emanating from inclusion: matrix interface (A) and from an inclusion in a carbide-free grain-boundary (B)

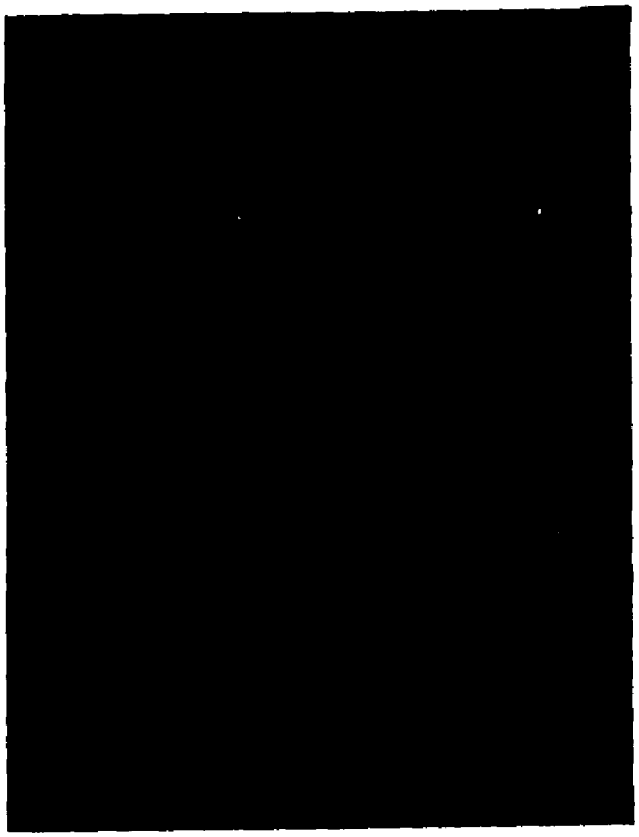

Figure 57. Glyceregia X1500

Sample All (1000°F--4.72 per minute) Enlargement of Figure 56. Note propagation of crack through a small group of inclusions.

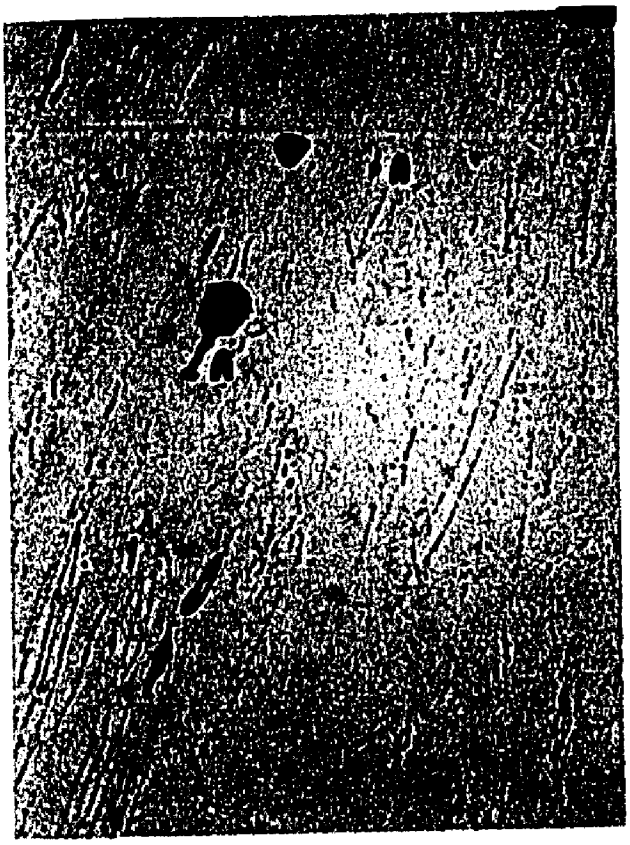

Figure 58. Glyceregia X600

Sample A11 (1000°F--4.72 per minute) Enlargement of Figure 55 showing cracks growing from inclusion: matrix interfaces (A).

Figure 59. Glyceregia X125

Sample A18 (1200°F--0.073 per minute) Secondary cracks behind fracture surface showing localization of plastic-flow between two growing cracks, and extreme rotation of grains and inclusions from original bar-axis (horizontal) by torsional deformation.

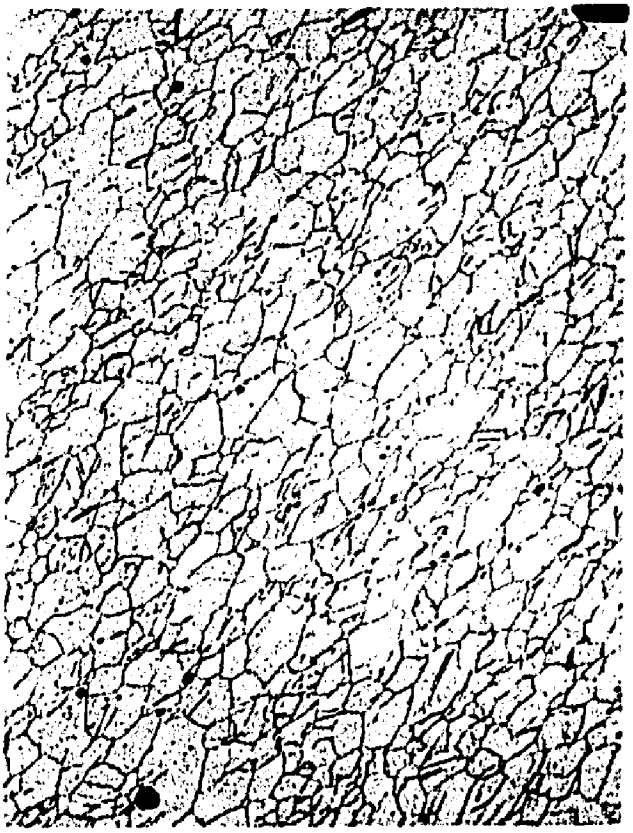

Figure 60. Glyceregia X125

Sample A18 (1200°F--0.073 per minute) Microstructure far from fracture surface. Compare with Figure 59 and note relatively undeformed microstructure.

Figure 61. Oxalic Acid X600

Sample A18 (1200°F--0.073 per minute) Enlargement of end of crack shown in Figure 59 showing transgranular growth of crack and precipitation of carbides on grain-boundaries and within the grains during heating to and testing at 1000°F.

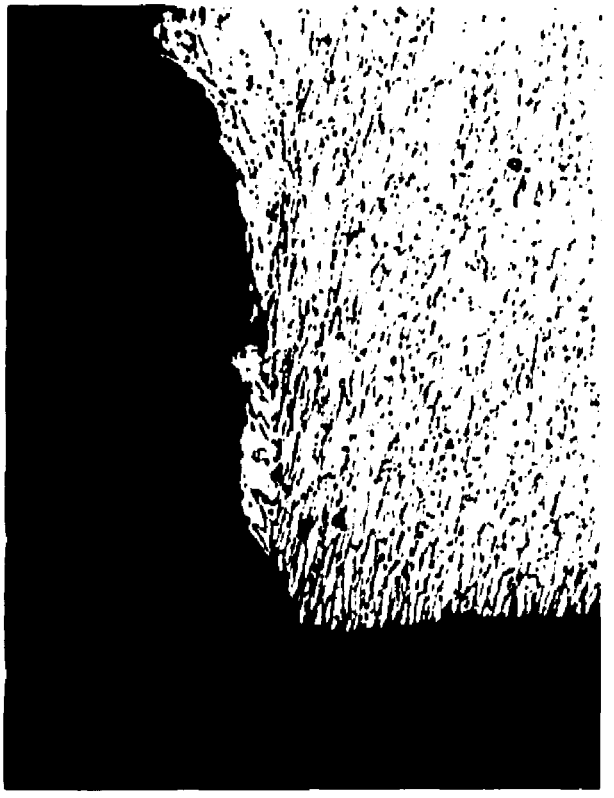

Figure 62. Oxalic Acid X125

Sample AS17 (75°F--2.34 per minute) Microstructure at fracture-surface, showing extreme rotation of grains from original bar-axis.

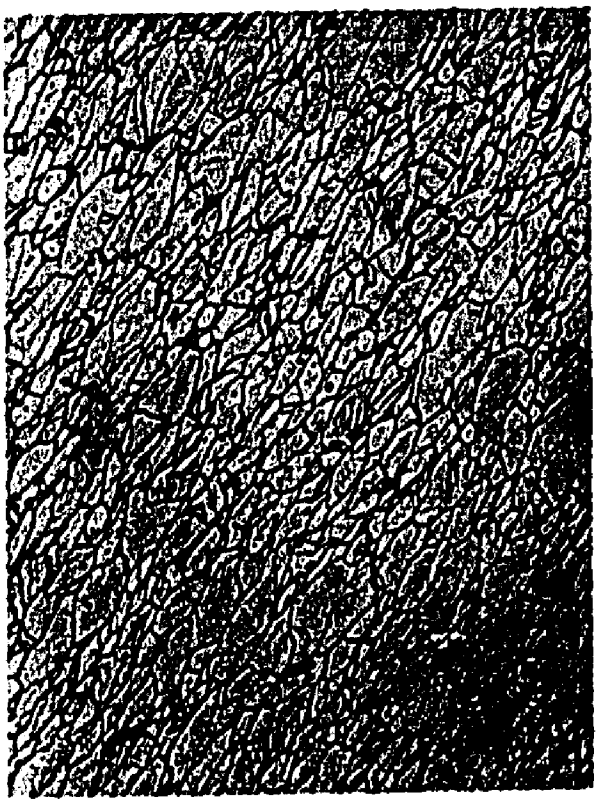

Figure 63. Oxalic Acid X125

Sample AS17 (75°F--2.34 per minute) Microstructure far from fracture-surface illustrating moderate deformation of grains (compare with Figure 62).

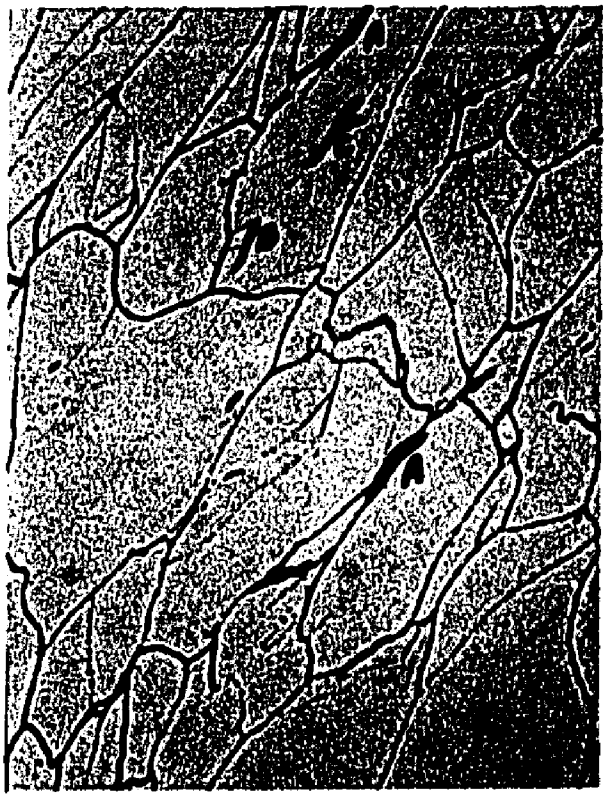

Figure 64. Oxalic Acid X600

Sample AS17 (75°F--2.34 per minute) Crack-propagation associated with second-phases in grain-boundaries (A), twin-boundaries (B) and within the grains (C).

Figure 65. Oxalic Acid X1500

Sample AS17 (75°F--2.34 per minute) Enlargement of Figure 64, showing the development of a crack growing from an inclusion (A) in the interior of a grain towards a nearby second-phase particle (B).

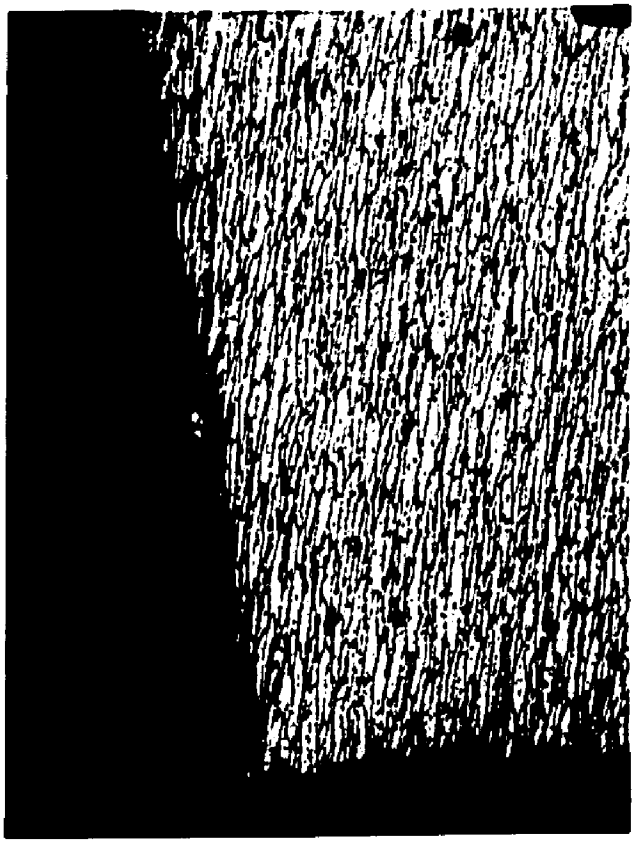

Figure 66. Oxalic Acid X125

Sample AS11 (500°F--0.065 per minute) Fracture-surface, showing extreme rotation of grains and inclusions from original bar-axis (horizontal).

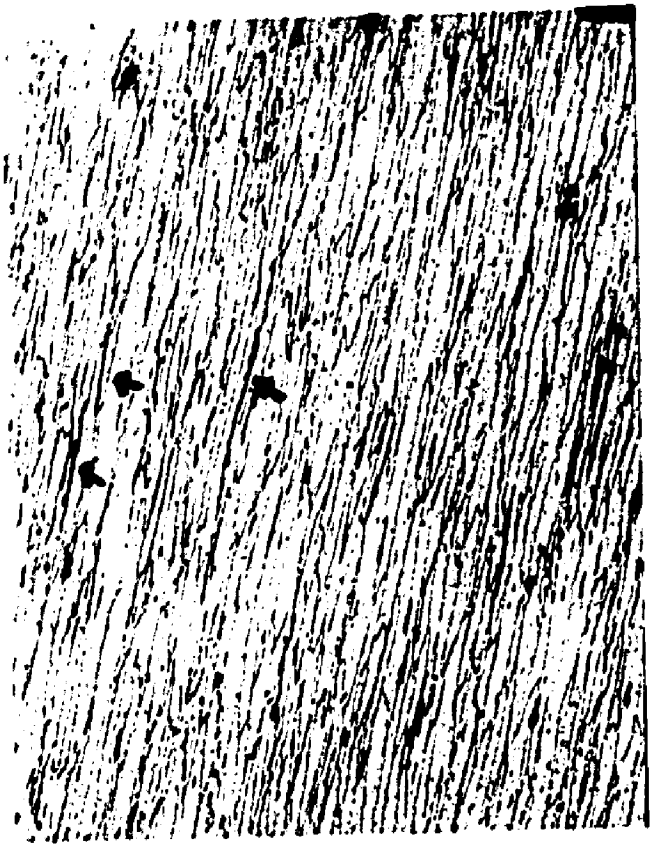

Figure 67. Oxalic Acid X125

Sample AS11 (500°F--0.065 per minute) Microstructure far from fracture-surface, showing secondary cracks along grain-boundaries.

Figure 68. Oxalic Acid X125

Sample AS11 (500°F--0.065 per minute) Microstructure near center-line of bar far from fracture-surface.

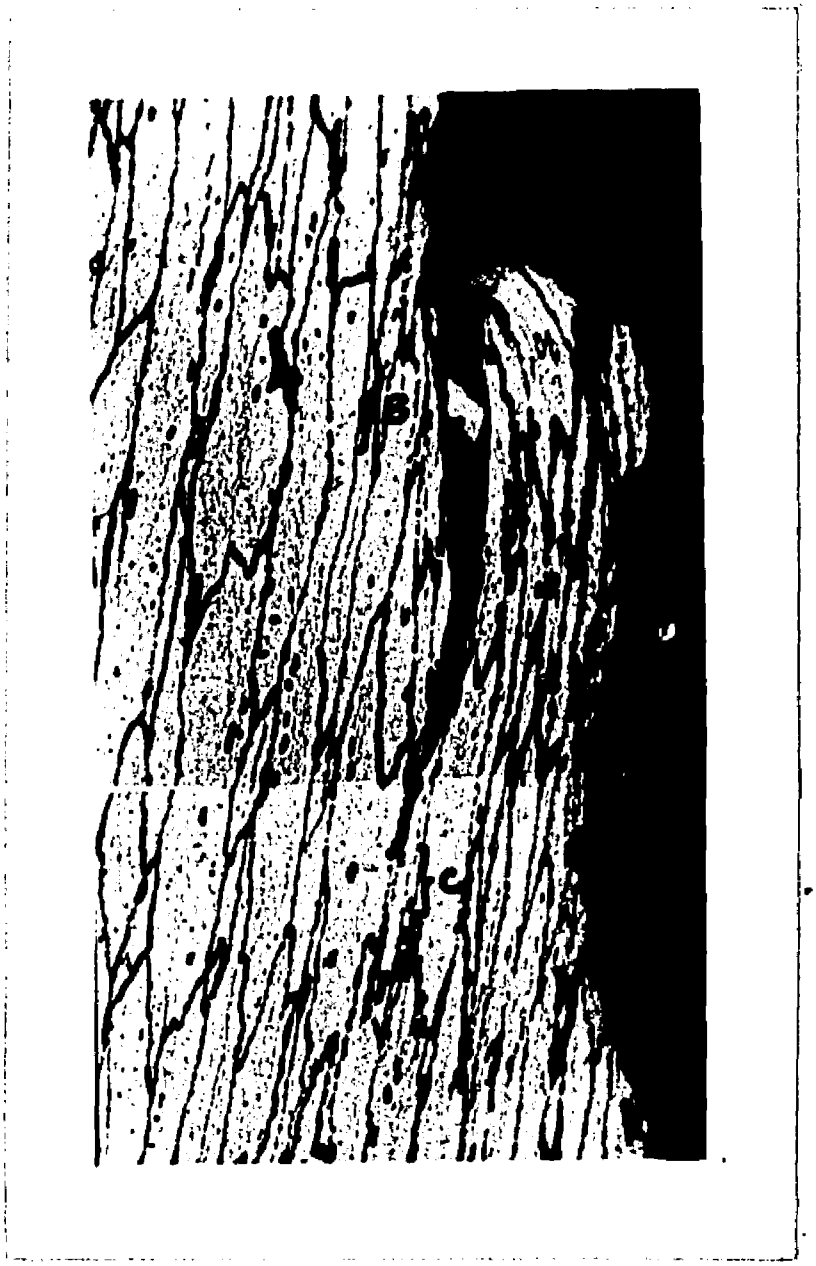

Figure 69. Oxalic Acid X600

Sample AS11 (500°F--0.065 per minute) Secondary crack, showing pore-formation in intergranular carbide networks (A), their growth into intergranular cracks (B), and crack-growth by localization of plastic flow between crack-tip and nearby array of pores (C).

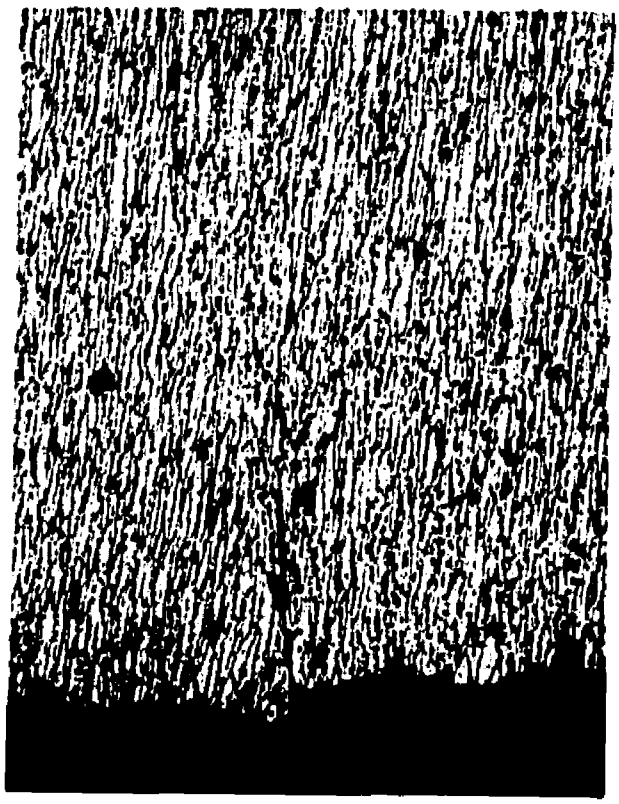

Figure 70. Oxalic Acid X125

Sample AS3 (500°F--2.64 per minute) Microstructure just behind fracture-surface, illustrating extreme rotation of grains and inclusion from original bar-axis (horizontal) by torsional deformation and a secondary crack (A).

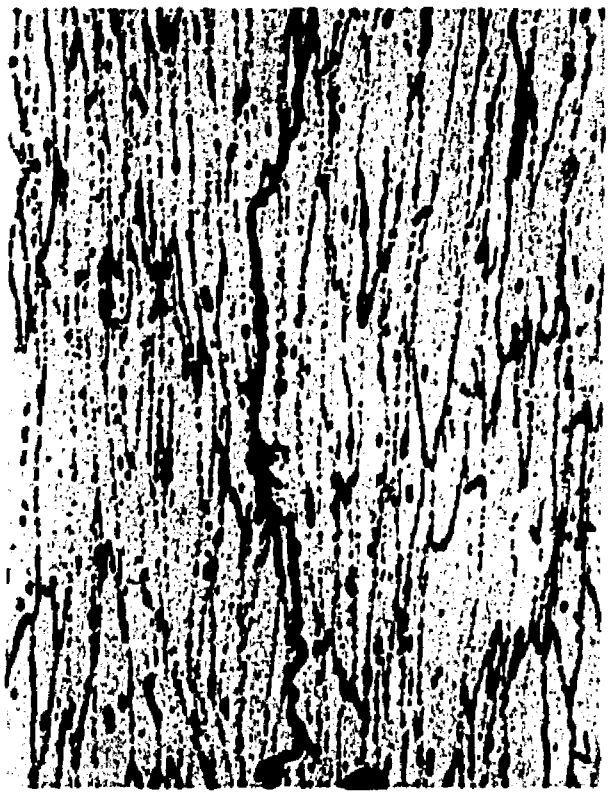

Figure 71. Oxalic Acid X600

Sample AS3 (500°F--2.64 per minute) Enlargement of growing end of secondary crack in Figure 70, showing partially intergranular-partially transgranular propagation of crack.

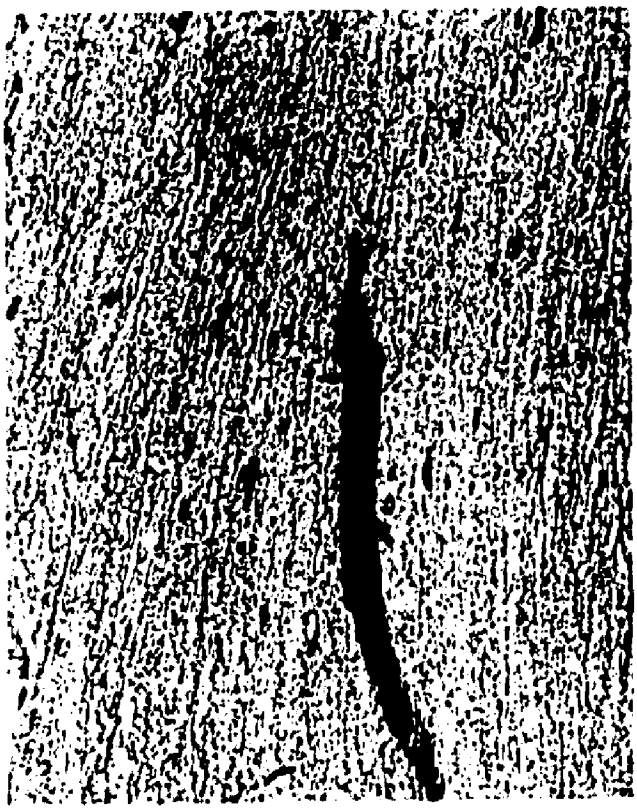

Figure 72. Oxalic Acid X600

Sample AS8 (1000°F--4.81 per minute) Secondary crack behind and parallel to the fracture-surface.

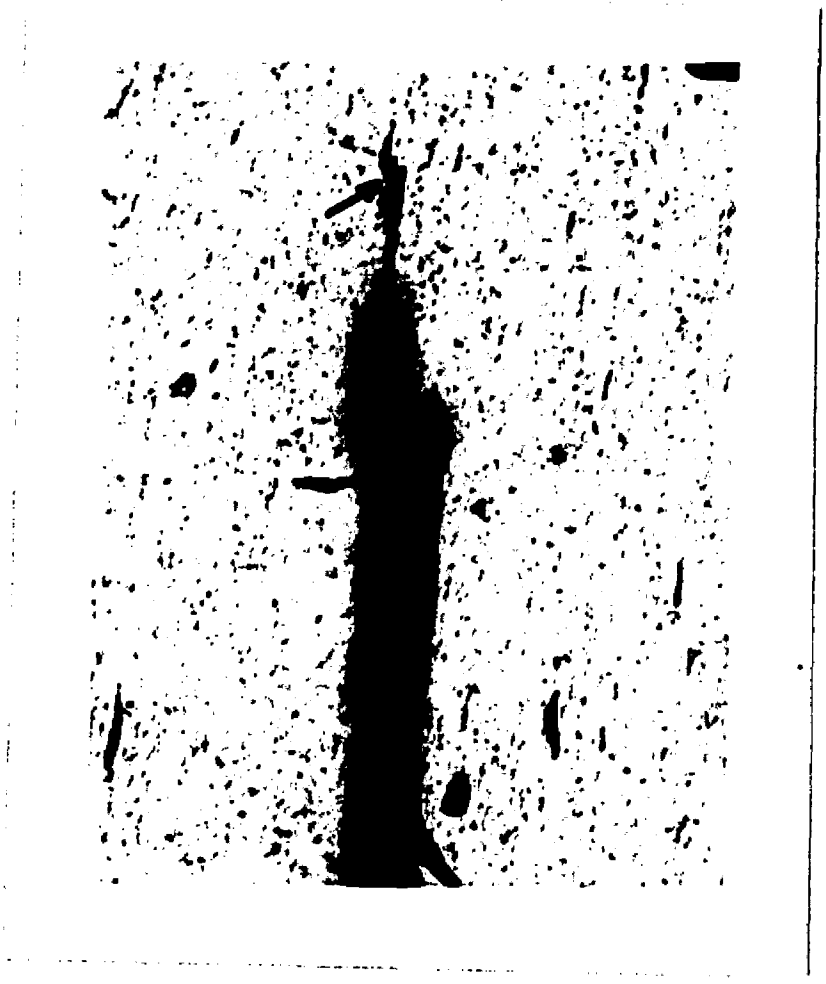

Figure 73. Oxalic Acid X1500

Sample AS8 (1000°F--4.81 per minute) Enlargement of growing end of crack in Figure 72 showing growth past an inclusion by an inclusion: matrix decohesion.

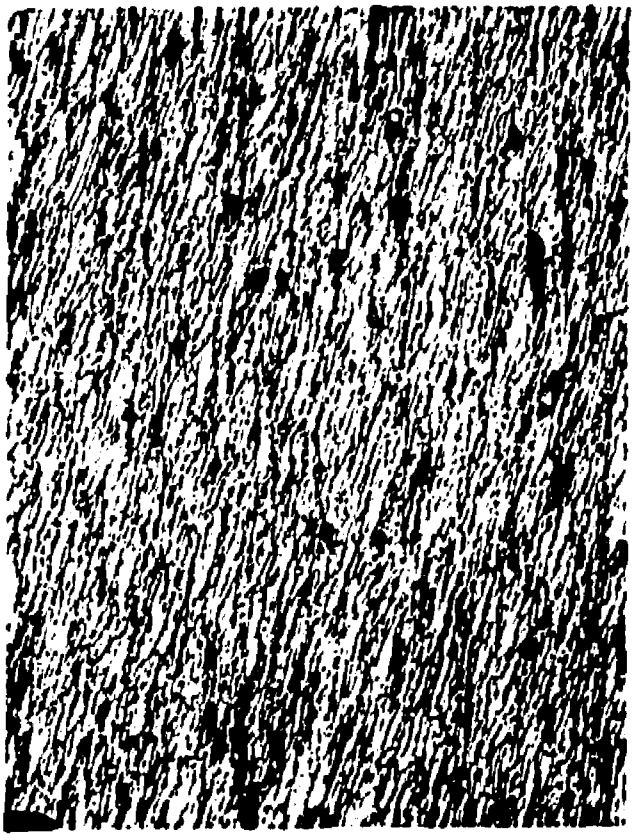

Figure 74. Oxalic Acid X125

Sample AS15 (1200°F--0.0731 per minute) Microstructure just behind fracture-surface showing extreme rotation of grains and inclusions from original bar-axis (horizontal) by torsional deformation.

Figure 75. Oxalic Acid X600

Sample AS15 (1200°F--0.0731 per minute) Microstructure just behind fracture-surface showing growth of a secondary crack along grain-boundary carbide-networks (A) and localization of plastic-flow between two growing cracks (B)

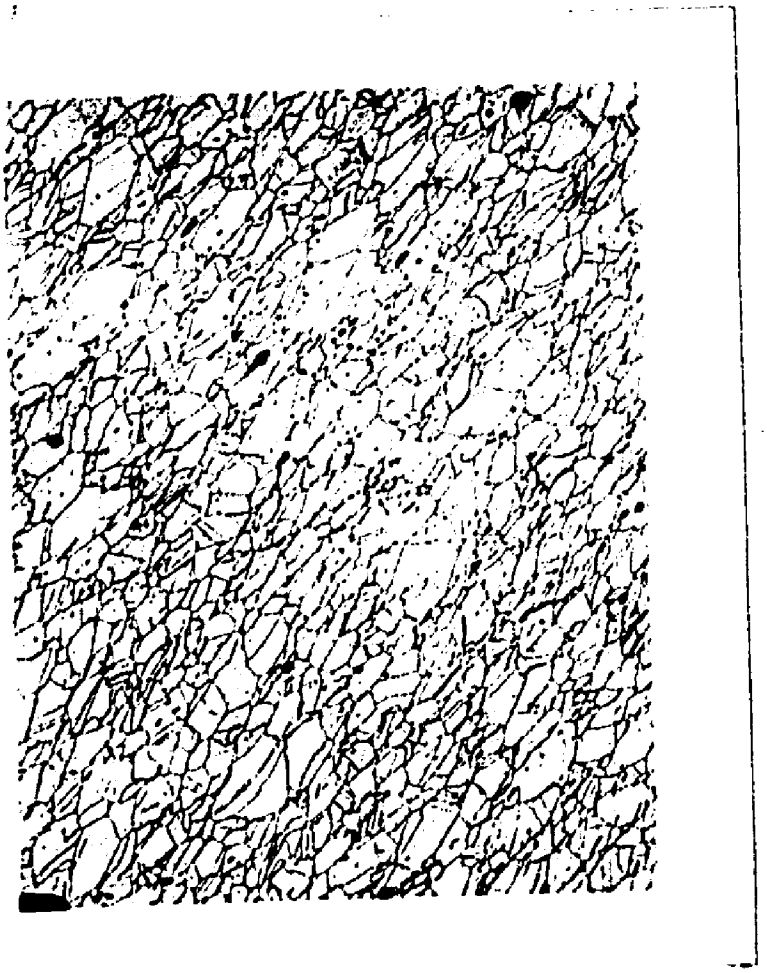

Figure 76. Oxalic Acid X125

Sample AS15 (1200°F--0.0731 per minute) Microstructure far from fracture showing small amount of grain and inclusion rotation from original bar-axis.

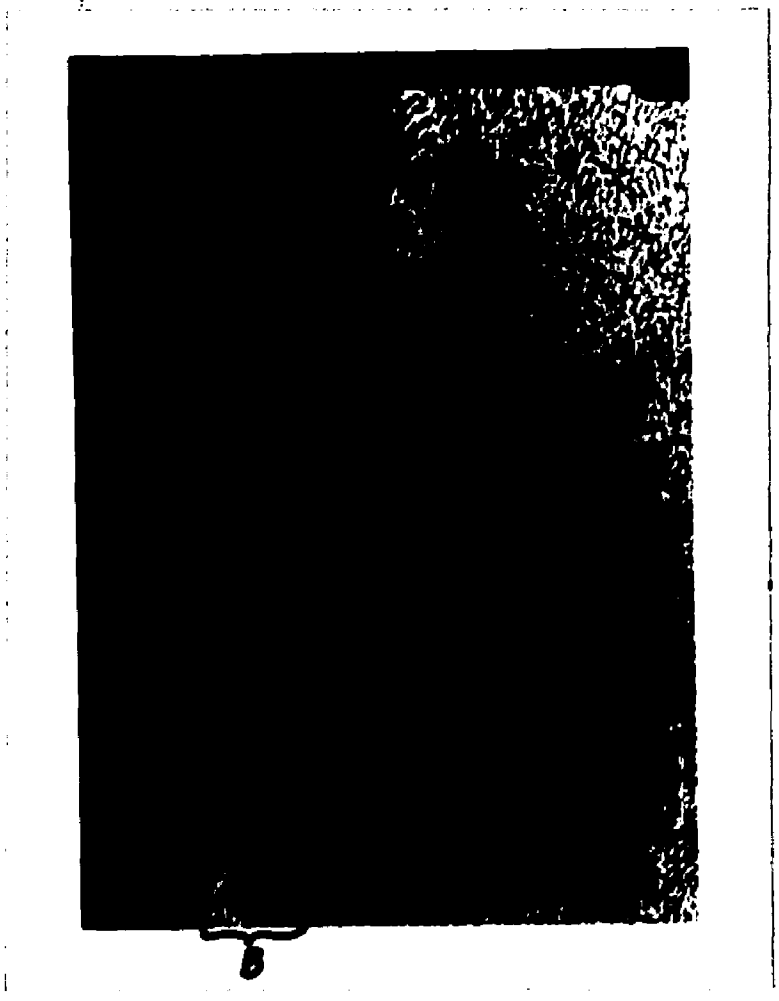

Figure 77. Glyceregia X125

Sample W12 (75°F--0.0688 per minute). Details of fracture surface showing development of a secondary crack at the edge of an instability (A). Note localization of plastic flow within the instability that was associated with fracture (B).

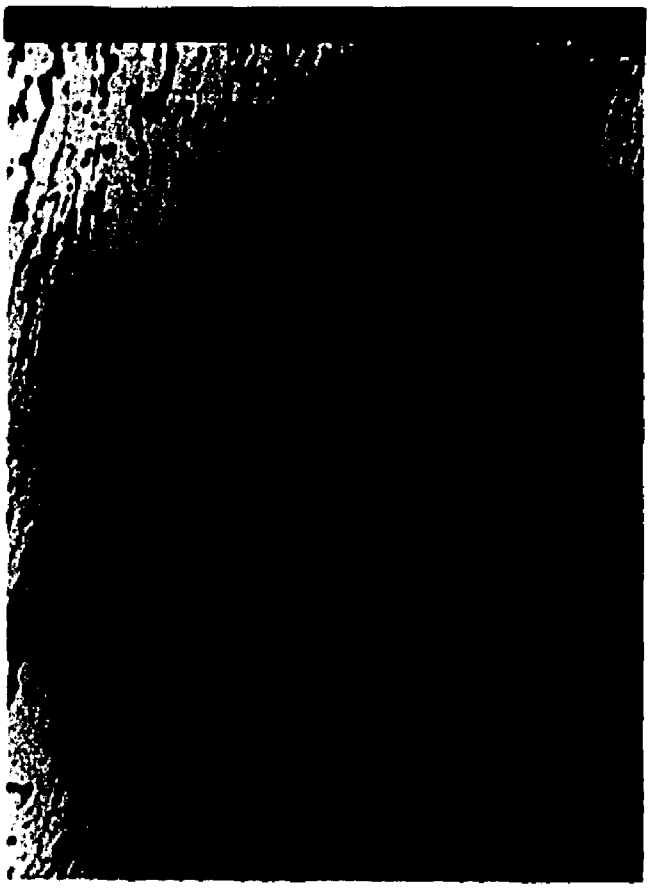

Figure 78. Glyceregia X600

Sample W12 (75°F--0.0688 per minute) Microstructure at the tip of the growing crack shown in Figure 77. Note growth of the crack along interdendritic ferrite networks (A) and presence of pores within ferrite islands ahead of the crack.

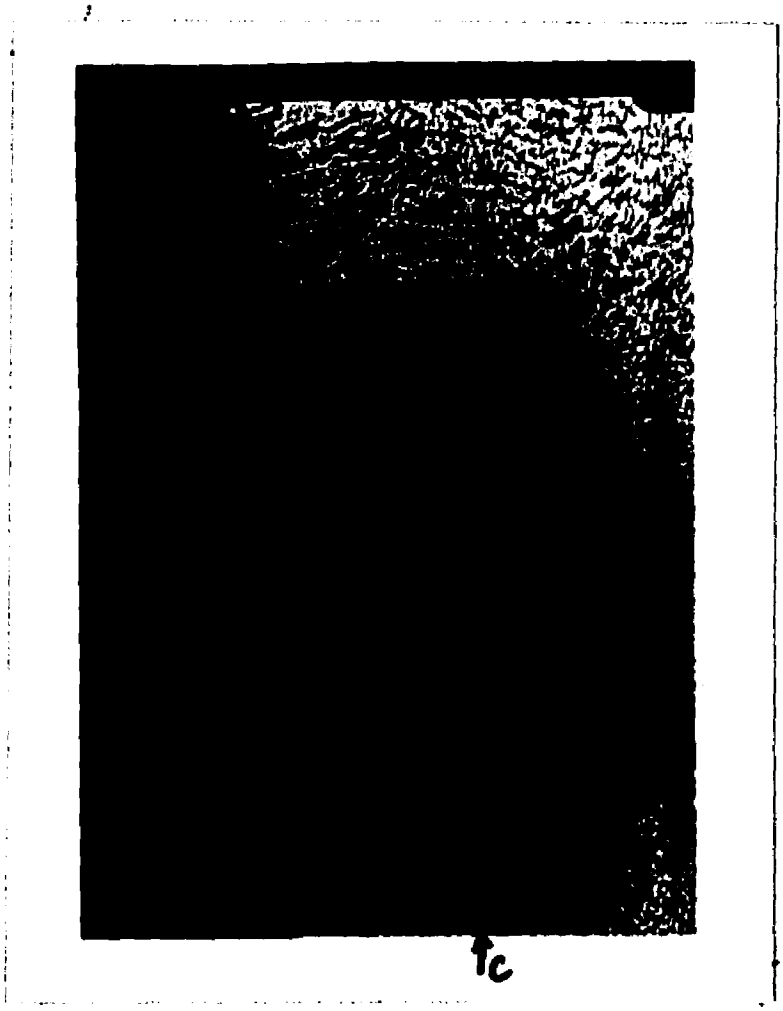

Figure 79. Glyceregia X125

Sample W1 (500°F--4.85 per minute) Fracture surface showing propagation through a region of "as deposited" weld-metal (A) and growth of a secondary crack (B) that stopped just short of the "as deposited: grain-refined" interface (C).

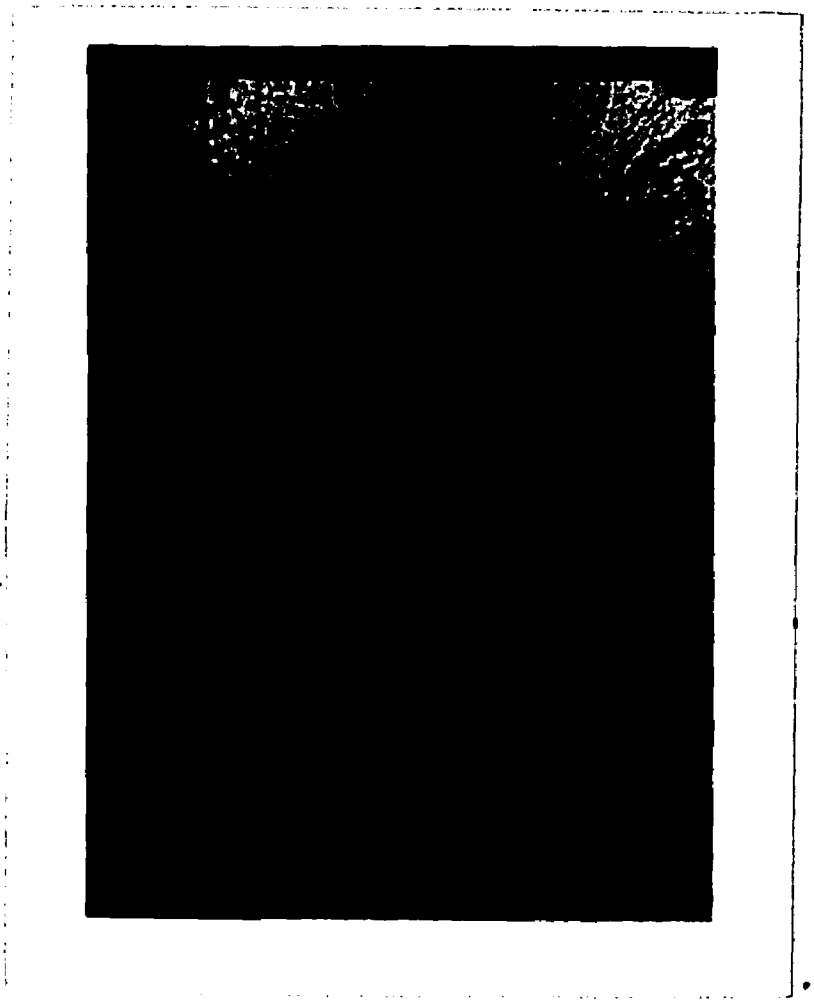

Figure 80. Glyceregia X600

Sample W1 (500°F--4.85 per minute) Enlargement of the secondary crack shown in Figure 79, showing the propagation through interdendritic ferrite (A) and formation of pores (B) in ferrite pools ahead of and around the crack.

Figure 81. Glyceregia X125

Sample W3 (500°F--0.0651 per minute) Fracture surface, showing propagation of fracture through an "as-deposited" region (A) and a "grain-refined" region (B) in the fusion-zone.

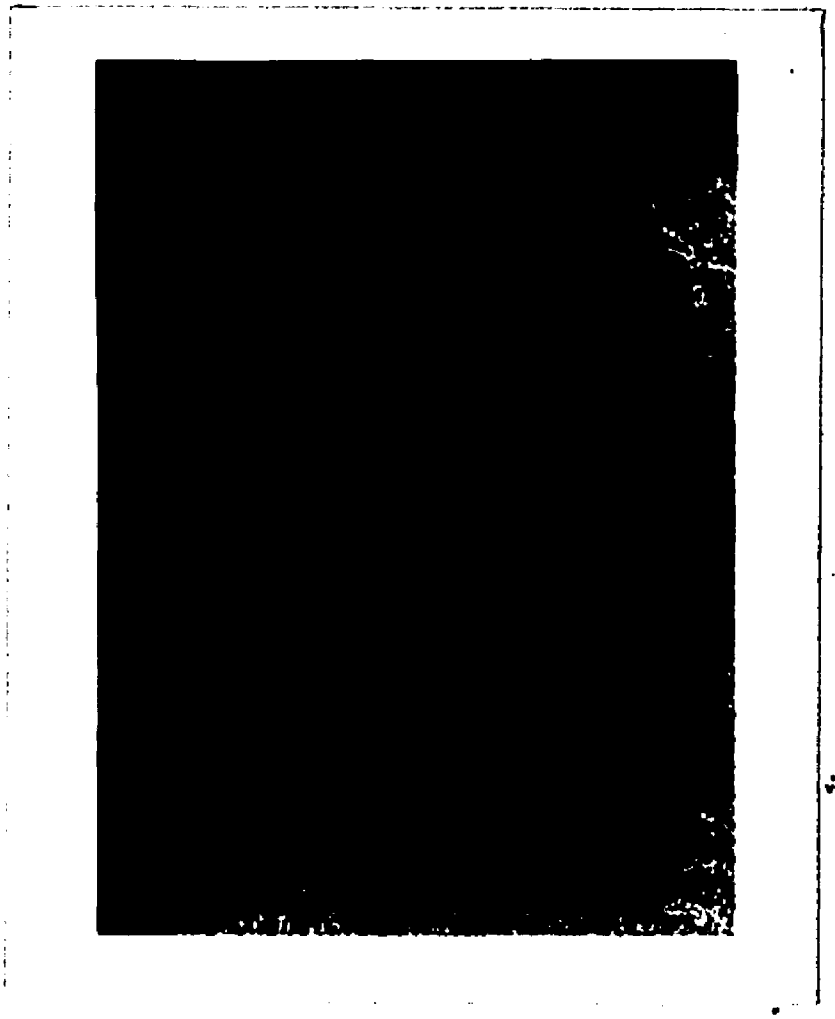

Figure 82. Glyceregia X125

Sample W7 (1200°F--4.80 per minute) Fracture surface showing secondary cracks.

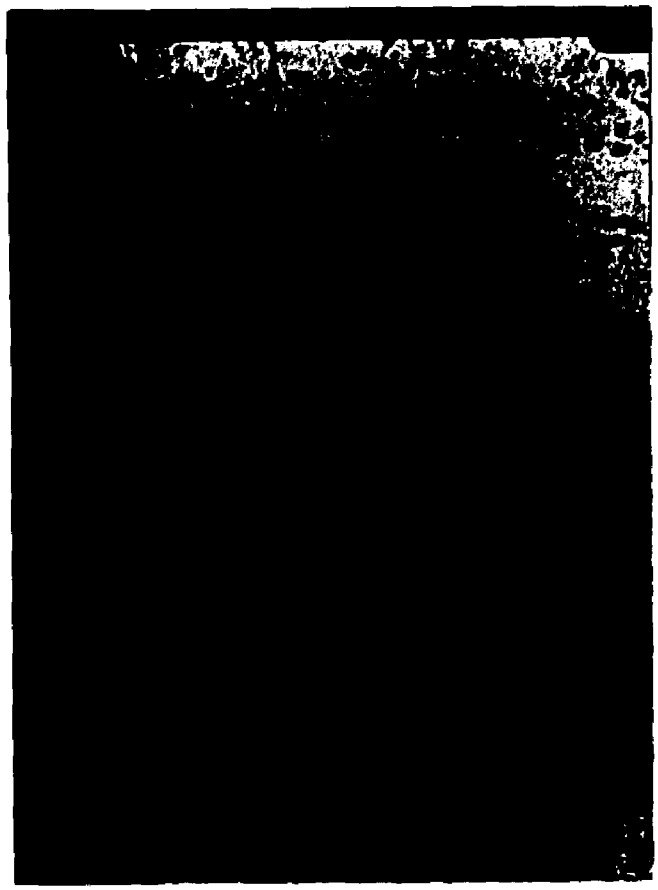

Figure 83. Glyceregia X600

Sample W7 (1200°F--4.80 per minute) Enlargement of fracture surface shown in Figure 82 showing propagation along interdendritic ferrite pools (A).

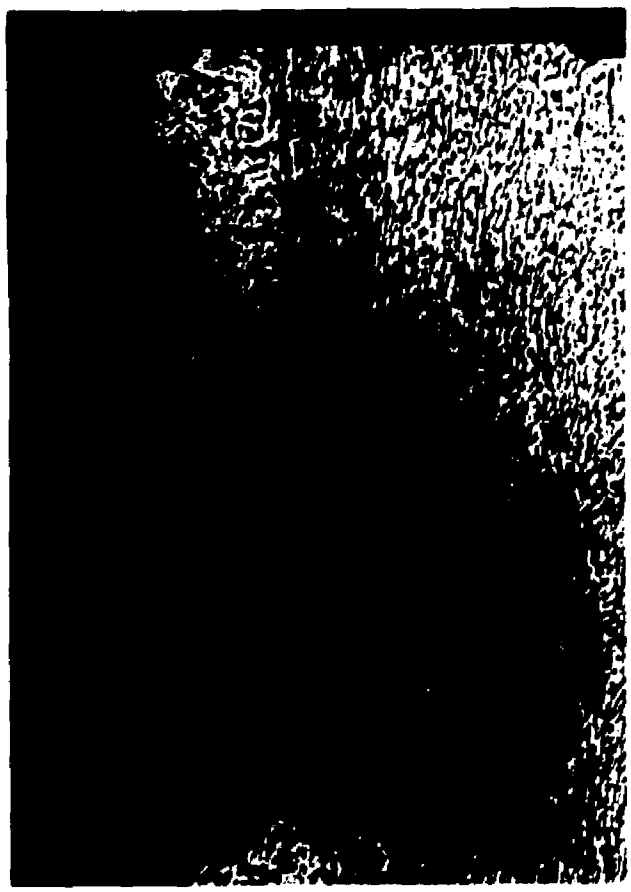

Figure 84. Glyceregia X125

Sample W9 (1200°F--0.580 per minute) Fracture-surface showing a change in orientation of weld-metal just behind fracture-surface.

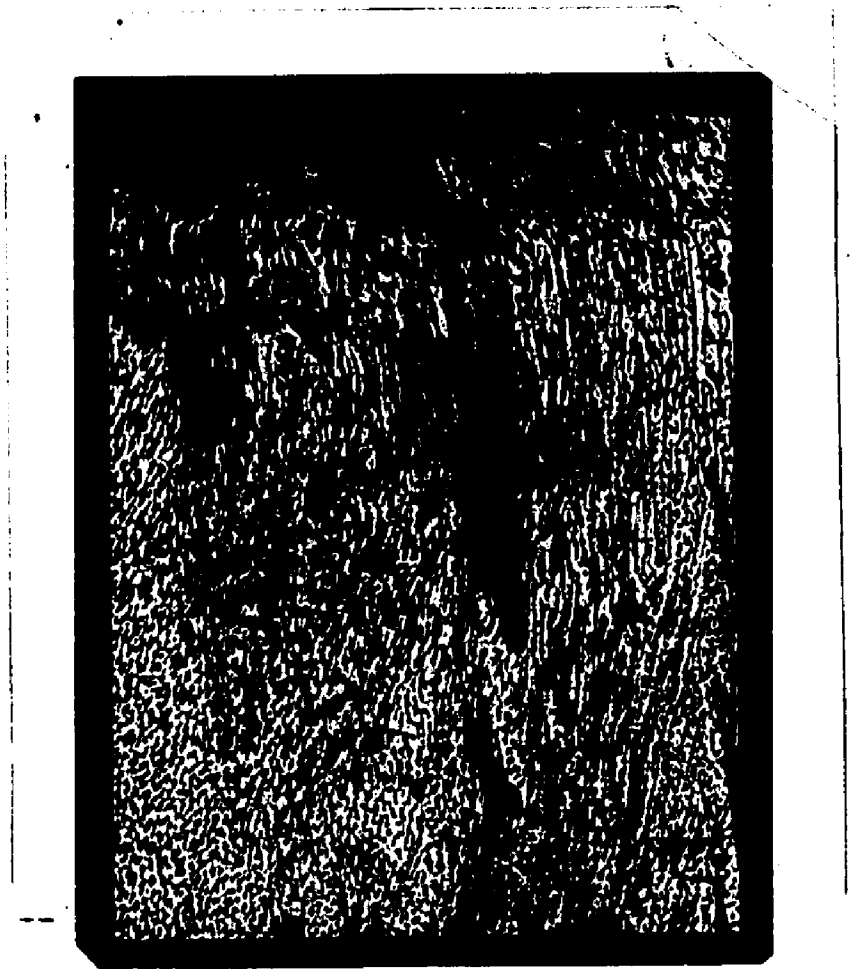

Figure 85. Glyceregia X125

Sample W9 (1200°F--0.580 per minute) Secondary crack (A) about 1/8 inch behind fracture-surface.

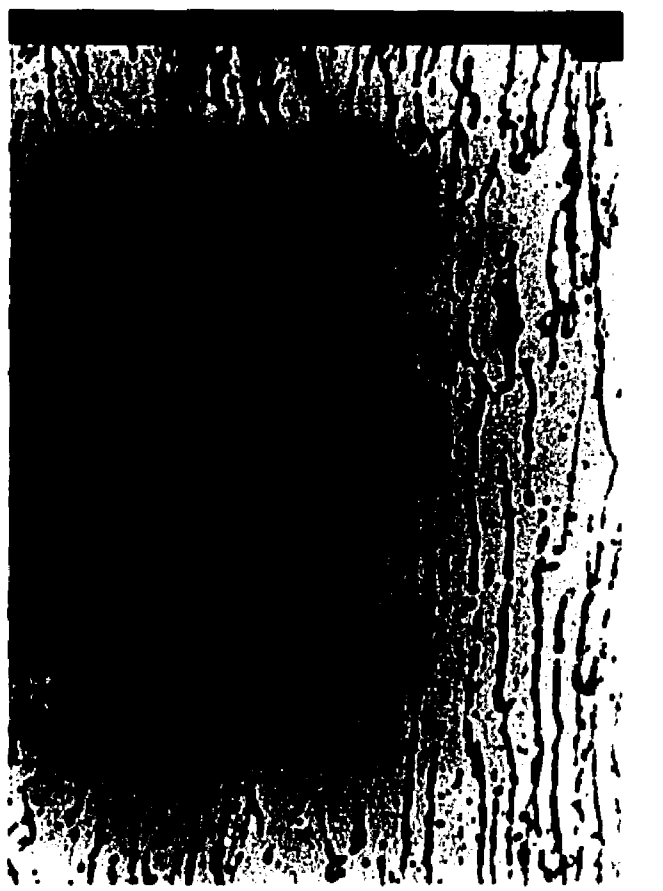

Figure 86. Glyceregia X600

Sample W9 (1200°F--0.580 per minute) Enlargement of tip of secondary crack shown in Figure 85, showing propagation of crack along interdendritic ferrite (A) and formation of pores within the ferrite (B).

Figure 87. Glyceregia X600

Sample W9 (1200°F--0.580 per minute) Same field as Figure 86, but using Nomarski differential interference contrast illumination to emphasize the localization of plastic flow (A) near the growing cracks.

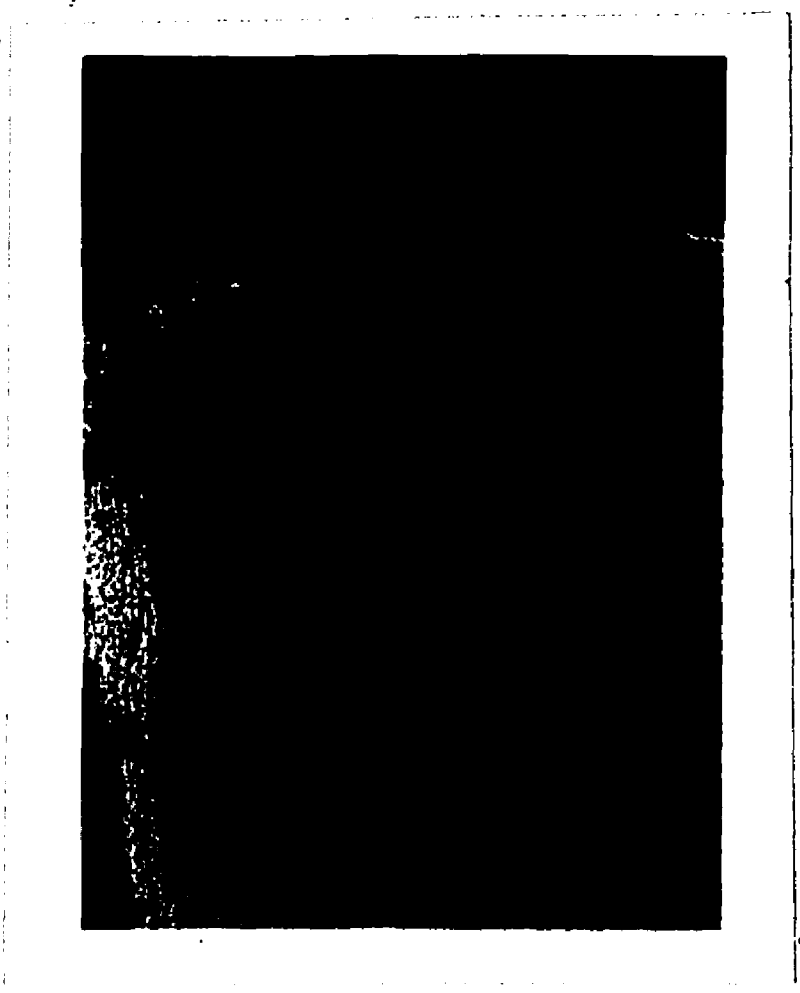

Figure 88. Oxalic Acid X125

Sample J10 (75°F--4.80 per minute) Note fracture propagating through grain-coarsened region of the heat-affected zone.

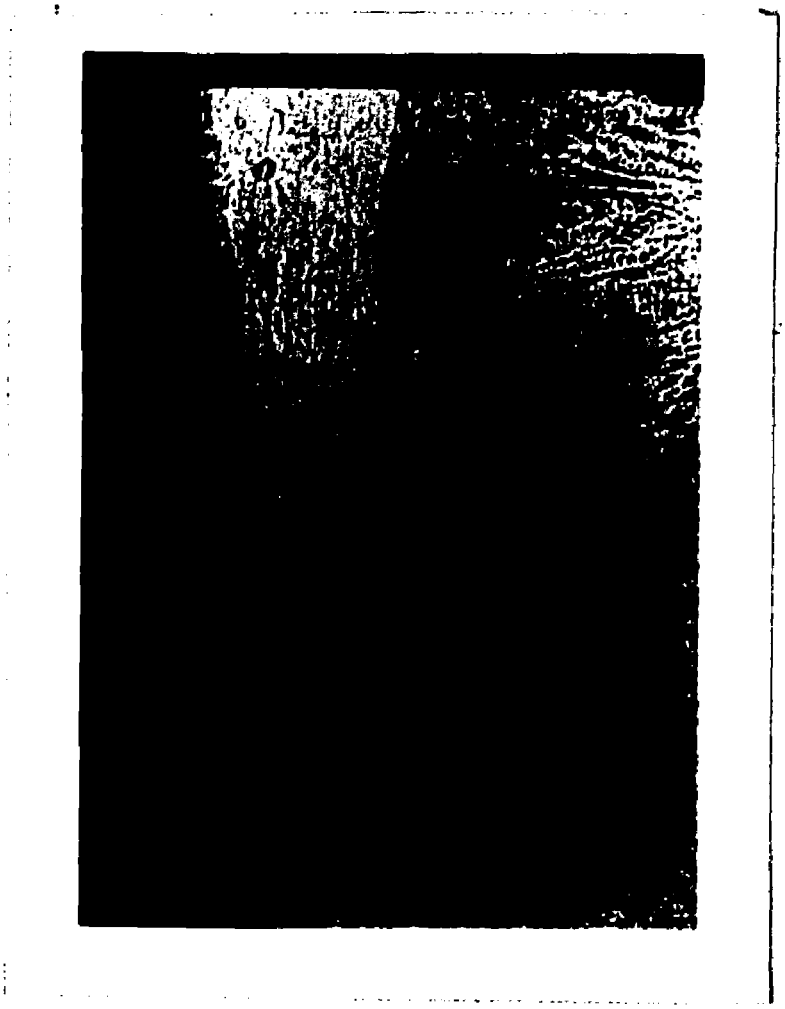

Figure 89. Oxalic Acid X125

Sample J10 (75°F--4.80 per minute) Note propagation of fracture partially through the heat-affected zone and partially through the fusion-zone, as well as the secondary crack (A) originating from a microshrinkage cavity (B) in the fusion-zone.

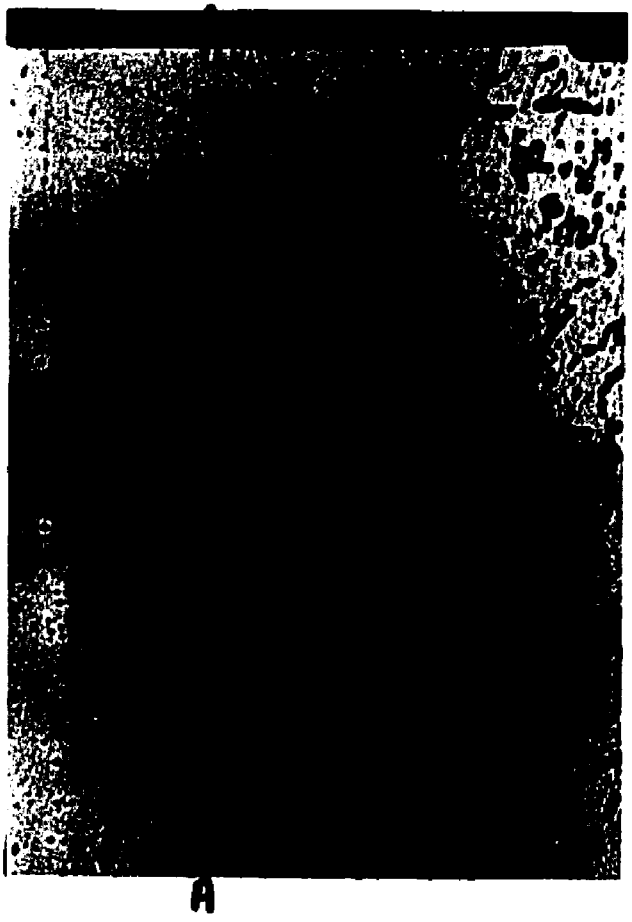

Figure 90. Oxalic acid X600

Sample J10 (75°F--4.80 per minute) Enlargement of Figure 89, showing microshrinkage defect at edge of fusion zone, fusion line (A), crack (B) emanating from microshrinkage defect, and pores forming in ferrite pools in fusion zone (C).

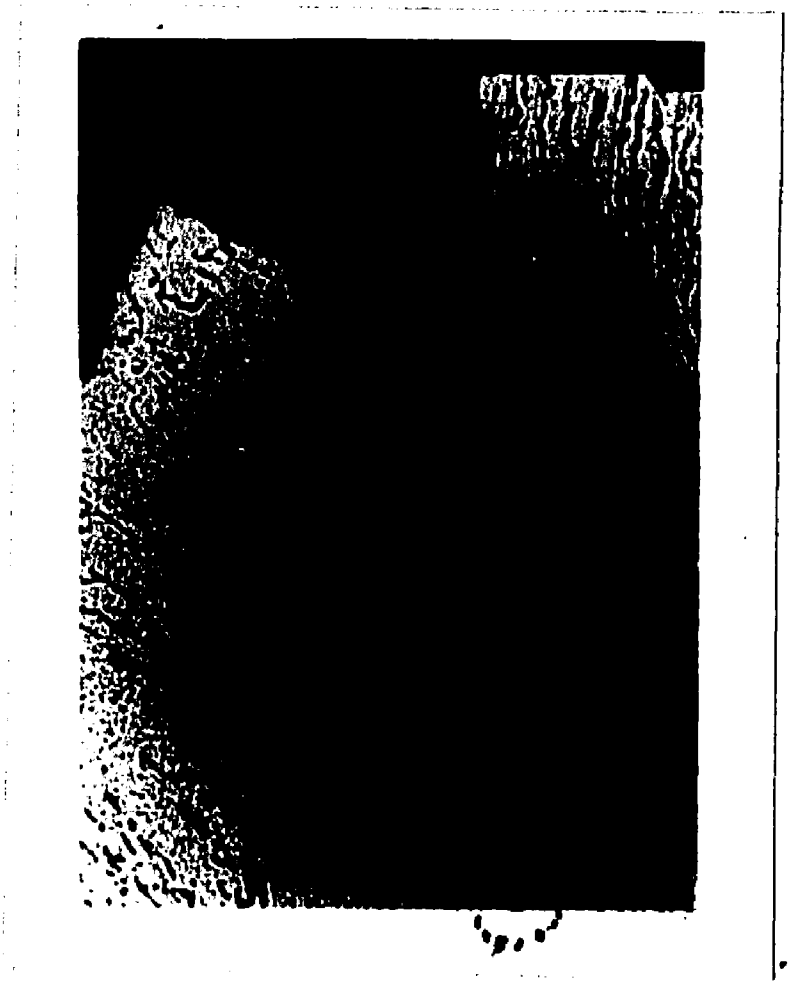

Figure 91. Oxalic Acid X600

Sample J3 (500°F--0.0690 per minute) Microstructure just behind the fracture-surface, showing propagation of two secondary cracks towards and around the periphery of inclusions (A) and localization of plastic flow (B) near one of the secondary cracks.

Figure 92. Oxalic Acid X1500

Sample J3 (500°F--0.0690 per minute) An enlargement of the circled region in Figure 91, showing a crack emanating from an inclusion: matrix interface (A), and isolated pores (B) forming within ferrite pools.

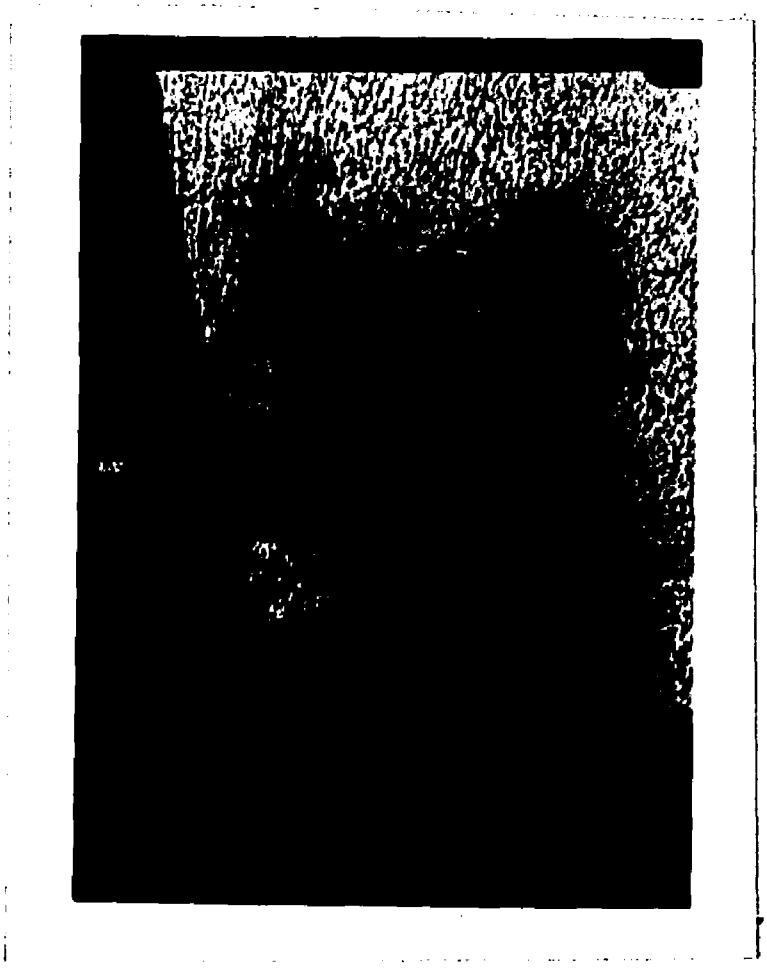

Figure 93. Oxalic Acid X125

Sample J4 (1000°F--4.87 per minute) Corner of fracture-surface showing propagation of a secondary crack (A).

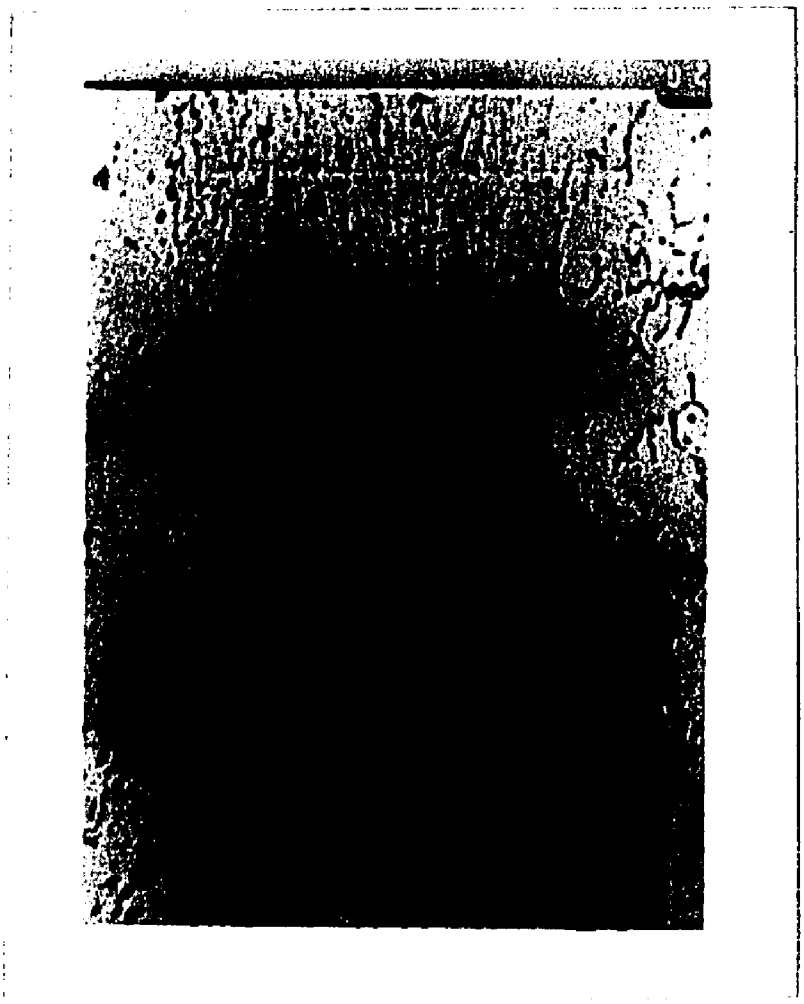

Figure 94. Oxalic Acid X600

Sample J4 (1000°F-4.87 per minute) Enlargement of growing end of secondary crack shown in Figure 93, illustrating its propagation between pools of ferrite (A).

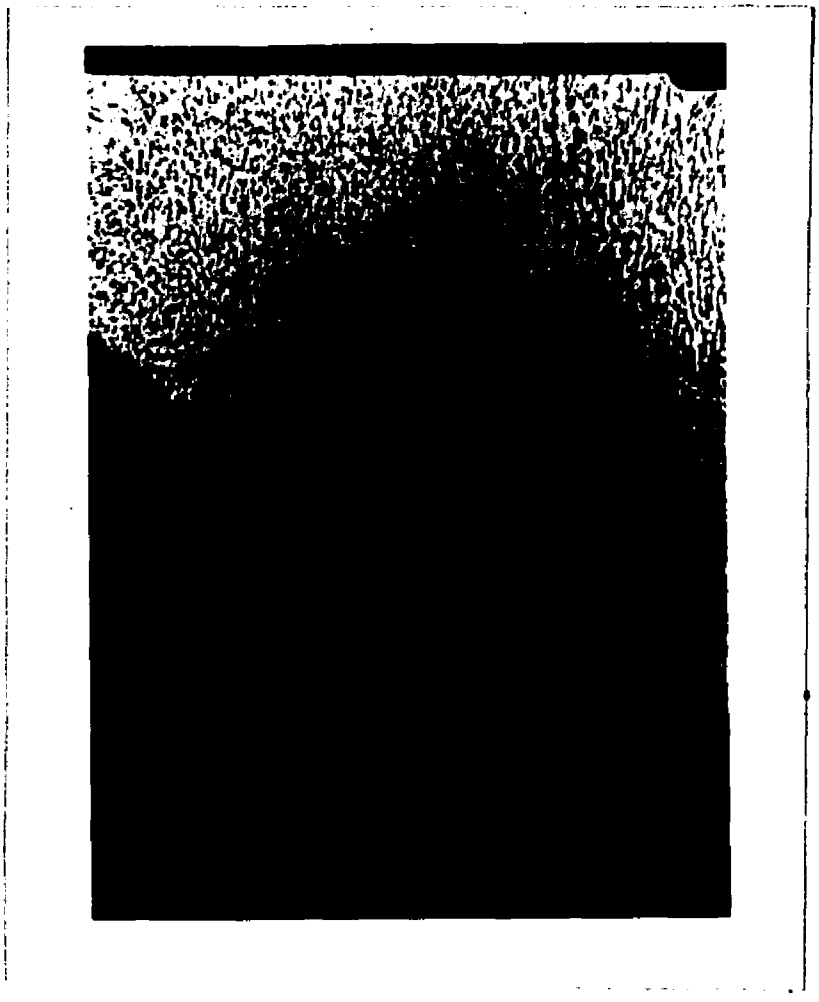

Figure 95. Oxalic Acid X125

Sample J7 (1200°F--4.86 per minute) Details of fracture surface and secondary crack (A).

Figure 96. Oxalic Acid X125

Sample J7 (1200°F--4.86 per minute) Details of fracture surface.

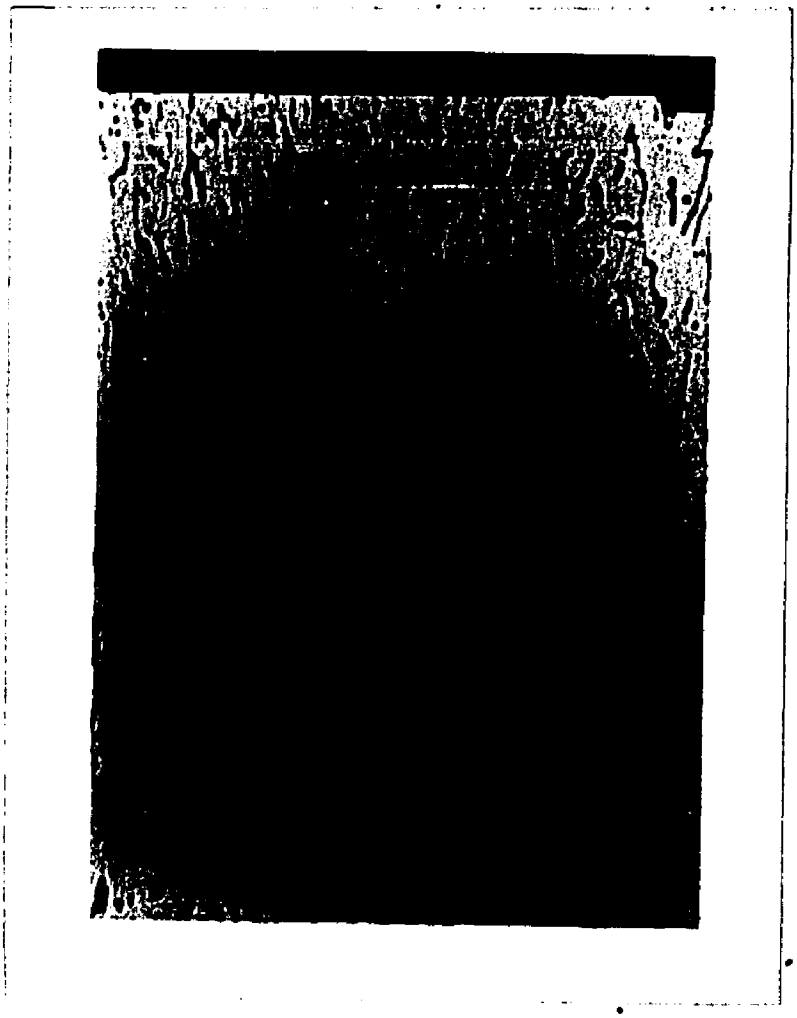

Figure 97. Oxalic Acid X600

Sample J7 (1200°F--4.86 per minute) Enlargement of tip of secondary crack shown in Figure 95. Note propagation of crack between ferrite pools and along an inclusion: austenite interface (A).

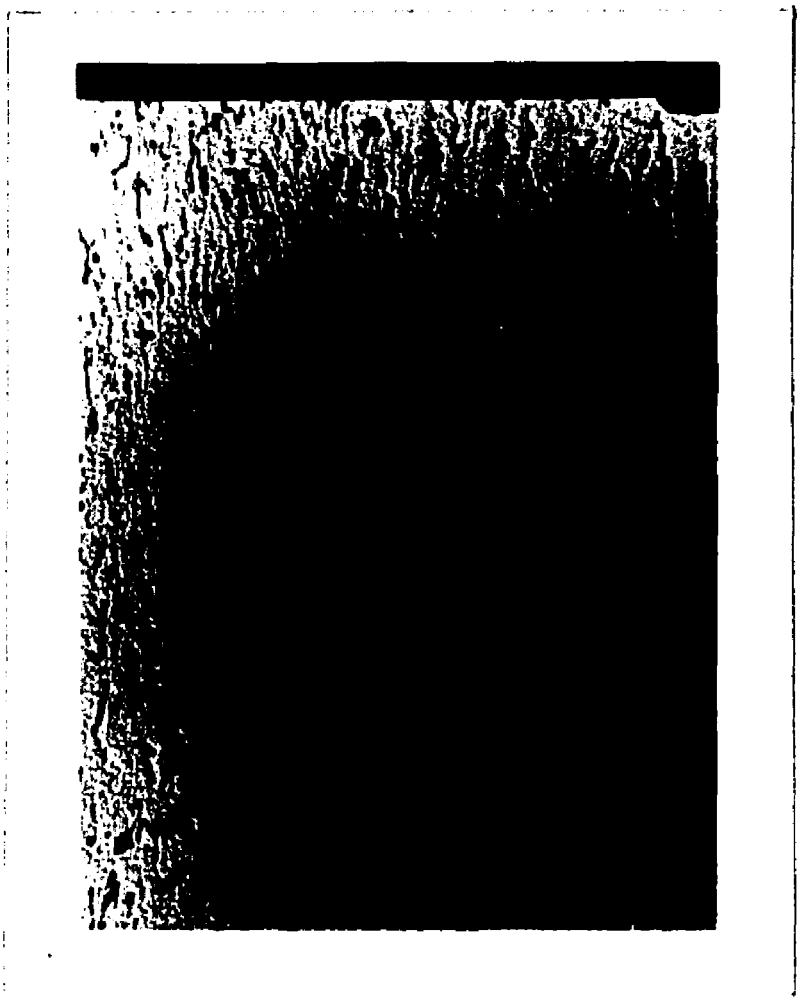

Figure 98. Oxalic Acid X600

Sample J7 (1200°F--4.86 per minute) Same field as Figure 97, but using Nomaraki differential interference contrast illumination to emphasize the localization of plastic-flow at and ahead of the crack-tip (A).

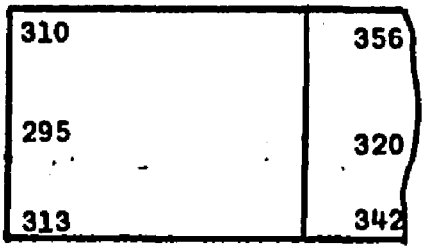

A4 (500°F: 0.62 per minute)

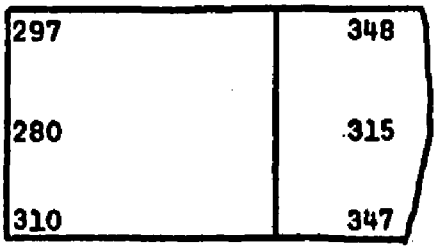

A11 (1000°F: 4.72 per minute)

Solution-annealed samples

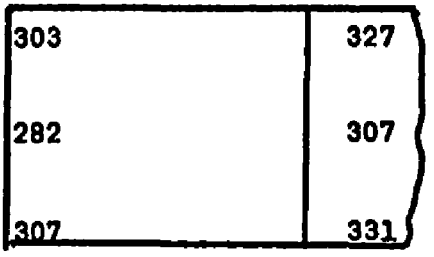

AS3 (500°F: 2.64 per minute)

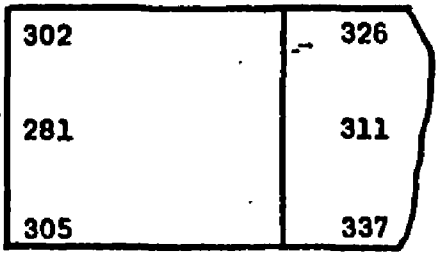

AS8 (1000°F: 4.81 per minute)

Sensitized samples

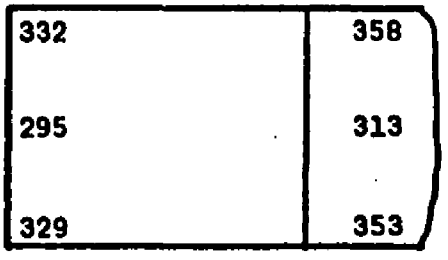

W3 (500°F: 0.0651 per minute)

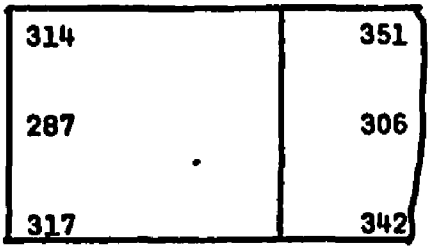

W6 (1000°F: 0.0721 per minute)

Weld metal samples

NOTE: All microhardness values are averages of 3 readings per location made with a 500 gram load using a Vickers Pyramid indenter.

Figure 99. Summary of Microhardness Results.

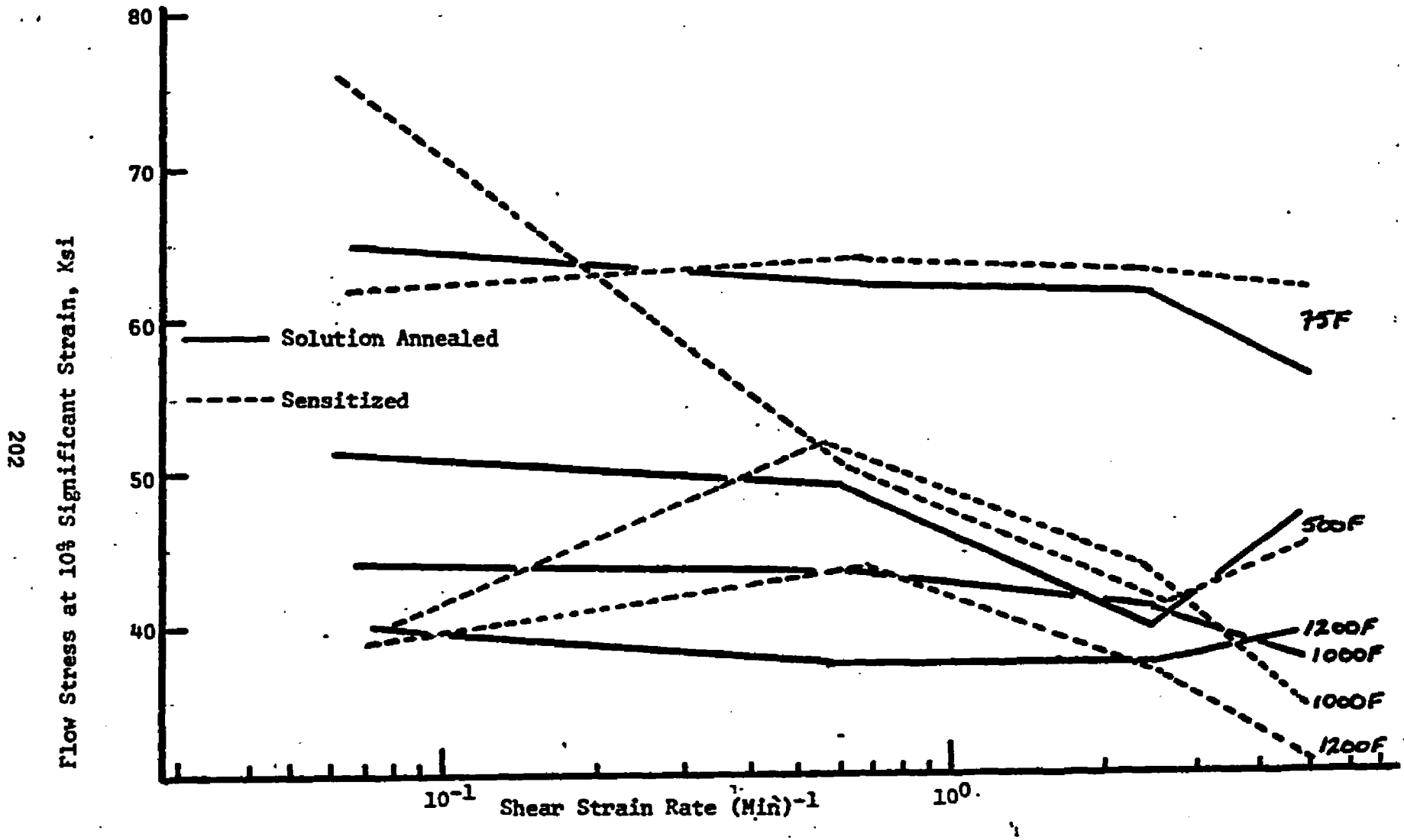

Figure 100. Flow Stress at 10% Significant Strain vs Strain-Rate at the Indicated Temperatures for Type 304 Stainless Steel Bar.

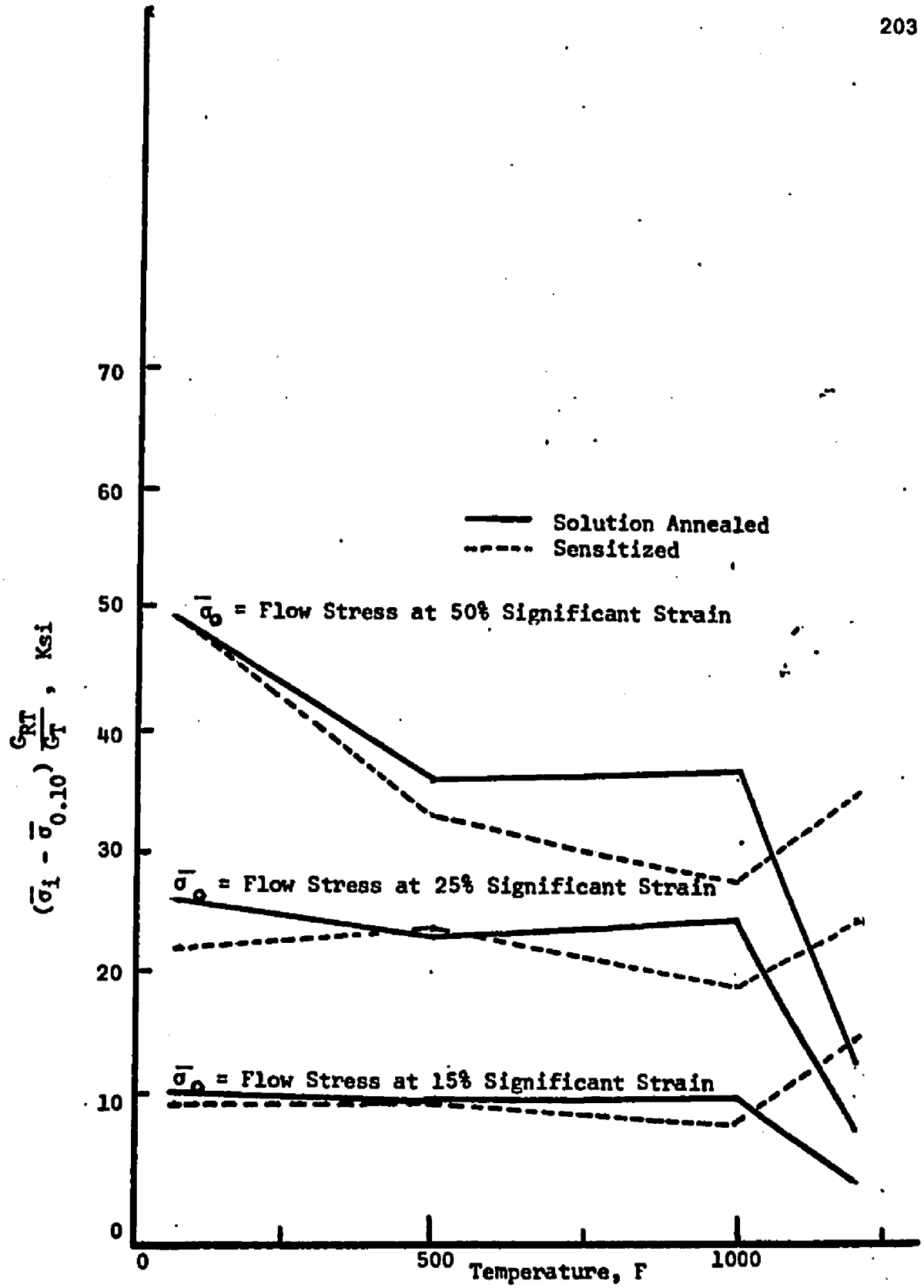

Figure 101. Barnby's Work-Hardening Parameter vs Temperature at a Nominal Strain Rate of 4.8 Inches/Inch/Minute for Type 304 Stainless Steel Bar.

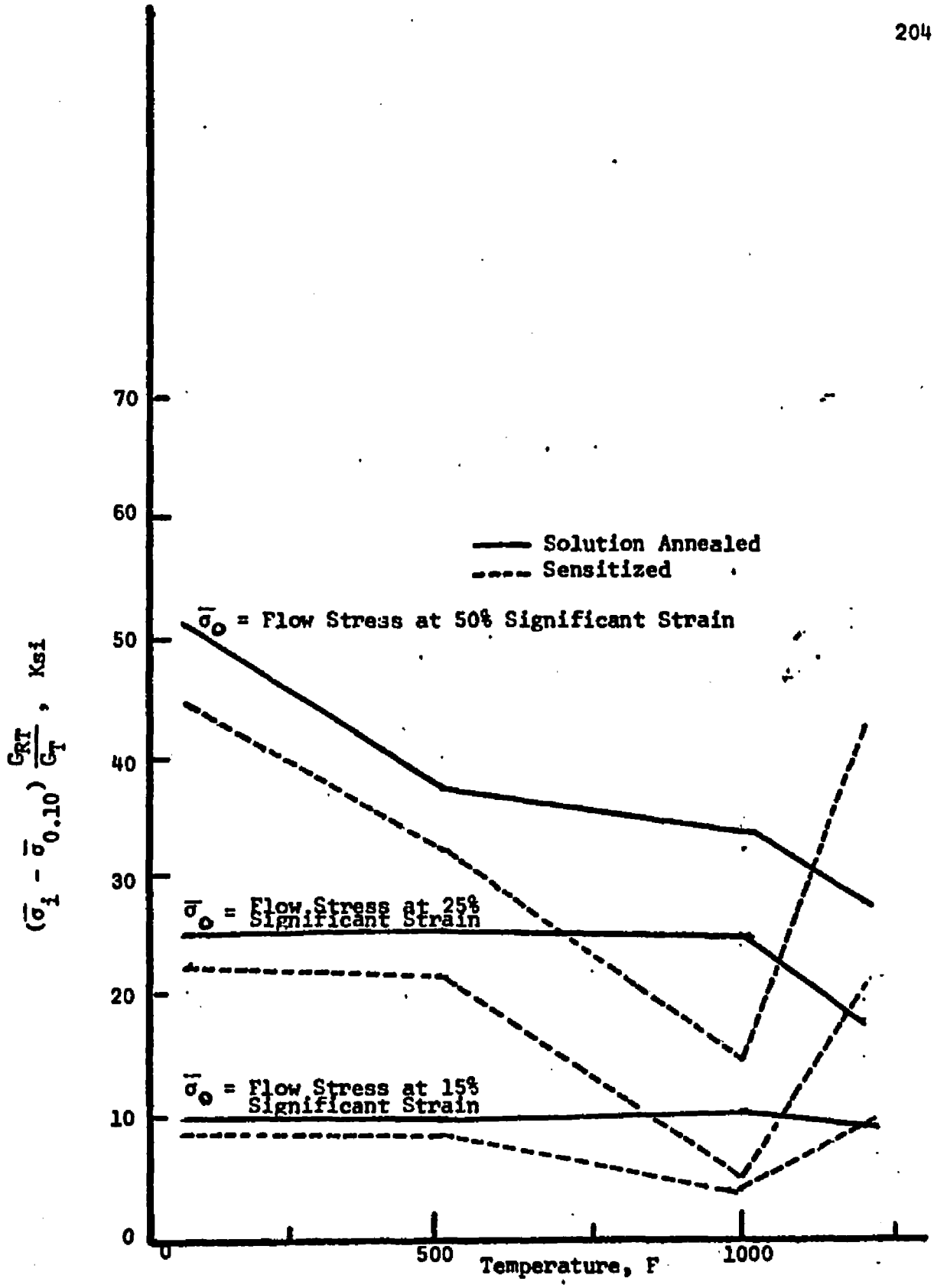

Figure 102. Bamby's Work-Hardening Parameter vs Temperature at a Nominal Strain-Rate of 2.5 Inches/Inch/Minute for Type 304 Stainless Steel Bar.

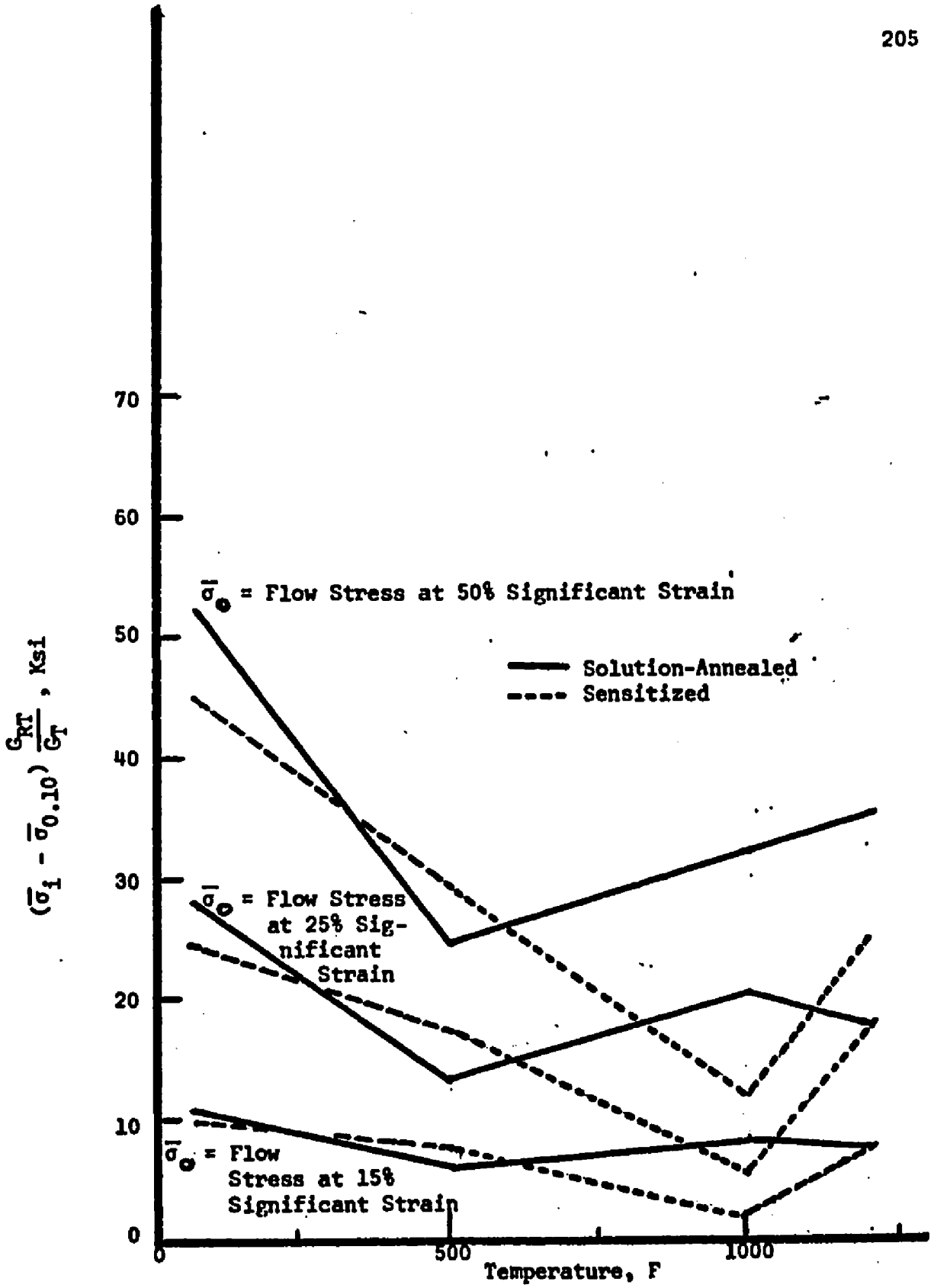

Figure 103. Barnby's Work Hardening Parameter vs Temperature at a Nominal Strain-Rate of 0.6 Inches/Inch/Minute for Type 304 Stainless Steel Bar.

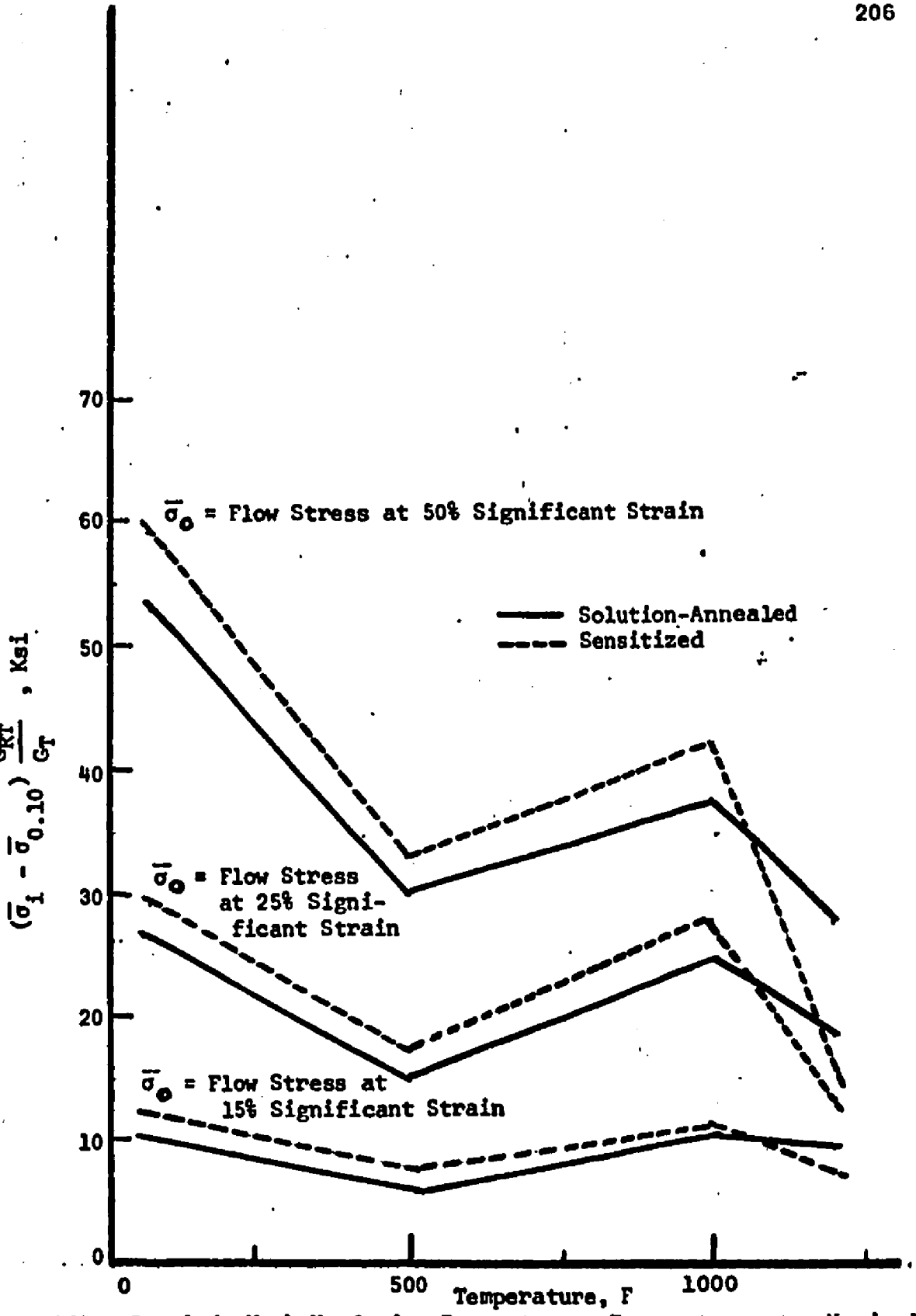

Figure 104. Barnby's Work Hardening Parameter vs Temperature at a Nominal Strain-Rate of 0.07 Inches/Inch/Minute for Type 304 Stainless Steel Bar.

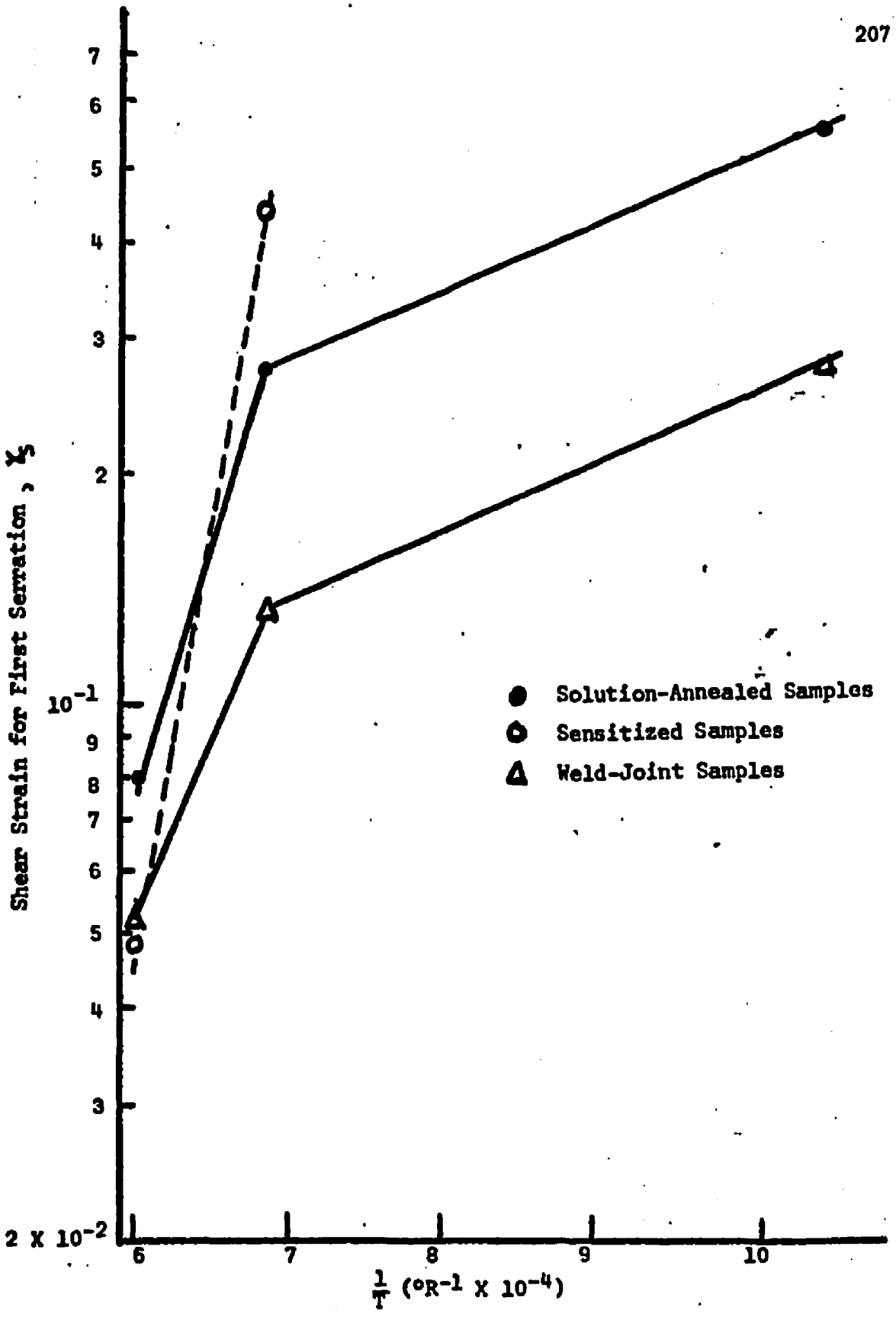

Figure 105. Shear Strain for First Serration Versus Reciprocal Temperature for Various Conditions of Type 304 Stainless Steel at a Nominal Strain-Rate of 0.07 Per Minute.